Structure and Assembly of the Fungal Prion-forming Domain HET-s(218–289)

By

William Wan

Dissertation

Submitted to the Faculty of the

Graduate School of Vanderbilt University

in partial fulfillment of the requirements

for the degree of

DOCTOR OF PHILOSOPHY

in

Chemical and Physical Biology

May, 2014

Nashville, Tennessee

Approved:

Gerald Stubbs, D.Phil.
Charles R. Sanders, Ph.D.
Martin Egli, Ph.D.
Anne K. Kenworthy, Ph.D.
Benjamin Spiller, Ph.D.

ACKNOWLEDGEMENTS

To my advisor and mentor, Gerald Stubbs, the consummate fiber diffractionist. His exuberance for knowledge, rousing lecturing style, and succinct writing are reminiscent of the pioneers of molecular biology; I have learned a great deal from observing him. He has also allowed me great freedom as a graduate student, which has been essential to my development.

I am grateful to the members of my Dissertation Committee, who have been supportive and helpful throughout my training. Our meetings have been nothing short of a scientific crucible; I can only hope I have emerged a tempered and refined scientist.

I would like to thank the senior members of the Stubbs lab, Amy Kendall, Wen Bian, and Michele McDonald. They have been great colleagues who have taught me much, helped me refine my ideas, and created a thoroughly snarky lab environment; it has been a joy to work with them. I would also like to acknowledge the many undergraduates of the Stubbs lab who I have had the pleasure of working with.

I would like to acknowledge the financial support of the National Institutes of Health, who have funded my training through the Molecular Biophysics Training Grant and a National Research Service Award.

TABLE OF CONTENTS

LIST OF FIGURES

LIST OF TABLES

LIST OF ABBREVIATIONS

A280	absorbance at 280 nm
BCA	bicinchoninic acid
BSE	bovine spongiform encephalopathy
CC	correlation coefficient
CCD	charge-coupled device
CJD	Creutxfeldt-Jakob disease
CWD	chronic wasting disease, a prion disease of cervids
EDTA	ethylenediaminetetraacetic acid
EM	electron microscopy
Gdn	guanidinium
GSS	Gerstmann-Sträussler-Scheinker syndrome, an inherited prion disease
HFIP	hexafluoroisopropanol
iCJD	iatrogenically transmitted CJD
MS/MS	tandem mass spectrometry
NTA	nitrilotriacetic acid
OD400	optical density at 400 nm
PDB	protein data bank
PMSF	phenylmethylsulfonyl fluoride
PrP	prion protein

PrP^{C}	cellular isoform of PrP
PrP^{Sc}	pathological isoform of PrP
recPrP	recominantly expressed PrP
RH	relative humidity
RMSE	root mean square error
sCJD	sporadic CJD
SDS-PAGE	sodium dodecyl sulfate polyacrylamide gel electrophoresis
ssNMR	solid state nuclear magnetic resonance
swa	swainsonine
ThT	thioflavin T
TME	Transmissible Mink Encephalopathy
Tris	tris(hydroxymethyl)aminomethane
TSE	transmissible spongiform encephalopathy
wt	wild-type

CHAPTER I

Introduction

I.1 The discovery of prions – a novel infectious agent

I.1.1 Determining the transmissibility of scrapie, the prototypical prion disease

The longest studied and prototypical prion disease is scrapie, a prion disease of sheep. While it has been suggested that scrapie was first documented by Hippocrates in 5th century BC (McAlister 2005), the oldest reliable mention is from mid-18th century Germany (Leopoldt 1750), which has since been reproduced in English (Schneider et al. 2008). In this account, Leopoldt describes basic symptoms as an initial desire to scratch against posts, followed by consumption and eventually, death. He states that the disease is contagious and invariably fatal, so to avoid damage to the flock he advises slaughtering the sheep for consumption by servants. In 1755, a petition was recorded in the *Journal of the House of Commons* concerning the evasion of an act made in the 5th and 6th years of King Edward VI, i.e. 1551–1552. This act prohibited the resale of lambs and sheep, unless the sheep were first raised for five weeks before resale, indicating a knowledge that time was required to determine whether sheep were afflicted by scrapie. Evasion of this requirement, and the establishment of a local monopoly, resulted in significant damage to the local economy.

Accounts of scrapie from the mid-18th to the early 20th century were relatively sparse, which is generally attributed to the economic incentives in keeping infections and outbreaks silent. The secrecy of the disease was so extensive that it was practically unknown to the veterinary community until the turn of the 20th century. By then, scrapie had become so prevalent in Scotland that the habit of secrecy was broken because virtually every farm had been afflicted. In 1912, the Edinburgh and East of Scotland College of Agriculture and the Board of Agriculture for Scotland commissioned an investigation, resulting in the publication of a detailed analysis of historical accounts (M'Gowan 1914). In his investigation, M'Gowan found that scrapie occurred in many areas of Britain, France, and Germany,

with the name of the disease varying by region. The over-forty different names (Schneider et al. 2008) included"scratchie", "rubbers", and "shakings", which were derived from two primary symptoms of the disease: the initial violent scratching against objects which often resulted in torn fur and flesh, and the later trembling and ataxia. During his investigation, another account was published and was generally consistent with M'Gowan's findings (Stockman 1913). Historical reports had opposing conclusions about the hereditary or contagious nature of scrapie, as well as a myriad of conflicting etymological observations, but they generally agreed that scrapie was only seen in sheep older than 18 months, incurable, and eradication of the disease required culling entire flocks. M'Gowan concluded from his investigation that scrapie was an infectious disease caused by sarcosporidia, a protozoan infection common to virtually all sheep, and that it was transmitted *in utero*, but was otherwise not communicable. A later study by M'Fadyean (1918) tore down the sarcosporidia hypothesis on the basis of over-reliance on the undocumented accounts of farmers, inconsistencies in reasoning, and the lack of controlled experiments. In his experiments, M'Fadyean showed that diseased sheep could give birth to non-diseased animals, but were unable to transmit the disease through blood transfusions and subcutaneous inoculations of blood, small intestinal contents, cerebral spinal fluid, and suspensionions of skin scrapings and foetal cotyledons. The inability to transmit scrapie by inoculation led to other theories of transmission including sexual transmission between individuals with subsequent passage to offspring (Gaiger 1924).

While the aforementioned accounts by British veterinaries list examples of case studies from Germany and France, they appear to have missed a pair of studies concerning the physiological effects and the nature of the infectious agent. In the first study (Besnoit and Morel 1898), sheep were sacrificed at the onset of scrapie symptoms, and post-mortem examinations were conducted. As with the British studies, macroscopic examination revealed no unusual features, but this study also conducted microscopic examinations. Microscopic examinations revealed lesions and vacuolation throughout the nervous system and intense lesions and degradation in motor neurons. In hopes of finding the infectious agent they attempted to culture bacteria from degraded neurons, but these experiments gave negative

results. In the second study (Besnoit 1899), they tried to transmit scrapie by inoculating rabbits, guinea pigs, and sheep with blood, cerebral spinal fluid, and liquid derived from arachnoid matter and mesenteric lymphnodes, all of which proved unsuccessful. While not much experimental detail is given, it is noted that a sheep that was given a blood transfusion from an infected sheep was monitored for a total of 14 months.

A later study by Cuillé and Chelle (1936) made use of Besnoit and Morel's observations of degenerated nerve tissue and the 18 month incubation period observed by the British researchers, resulting in the successful transmission of scrapie. In this study Cuillé and Chelle confirmed that 9 of the test sheep were uninfected by first raising them for 18 months. Following this waiting period, the sheep were subjected to intra-ocular, epidural, and intra-cerebral inoculation of cerebral spinal fluid or lumbar marrow homogenates. While 7 sheep died of non-scrapie related causes 6–9 months post inoculation, the remaining two sheep, which were both subjected to intra-ocular injection of marrow homogenate, developed scrapie in 15 or 22 months. In a follow up to this study, another two out of 5 sheep, which didn't succumb to other illnesses, were successfully infected using spinal cord homogenates injected epidurally or subcutaneously (Cuillé and Chelle 1938a). In a subsequent study, they were able to infect two sheep using intra-occular and subcutaneous injection of filtered spinal cord homogenate (Cuillé and Chelle 1938b). Their filtration protocol consisted of coarse filtration through gauze followed by filtration through a Chamberland L3 filter, similar to an experiment used to demonstrate that tobacco mosaic virus was caused by a non-microbial pathogen (Beijerinck 1898, and translated Beijerinck 1942), leading to the assumption that the scrapie agent was a virus. Cuillé and Chelle also published another paper (1939), demonstrating transmission of scrapie to goats, an animal that does not normally contract scrapie. They found that the incubation time required 25 months, and that the goats developed motor dysfunction similar to that in sheep, but did not exhibit any scratching behavior.

Around the same time as Cuillé and Chelle's experiments, an inadvertent large-scale replication was conducted in Britain (Gordon 1946). Following 4 years of testing, in 1935 a vaccine for louping-ill virus, a sheep virus with about 9% mortality, was issued for general

use. The vaccine was produced by formalin treating brain, spleen, and spinal suspensions from an infected animal, and was delivered by intra-cerebral inoculation. The vaccines used that year were produced as three batches, and proved to be very effective against louping-ill. By 1937, cases of scrapie arising in otherwise non-infected flocks began to appear, all of which were traceable to batch 2 of the vaccine. While this incident reproduces many of the observations of Cuillé and Chelle's experiments, a notable new factor was that formalin treatment did not inactivate the scrapie agent. A later study from Iceland confirmed that the scrapie agent passed filters, but also showed that concentrating the agent by ultracentrifugation decreased the time required for manifestation of symptoms down to three months (Sigurdsson 1954). In this study, Sigurdsson also compares scrapie to visna, a viral disease of sheep, that has a similar period of latency before occurrence of symptoms, leading to the term "slow virus".

I.1.2 Transmissible Encephalopathies in Humans

Contemporaneously with the emerging idea of scrapie as a slow virus, Gajdusek and Zigas (1957) published their observations on kuru, a disease affecting the Fore people of the Eastern Highlands of Papua New Guinea. Kuru is a Fore word meaning trembling associated with fear or cold, which describes the ataxia and tremors associated with the onset of disease symptoms. After initial symptoms appear, degeneration occurs rapidly leading to severe incoordination resulting in inability to walk, stand, or sit, along with loss of speech, though intelligence appears normal. Within 6 months to a year the patient succumbs to starvation caused by inability to swallow, decubitus ulcerations, or hypostatic pneumonia. They also noted that kuru was prevalently found in adult women and children of both sexes, but rarely in adult men, which suggested to them a strong genetic association.

In a later report, Gajdusek and Zigas (1959) published descriptions of their pathological findings, which included widespread neurodegeneration and senile plaque-like bodies which showed anisotropy under polarized light after cresyl-violet staining. They also note that they found no infectious agent by passage of brain material through chick embryos and mice. A report the same year (Klatzo et al. 1959) showed the detailed pathological findings

and noted that the pathology of kuru closely resembled that of Creutzfeldt-Jakob disease (CJD), a rare neurodegenerative disease of humans (Siedler and Malamud 1963).

After the publication of clinical and pathological findings on kuru, Hadlow (1959) suggested an overall resemblance to scrapie and noted the possibility for transmissibility. Hadlow also noted that scrapie had only been transmitted to sheep and the closely related goat, as well as the long incubation times needed. Following his suggestions, Gajdusek and coworkers began a series experiments in 1962, attempting to transmit kuru and CJD to chimpanzees and other monkeys. Initial observations showed negative results (Gajdusek and Gibbs 1964), though continued observation showed clinical onset starting at about 20 months (Gajdusek et al. 1966). A subsequent experiment demonstrated that serial passage of kuru into a second generation of chimpanzees shortened incubation times to about one year (Gajdusek et al. 1967). Passage of kuru-afflicted chimpanzee brain was also inoculated into spider monkeys (Gajdusek et al. 1968), which resulted in kuru symptoms about two years later. CJD from human brain was successfully transmitted to chimpanzees with a 13 month lag time (Gibbs et al. 1968), followed by transmission of CJD and kuru to several different species of "New World" monkeys (Gajdusek and Gibbs 1971). The latter study also included a number of serial propagation experiments, demonstrating decreasing incubation time upon serial passages. Taken together, these findings implicated an infectious agent associated with kuru and CJD that was related to scrapie, thus establishing a slow virus hypothesis of infection.

The establishment of kuru as an infectious disease eventually led to determining the epidemiology of the disease. Prior to demonstrating the transmissibility of kuru, Gajdusek (1963) included what he called "an outlandish hypothesis" involving auto-immune hypersensitivity caused by the Fore practice of mourning via ritual cannibalism. While Gajdusek acknowledged this mechanism was unlikely, Glasse, an anthropologist, was able to explain the preponderance of kuru cases in adult women and children of both sexes as a result of the rules of ritualistic cannibalism (1967). Briefly, these rules stipulated that the body of the deceased was to be given to a woman on the maternal side, to be consumed by women and the children in their care. Men did not partake in cannibalism, owing to the thought

that doing so would diminish their vitality. Further study (Mathews et al. 1968) explained the spread of kuru across certain Fore tribes that intermarried, eliminating the need for a genetic hypothesis. This hypothesis was borne out by the eventual decline of kuru deaths owing to the cessation of cannibalism due to the influence of Western civilization (Alpers 1970; Gajdusek 1977).

I.1.3 Unusual Properties of the Scrapie Agent

Parallel to the experiments demonstrating interspecies transmission of kuru and CJD to primates, a series of experiments were performed demonstrating interspecies transmission of scrapie and transmissible mink encephalopathy (TME) (Hartsough and Burger 1965; Burger and Hartsough 1965). These experiments included TME to goats (Zlotnik and Barlow 1967), mice (Barlow and Rennie 1970), and squirrel monkeys (Eckroade et al. 1970), as well as scrapie to mice (Chandler 1961). Transmission of TME to mice and goats produced similar pathologies to scrapie, strengthening the idea that these diseases involved a common infectious agent. The ability to obtain scrapie-like spongiform encephalopathies in smaller model animals allowed for the quantitative assessment of infectious titers of brain homogenates by titration (Chandler 1963). Quantitative titer analysis allowed for experiments to determine the nature of the scrapie agent by measuring resistance to inactivation and by purification of the scrapie agent through measuring the infectious titer of separated fractions.

Attempts to inactivate the scrapie agent with irradiation yielded a number of results that indicated a lack of nucleic acid. Experiments with ionizing radiation (Alper et al. 1966; Field et al. 1969; Alper et al. 1978) showed high resistance to inactivation, which was indicative of a relatively small molecule. Comparisons with inactivation studies of a range of molecules indicated that the size of the scrapie agent was much smaller than a virus. Similar inactivation results were obtained for ionizing radiation studies of kuru and CJD (Gibbs et al. 1978), indicating a relatively small infectious agent. Scrapie inactivation by ionizing radiation was also found to be more effective under oxygenated conditions (Alper et al. 1978), while inactivation of bacteriophage or transforming DNA did not show

similar oxygen sensitivity. Inactivation experiments using UV irradiation (Alper et al. 1967; Latarjet et al. 1970; Alper et al. 1978) showed that the scrapie agent was not sensitive to wavelengths that deactivated nucleic acid, but instead had a distinct inactivation spectrum.

Chemical methods of scrapie inactivation and extraction yielded a number of unusual results. The scrapie agent was found to be stable across a broad temperature range including prolonged storage at $-25\,^{\circ}\mathrm{C}$, and incomplete inactivation after incubation at $118\,^{\circ}\mathrm{C}$ (Hunter and Millson 1964). Though no precise quantitative experiments were performed, qualitative experiments indicated that formalin had some impact on scrapie infectivity (Pattison 1965), though only with prolonged incubation in excess of two years. Scrapie showed slight inactivation upon incubation at pH values between 2.1–4.8 or 8.4–11, or incubation in CsCl (Mould et al. 1965). Extraction with ether, acetone, butanol, or chloroform-methanol mixtures also resulted in partial inactivation (Mould et al. 1965). Enzymatic digestion with neuraminidase and a number of lipases showed no inactivation, while trypsin showed slight inactivation but trypsin with sodium deoxycholate showed complete inactivation (Hunter and Millson 1967). It was later shown that lipid extraction with fluorocarbons made the scrapie agent more susceptible to inactivation by trypsin or papain, though complete inactivation was not obtained (Hunter et al. 1969). Extractions of scrapie agent with strong phenol solutions or 8M urea, or periodate treatment, result in nearly complete inactivation (Hunter et al. 1969).

Early efforts to purify the scrapie agent were unable to isolate a viral agent. Studies using differential centrifugation and sucrose gradients found that the fractions with the highest scrapie titer contain mitochondria (Hunter et al. 1964), while CsCl gradients showed co-localization with lysosomes (Mould et al. 1964b). In both cases, infectivity was found throughout the gradients. Electron microscopy (EM) of mitochondrial fragments did not show the presence of virions (Hunter et al. 1964). Chromatographic and ultrasonication results indicated that the scrapie agent was closely bound to tissue components (Mould et al. 1964a; Hunter and Millson 1964). Attempts to separate the scrapie agent from tissue debris provided some of the chemical inactivation results described above (Mould et al. 1965; Hunter and Millson 1967), but were unable to isolate high titer scrapie fractions.

The unusual inactivation and purification properties of scrapie and other spongiform encephalopathy-related agents led to a number of hypotheses concerning its nature. As a result of her inactivation studies with ionizing and UV irradiation, Alper suggested that the scrapie agent contained no nucleic acid (Alper et al. 1967), though others who reproduced her results were unconvinced (Field et al. 1969). One hypothesis posited the possibility of a self-replicating polysaccharide (Field 1966), while another suggested that a polysaccharide coat could lend sufficient protection against irradiation to a virus (Adams and Caspary 1967). Taking into account the unusual properties of the scrapie agent and contemporary theories on biological membranes (Changeux et al. 1967), a modified membrane hypothesis was suggested (Gibbons and Hunter 1967; Hunter et al. 1968; Hunter 1972), whereby a pathogenically structured membrane would spread by incorporation into healthy membranes. A self-propagating protein in the form of a histone was suggested (Pattison and Jones 1967), and several possible mechanisms of protein self-propagation were discussed (Griffith 1967). Following the discovery of the viroid (Diener 1971), a short RNA-only infectious agent, it was suggested that a viroid might be consistent with inactivation studies (Diener 1972). Others noted the unusual properties of the scrapie agent, and resorted to using the term "unconventional virus" (Gajdusek 1977).

I.1.4 The Nature of the Scrapie Agent

In order to directly determine the molecular properties of the scrapie agent, Prusiner and colleagues began work on purification protocols. Initial results showed that the scrapie agent had sedimentation profiles similar to polyribosomes, but different from other subcellular markers, indicating the possibility of purification (Prusiner et al. 1977). Purification protocols using linear sucrose gradients found that while scrapie infectivity was spread across entire gradient, bulk protein and nucleic acid was not, indicating that the scrapie agent could be purified from bulk contaminants, and that it likely consisted of multiple isoforms (Prusiner et al. 1978a; Prusiner et al. 1978b). Incubation at high temperatures also affected sedimentation profiles, indicating that the scrapie agent was likely to be hydrophobic (Prusiner et al. 1978a). Refinement of purification protocols provided further separation

of bulk protein and scrapie agent, and inactivation of these partially purified specimens using protein denaturants strengthened arguments for a protein-related agent (Prusiner et al. 1980). Further refinement of purification protocols involved exploiting the insensitivity of the scrapie agent to nucleases and proteases, resulting in purification of 100–1000 fold with respect to total protein (Prusiner et al. 1981b; Prusiner et al. 1981a). Purified scrapie agent was inactivated by chaotropic salts and hydroxyl ions (Prusiner et al. 1981b), reversibly inactivated by chemical modification (McKinley et al. 1981), and susceptible to protease, but not nuclease, digestion over extended time periods (Prusiner et al. 1981a). These properties were not readily apparent in brain homogenates, likely caused by the protective effects of bulk protein.

The molecular properties of partially purified scrapie agent indicated that a protein component was required for infectivity. This set of molecular properties distinguished the scrapie agent from other known infectious agents, leading Prusiner (1982) to coin the term "prion", a quasi-portmanteau of proteinaceous and infectious. While the initial prion hypothesis posited a requisite protein component, it did not explicitly exclude a nucleic acid component. Comparisons of scrapie inoculated and uninoculated control hamster brain homogenates subjected to the same purification procedures revealed a protein found only in scrapie infected animals (Bolton et al. 1982). This novel band had a broad electrophoretic mobility in sodium dodecyl sulfate polyacrylamide gel electrophoresis (SDS-PAGE), with an apparent molecular weight between 27–30 kDa. Autoradiography of labelled scrapie prions indicated that the concentration of this protein correlated with infectious titer. EM of highly purified prion fractions showed rod-like structures but no obvious virus-like particles (Prusiner et al. 1982). Direct correlation between proteinase K digestion of the 27–30 kDa protein and subsequent infectious titer demonstrated that this protein was a necessary component of the scrapie prion (McKinley et al. 1983), earning it the moniker "prion protein" (PrP), with PrP 27–30 denoting the proteinase K resistant fragment.

Further purification of PrP allowed for the determination of the precise nature of the scrapie prion. Purification of PrP 27–30 to near homogeneity indicated that the rod-like structures seen by EM were mainly composed of PrP 27–30 (Prusiner et al. 1983). Solutions

of PrP 27–30 rods were dyed with Congo red which induced birefringence under polarized light, a property long attributed to amyloid fibrils (Divry and Florkin 1927), though definitive confirmation from X-ray fiber diffraction would not come until later (Wille et al. 2009). Inactivation of scrapie prions through denaturation was correlated with protease sensitivity, and loss of rods and Congo red binding, indicating that the rods were the infectious agent. Extensive PrP 27–30 purification also allowed for the production of antibodies (Bendheim et al. 1984), which allowed for correlation of Congophilic deposits and immunostained plaques in serial brain sections. UV absorption spectra of purified PrP 27–30 indicated that no nucleic acid was present, and amino acid sequencing indicated that scrapie prions contained a single protein (Prusiner et al. 1984). Amino acid sequencing allowed for the determination that PrP is encoded for by a cellular gene, and a protease sensitive protein is found by western blotting with anti-PrP 27–30 antibodies (Oesch et al. 1985). Sequencing of the chromosomal gene showed that the coding sequence of PrP is uninterrupted by introns, indicating that the difference between the normal cellular form, PrP^{C}, and the scrapie isoform, PrP^{Sc}, is caused by post-translational modification (Basler et al. 1986).

The conversion from PrP^{C} to PrP^{Sc} appears to be caused by the reconfiguration of its molecular structure. Studies on PrP^{Sc} using mass spectrometry (MS) did not reveal any alternative splicing or post-translational chemical modifications (Stahl et al. 1993). Spectroscopic analysis indicated a loss of α-helical structure and gain of β-sheet structure associated with the formation of PrP^{Sc} from PrP^{C} (Pan et al. 1993). Structure determination of a recombinant construct of PrP^{C} consisting of the residues found in PrP 27–30 showed a predominantly α-helical protein (James et al. 1997), while electron crystallography and molecular modelling of PrP 27–30 two-dimensional crystals indicated a four-rung β-solenoid structure (Wille et al. 2002; Govaerts et al. 2004). While high resolution structure determination of PrP^{Sc} has not yet been attained, amassed evidence suggests that the formation of pathogenic PrP is caused by overall conformational change leading to a β-sheet rich structure.

I.1.5 Prions and Spongiform Encephalopathies

While the majority of knowledge on prions has come from scrapie adapted to mouse and hamster, the prion hypothesis and role of PrP has proved to be useful in explaining spongiform encephalopathies. Immunoblotting and EM of purified PrP 27–30 from sporadic human CJD (sCJD) (Bockman et al. 1985), and iatrogenically tranismitted CJD (iCJD) (Gibbs et al. 1985) demonstrated similarities to hamster-adapted scrapie. Subsequent immunohistological studies showed positive staining for PrP 27–30 in kuru and Gerstmann-Sträussler-Scheinker syndrome (GSS), a familial prion disease (Roberts et al. 1986). The prion also proved to be useful in explaining newly discovered spongiform encephalopathies including chronic wasting disease (CWD) in cervids (Bahmanyar et al. 1985; Guiroy et al. 1991), and bovine spongiform encephalopathy (BSE) (Wells et al. 1987; Prusiner et al. 1993). The successful detection of PrP 27–30 in these diseases using antibodies produced against hamster-adapted scrapie PrP 27–30 not only confirmed the presence of prion, but also indicated that the PrP amyloids are similarly structured. This family of PrP-related diseases is now known as the transmissible spongiform encephalopathies (TSEs).

I.1.6 The Diversity of Prion Phenotypes is Caused by Strains

Depending on the fibrillization environment, prions can induce a diverse array of phenotypes, despite being formed form the same protein. Environment can be defined as the particular fibrillization conditions, such as solution conditions *in vitro* or the brain of a particular species *in vivo*. Modest examples of strain adaptation are generally seen when crossing the species barrier, usually resulting in decreasing incubation time on serial passage (Gajdusek et al. 1967). However, one particularly interesting example of strain adaptation caused by species crossing is the emergence of the drowsy (DY) and hyper (HY) strains caused by passage of TME into Syrian hamsters (Bessen and Marsh 1992). After passaging through two generations of hamsters, it was observed that on the third passage, there was a divergence of phenotypes and incubation times, with faster incubation times giving a hyper phenotype while slower incubation times had a drowsy phenotype. Eventually separate serial passage of each phenotype resulted in stabilization of these two strains, and on passage

back to mink, it was found that HY was no longer able to cause TME. Since prion activity is dictated by its three-dimensional strucutre, the basis of the strain phenomenon appears to be structural mutation caused by environmental conditions.

Besides adaption caused by prion transmission between species, a diverse range of prion strains has been produced through attempts to produce recombinant PrP prions. Recombinant PrP is difficult to refold into fully infectious prions and generally requires serial passage through brains in order to improve titre (Legname et al. 2004), though some labs have been able to produce prions *de novo* (Castilla et al. 2005; Wang et al. 2010). Prion strains can be separated with serial passage of brains from animals that show distinct incubation times, resulting in the production of stable strains with different levels of infectivity (Colby et al. 2009). This type of strain formation appears to be caused by the formation of heterogeneous amyloid mixtures from recombinant protein.

Besides changing the particular fibrillization conditions of prions, differences in sequence can cause distinct phenotypes. In humans, these manifest as familial prion diseases such as GSS (Hsiao et al. 1989) or fatal familial insomnia (FFI) (Medori et al. 1992). These diseases have distinct pathologies and phenotypes, and tend to take effect earlier than sporadic prion diseases. In sheep, it was found that certain polymorphisms within the PrP gene modulated susceptibility to scrapie (Fast and Groschup 2013). On breeding of less susceptible sheep, a new strain of scrapie was found, with distinct pathological differences from "classical" scrapie. These mutations seem to have caused a sporadic strain so distinct from classical scrapie that "atypical" scrapie may not be transimissible between sheep under normal circumstances.

I.1.7 Functional prions can explain non-Mendelian heritable traits

While the term prion became synonymous with "spongiform encephalopathy causing agent", the idea of a self-propagating protein structure proved to be more broadly applicable. The idea of prions as a mode of non-Mendelian inheritance was first applied to [URE3], a phenotype in *Saccharomyces cerevisiae* involving the prion form of the protein Ure2p

(Wickner 1994). It has since been shown that prions represent a common mode of non-Mendelian inheritance in *S. cerevisiae* (Halfmann et al. 2012). *S. cerevisiae* prions have also been shown to form strains with varying levels of phenotypic expression (King and Diaz-Avalos 2004). This strain phenomenon has been shown to be caused by structural differences (Toyama et al. 2007). A prion mechanism was also found for mating-type determination in the fungus *Posopora anserina* (Coustou et al. 1997; Saupe 2011). With these functional prions, it was found that prions could act as molecular triggers in order to elicit a phenotype across a population.

I.2 A brief history of amyloids

I.2.1 Some key observations from early amyloid research

While what we now know as amyloid had been observed in autopsies as early as the 17^{th} century (for review see Cohen 1986), the term amyloid was first coined by Virchow in 1854. The word amyloid was derived from the Greek and Latin words for starch; this name was given because the tinctorial properties of amyloid were similar to that of starch when stained with iodine. Shortly after, it was demonstrated that amyloid plaques did not contain carbohydrates but contained protein (Friedreich and Kekulé 1859). Following the classification of amyloid, it was discovered that amyloidosis could occur with infection or chronic inflamation, by injection with certain substances, and in the absence of prior symptoms, was more likely to be found in organs of older individuals (Cohen 1986). These plaques remained the mainstays of amyloid research for many decades (Cohen 1967a, b, c; Glenner 1980a, b). Among the important discoveries of this period was the discovery that unstained amyloid was weakly birefringent when viewed with crossed polarizers and strongly birefringent after staining with Congo red (Divry and Florkin 1927). Birefringence demonstrated that amyloids were not amorphous masses, but instead consisted of structures ordered at a level that could not be resolved through optical microscopy.

I.2.2 Studying amyloids at the molecular level

Molecular level study of amyloids can be thought to begin at approximately 1959, with the first electron micrographs showing that amyloids consisted of fibrillar aggregates (Cohen and Calkins 1959). X-ray fiber diffraction of amyloids showed that these fibrils had cross-β structure (Eanes and Glenner 1968; Bonar et al. 1969), a structural motif formed from β-strands running perpendicular to the fiber axis, forming β-sheets along the fibril. Cross-β structure had initially been seen in denatured egg whites (Astbury et al. 1935) and super-contracted epidermin (Rudall 1946), but much better characterized in the egg-stalk of lacewing flies (Parker and Rudall 1957; Geddes et al. 1968). At that point, what are now considered the hallmarks of amyloid were established: birefringence on Congo red binding, fibrillar ultrastructure, and cross-β molecular structure. However, information regarding the identity of amyloid-forming proteins was scarce until the identification of immunoglobulin by protein sequencing of purified amyloid (Glenner et al. 1970). Other amyloid forming proteins were identified including the systemic amyloidosis-related serum amyloid A (Levin et al. 1973), familial amyloidotic polyneuropathy-related transthyretin (Costa et al. 1978), diabetes-related insulin amyloid precursor protein (Westermark et al. 1986), the Alzheimer's-related Aβ (Glenner 1988) and tau (Wischik et al. 1988), and the Parkinson's-related α-synuclein (Spillantini et al. 1997). In addition to characterizing amyloids extracted from tissues, it was becoming recognized that globular proteins could be induced to form fibrils with characteristics of amyloid (Glenner et al. 1974). With the formation of Congophilic fibrils with cross-β structure *in vitro*, the general definition of amyloid shifted from the fibrils accumulated in amyloid diseases to any fibril which met those molecular requirements.

While it is established that amyloid diseases can have a wide range of proteins, the role of amyloids in disease is still poorly understood. A general framework for understanding amyloid diseases is the amyloid cascade hypothesis that was developed for Alzheimer's disease (Hardy and Allsop 1991; Hardy and Higgins 1992). The basic premise is that the formation of amyloid triggers a set of events that leads to a pathological state. While temporal features of amyloid diseases tend to be consistent with this hypothesis, it is still

unknown whether the amyloid itself causes pathology or if oligomers or protofibrils formed by the same proteins are the pathological agents (Haass and Selkoe 2007; Glabe 2008; Nicoll et al. 2013).

I.2.3 Functional amyloids

In addition to pathological amyloids, a number of functional amyloids have been found. Curli fibers are amyloids produced by *Escherichia coli* and other *Enterobacteriaceae*, which make use of these filamentous structures in the colonization of inert surfaces and formation of biofilms (Barnhart and Chapman 2006). In humans, Pmel17 serves as a functional amyloid associated with melanosome maturation (McGlinchey et al. 2009), and a number of peptide hormones are thought to be stored in secretory granules as amyloids (Maji et al. 2009). Functional amyloids appear to exploit the self-assembly properties of cross-β structure, but under regulated conditions. Curli and Pmel17 are expressed as non-aggregated proteins, but controlled proteolytic cleavage produces the aggregating peptides (Barnhart and Chapman 2006; Rochin et al. 2013). Peptide hormone amyloids fibrillize under the conditions found in secretory granules, but dissociate into monomers upon release into cytosolic conditions (Maji et al. 2009). These are distinct from the functional prions described above, as those appear to go into their amyloid states spontaneously.

I.3 Pathological amyloids as prions

It is becoming increasingly apparent that many amyloid diseases may have prion-like features (Aguzzi 2009; Frost and Diamond 2010; Prusiner 2012; Ashe and Aguzzi 2013). These features include propagation of pathology from initial points within a tissue or organism, diversity of phenotypes possibly caused by a strain-like mechanism, and the ability to elicit disease-states from exogenous sources. Proteins that appear to have prion-like properties include the Alzheimer's-related Aβ (Stöhr et al. 2012) and tau (Guo and Lee 2011), Parkinson's related α-synuclein (Volpicelli-Daley et al. 2011), and the amyotrophic lateral sclerosis superoxide dismutase-1 (Münch et al. 2011). Some researchers have been hesitant to expand the designation of prions to include these amyloid diseases because of

the transgenic systems used in transmission studies and the fact that these diseases have not been shown to be transmissible under normal circumstances. However, Parkinson's-like neurodegeneration (Luk et al. 2012) and systemic amyloidosis (Lundmark et al. 2002) have been transmitted to non-transgenic mice and β-amyloidosis was seeded in non-transgenic marmosets (Ridley et al. 2006). These transmission experiments resemble those showing transmission of CJD to chimpanzees (Gibbs et al. 1968); CJD is classified as a TSE but is not considered transmissible under normal circumstances.

Over the course of time, the definitions of prion and amyloid have changed to fit the current state of knowledge. What we now know as prions were originally thought to be slow viruses, and when that became unlikely, was generally referred to as the scrapie agent. After the discovery of prions, the term became synonymous with the TSE causing agent, until it was found that yeasts were able to transmit phenotypic states using only proteins. The term amyloid initially referred to what were thought to be starchy deposits, was amended to the proteinaceous aggregates found in amyloidoses, then to any protein assembly that exhibited birefringence on Congo red binding, showed fibrils under EM, and gave cross-β X-ray diffraction patterns. The evolution of both these terms has been driven by advances in their molecular understanding. At the molecular level, prions are simply proteins that catalyze a self-propagation effect and produce a phenotype under biological conditions. This definition does not require a prion to be an amyloid, as oligomers and protofibrils may turn out to be prions as well, but amyloids have been shown to have this self-propagating activity. In the cases of the amyloids discussed in this section, amyloid fibrils were sufficient to transmit disease-like properties. Insights into the basic mechanisms of self-propagation are required for broad understading of these diseases.

I.4 HET-s(218–289) as a model prion

HET-s(218–289) is the prion-forming domain of HET-s, a functional prion in the fungus *Podospora anserina* (Saupe 2011). HET-s(218–289) has been shown to be necessary and sufficient for reproducing the function of the full protein (Maddelein et al. 2002; Balguerie et al. 2003). HET-s is used as a mating-type determinant; upon cell fusion with another

mating-type expressing a homologous protein, HET-S, HET-s prions cause a cell-death reaction to prevent genetic transfer (Saupe 2011; Seuring et al. 2012). While the biological function of HET-s is interesting, our studies of HET-s(218–289) use it as a model prion, owing to its very robust self-assembling and self-propagating properties.

HET-s(218–289) can be fibrillized into prions or non-infectious amyloids by controlling the pH of the fibrillization buffer (Sabaté et al. 2007). At physiological pH, HET–s(218–289) forms infectious fibrils that exhibit a high degree of order and homogeneity. These features made infectious HET-s(218–289) amenable to solid state NMR (ssNMR) analysis, which resulted in an atomic resolution structure: a repeating two-rung β-solenoid (Van Melckebeke et al. 2010). At low pH, HET-s(218–289) forms non-infectious amyloids that have heterogeneous morphologies and properties (Sabaté et al. 2007; Sen et al. 2007). ssNMR studies of low pH fibrils indicated that they have structures significantly different from those of the physiological pH fibrils (Wasmer et al. 2008b). Low resolution models of one- and three-protofilament fibrils formed under acidic conditions have been obtained by cryo-EM, though these studies have suggested structures similar to the β-solenoid (Mizuno et al. 2011).

HET-s(218–289) is a useful model prion for studying the biophysical interactions of different types of amyloids. Unlike the prions of *S. cerevisiae* (Kabani and Melki 2011; Holmes et al. 2013), HET-s(218–289) is not Q/N rich, making its amino acid composition similar to those of most other pathological amyloids. While HET-s(218–289) is smaller than the putative prion-forming domain (the proteinase K-resistant core) of PrP (Legname et al. 2004), it is large enough to form a complex amyloid structure that is fundamentally irreproducible in short peptide systems (Sawaya et al. 2007). HET-s(218–289) forms polymorphs that are not strains in that they do not faithfully reproduce a phenotype (Sabaté et al. 2007). This may be partly caused by the function of HET-s as a molecular trigger for a cell death process, and by evolution to fold reproducibly under physiological conditions. However, this evolved reproducible fold allows us to gain insights into the properties that differentiate prions from other amyloids, that is, the particular properties that allow for self-propagation.

In this work, we have used X-ray fiber diffraction to characterize the structure of HET-s(218–289) polymorphs and site-directed mutants. We characterized biophysical properties

of these polymorphs and mutants using methods which include fibrillization kinetics and chemical stability assays. Our results provide insights into the stability of HET-s(218–289), the interaction between the prion and non-prion forms of HET-s(218–289), and the role of particular structural interactions in the reproducible folding of HET-s(218–289).

CHAPTER II

X-ray fiber diffraction of amyloids

II.1 The theory of fiber diffraction

II.1.1 General properties of fiber diffraction

Fiber diffraction is a diffraction method used to study the structure of filamentous assemblies. In some respects, fiber diffraction can be thought to lie between solution scattering and crystallographic diffraction, with particular types of specimens leaning towards one method or the other. This is in part caused by a fundamental feature of filamentous assemblies – they are periodic along the fiber axis. In effect, a fibrous assembly is a one-dimensional crystal, though its "unit cell" can have a very wide range.

Fiber diffraction specimens can take on different filament arrangements, each resulting in different types of diffraction patterns (Chandrasekaran and Stubbs 2012). One common feature of fiber diffracion patterns is cylindrical averaging, which occurs because specimens are generally composed of many individual filaments that are randomly oriented about their fiber axes. Another common aspect is that the one-dimensional crystallinity along the fiber axis produces a diffraction pattern that is crystalline on the axis parallel with the fiber axis. In some cases, individual filaments can aggregate together to form three-dimensional crystals, though these crystals tend to be very small, so diffraction specimens will generally consist of bundles of randomly oriented microcrystalline fibers (Figure 1A). This polycrystalline specimen produces a fiber diffraction pattern that is equivalent to rotating a single crystal about an axis during an exposure. Non-crystalline specimens are formed when the individual filaments are not arranged into regular arrays. Non-crystalline specimens (Figure 1B) give rise to continuous fiber diffraction data, where the data perpendicular to the fiber axis are continuous instead of being sampled through a crystal lattice. These continuous data are similar to the continuous data in solution scattering. An intermediate type of specimen can be formed, where the individual filaments form a regular paracrystalline array (Figure 1C), which does not have the regularity of a true three-dimensional crystal.

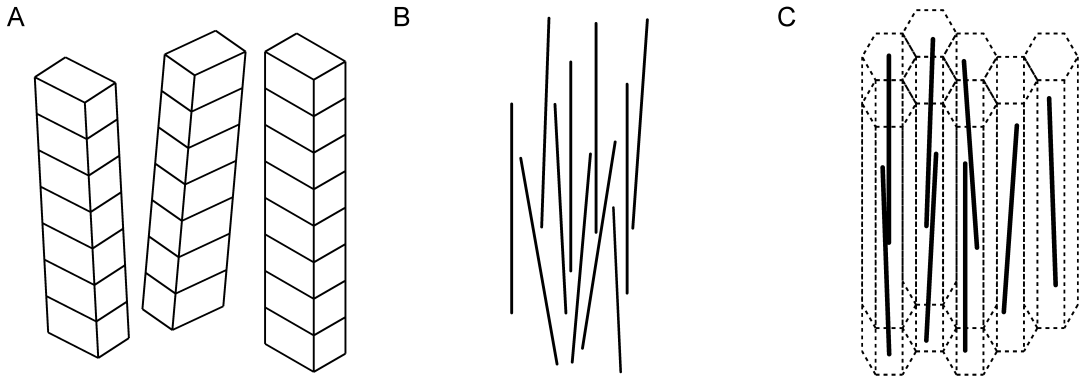

Figure 1: Types of fiber diffraction specimens. A) polycrystalline, B) non-crystalline, and C) paracrystalline.

The type of fiber diffraction specimen formed is related to both the nature of the filamentous assembly and the conditions of preparation. Polycrystalline specimens include naturally crystalline biological filaments such as muscle (Reconditi 2006), collagen (Orgel et al. 2006), different types of silks (Marsh et al. 1955; Geddes et al. 1968; Bram et al. 1997), and filaments with small repeating units such as polysaccharides (Arnott et al. 1974; Nishiyama et al. 2002) and A-DNA (Franklin and Gosling 1953; Arnott 2006). Larger macromolecular structures such as filamentous viruses (Namba et al. 1989; Marvin et al. 1994; McDonald et al. 2010), F-actin (Oda et al. 2009), and microtubules (Beese et al. 1987; Sugiyama et al. 2009) tend to form non-crystalline diffraction specimens, as does B-DNA (Franklin and Gosling 1953; Arnott 2006). Orientation of certain specimens can induce the formation of paracrystallinity such as in flagellar filaments (Yamashita et al. 1998) and bacteriophage (Marvin et al. 1994), leading to continuous fiber diffraction patterns with crystalline sampling at low resolutions. Transitions between non-crystalline and polycrystalline states can be induced by sample conditions such as relative humidity or salt-concentration, as most notably seen with the transition between A-DNA and B-DNA (Franklin and Gosling 1953; Arnott 2006). While short-amyloidogenic peptide fibrils form both polycrystalline and non-crystalline specimens (Inouye et al. 1993), larger amyloids tend to form non-crystalline specimens (Kishimoto et al. 2004; McDonald et al. 2012; Wan

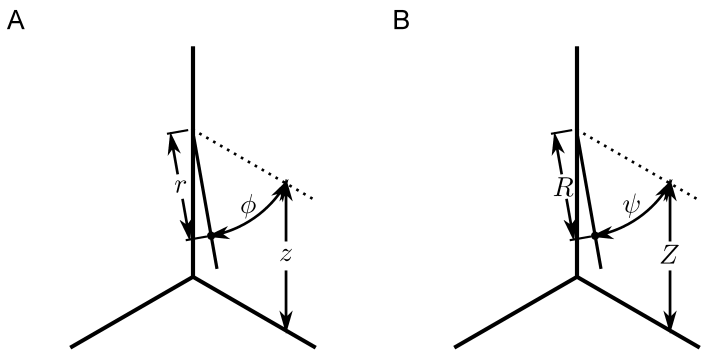

Figure 2: Cylindrical coordinates. A) Real space. B) Reciprocal space.

et al. 2013), or paracrystalline specimens (Wille et al. 2009). As such, the following sections will primarily focus on non-crystalline fiber diffraction.

II.1.2 Fourier methods in fiber diffraction

As with all diffraction methods, fiber diffraction results in the production of a diffraction pattern which represents the Fourier transform of the specimen. In-depth explanations of general principles of X-ray diffraction can be found elsewhere (Lipson and Taylor 1958). In the case of non-crystalline specimens, fibre diffraction patterns represent the cylindrically averaged Fourier transform of an individual fibril. For fiber diffraction, it is generally more convenient to use a cylindrical coordinate system, with r, ϕ, and z representing the real space coordinates for distance from the fiber axis, azimuthal angle around the fiber axis, and distance along the fiber axis, respectively (Figure 2A). The corresponding reciprocal space coordinates are R, ψ, and Z (Figure 2B).

Fiber diffraction data fall only on "layer lines," planes of reciprocal space that are separated by a distance related to the periodicities along the length of the fibril. The Fourier transform, or structure factor, of the fibril in cylindrical coordinates is generally (Chandrasekaran and Stubbs 2012) given as:

$$\mathbf{F}(R, \psi, \frac{l}{c}) = \sum_n \mathbf{G}_{n,l}(R)\ \exp[in(\psi + \frac{\pi}{2})], \tag{II.1}$$

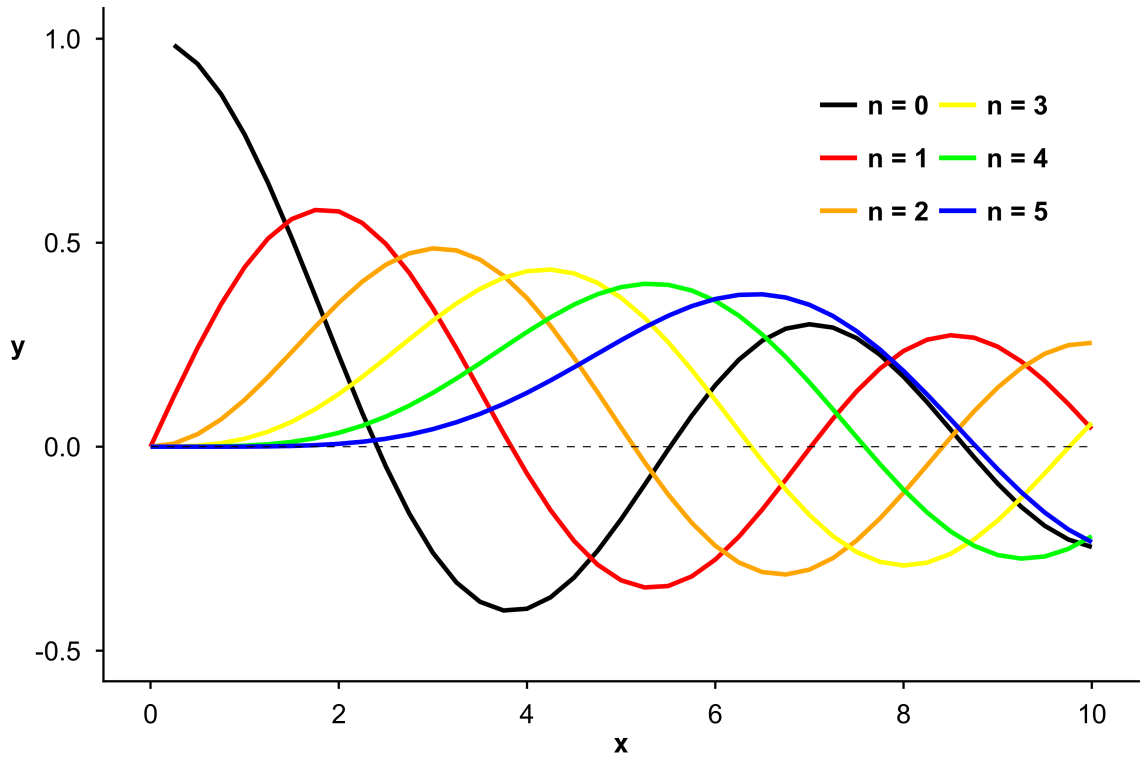

Figure 3: Bessel functions. Plots of Bessel functions of the first kind with order n.

where Z is equivalent to $\frac{l}{c}$, and l is the layer line number, c is the distance of one repeat along the fibril, and $\frac{1}{c}$ is the spacing between layer lines in reciprocal space. The summation is over n, the order of each Bessel function in the Fourier-Bessel structure factor $\mathbf{G}_{n,l}(R)$. The Fourier-Bessel structure factor is given as:

$$\mathbf{G}_{n,l}(R) = \sum_j f_j \, J_n(2\pi r_j R) \, \exp[i(-n\phi_j + 2\pi z_j \frac{l}{c})], \tag{II.2}$$

where the summation is across every atom j in the protomer, and J_n is a Bessel function of the first kind with order n. Bessel functions are cylindrical functions which take the appearance of attenuating sinusoidal functions, which reach appreciable amplitude with larger argument values; increasing Bessel orders increase this argument value required for appreciable amplitude (Figure 3).

The recorded intensity of the diffracted X-rays, I, is generally given by the complex conjugate of the structure factor, but the addition of cylindrical averaging in fiber diffraction results in:

$$I(R,l) = \sum_n \mathbf{G}_{n,l}(R)\,\mathbf{G}^*_{n,l}(R) = \sum_n |\mathbf{G}_{n,l}(R)|^2 \tag{II.3}$$

where the intensity on each layer line is related to only the reciprocal distance R, but not on the reciprocal azimuth ψ. Derivations of these equations can be found from first principles (Cochran et al. 1952; Franklin and Klug 1955; Klug et al. 1958), or by converting the Cartesian structure factor to cylindrical coordiantes (Cantor and Schimmel 1980), each of which provides particular insights.

The appearance of a Bessel function of order n on a layer line is restricted by a selection rule:

$$l = tn + um \tag{II.4}$$

where t is the number of turns per repeat, u is the number of subunits per repeat, and m is an integer. For fibrils where individual subunits are stacked with no twist, that is, a true one-dimensional crystal, $t = 0$. In all other cases, the fibril is helical.

The above equations define the diffraction pattern in terms of the sum of contribuations from atoms, each with its own helical parameters, but it is equally valid to think of the diffraction pattern in terms of a protomer and basic discontinuous helix (Cochran et al. 1952). The discontinuous helix itself is the product of a continuous helix and a set of planes (Figure 4A-C). In reciprocal space, the transform of a continuous helix falls on layer lines spaced with the reciprocal of the pitch, P, (Figure 4D), while the Fourier transform of the set of planes takes the form of points separated by the reciprocal of the plane spacings, p, (Figure 4E). In terms of an actual fibril, p is the vertical translation between protomers, that is, distance between subunits with respect to the z axis. The Fourier transform of the discontinuous helix is equivalent to the convolution of the transform of the continuous helix

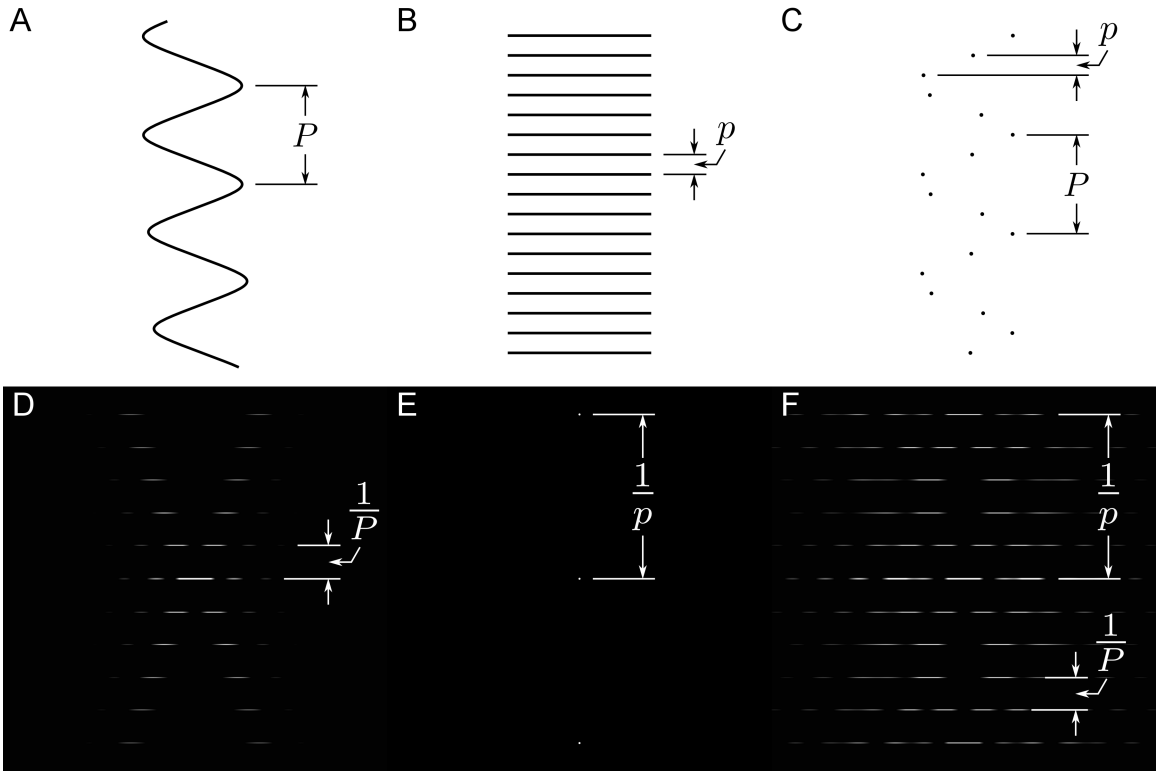

Figure 4: Components of a discontinuous helix in real and reciprocal space. A) Continuous helix, B) set of planes, and C) discontinuous helix in real space. Fourier transforms of D) continuous helix, E) set of planes, and F) discontinous helix.

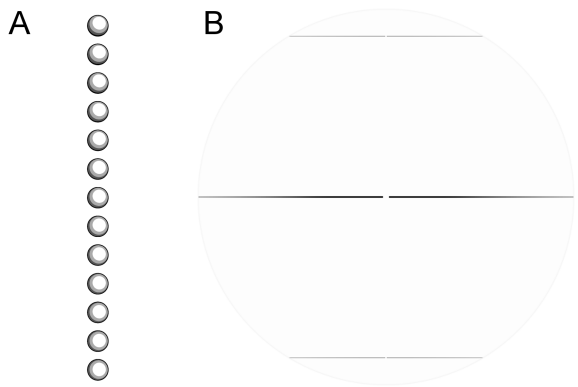

Figure 5: Transform of a row of carbon atoms. A) A row of carbon atoms with no twist, and B) its Fourier transform.

onto the transform of the set of planes, resulting in layer lines with distances equal to the reciprocal of the repeat distance.

In real space, the fibril is a convolution of a basic discontinuous helix and each subunit, while in reciprocal space the diffraction pattern is the product of the transform of the basic discontinuous helix and the transform of the subunit. Another way of stating this is that the transform of the subunit is sampled by the transform of the basic discontinuous helix. The helical transform results in Bessel functions spread over different layer lines according to the selection rule. The transform of a continuous helix (Figure 4D) is an X shape formed by the intense initial maxima of the increasing Bessel orders; this X shape is a characteristic feature of helical diffraction. The discontinuous helix results in a new helical X shape every time $Z = \frac{1}{p}$ (Figure 4E). For the special case of a true one-dimensional crystal, where there is no twist between subunits, all Bessel orders fall on every layer line (Figure 5). In this case, the only sampling that occurs is the formation of layer lines. One common property in all cases is that the only diffraction that is truly on the meridian is at spacings of $Z = \frac{1}{p}$, and this is always from J_0.

Cylindrical averaging causes a loss of data related to the reciprocal azimuthal angle, resulting in two-dimensional data. One effect of this is that all of cylindrically averaged reciprocal space can be represented by a single plane (Figure 6). However, a diffraction pattern represents a spherical sample through reciprocal space (Figure 6), so it is impossible

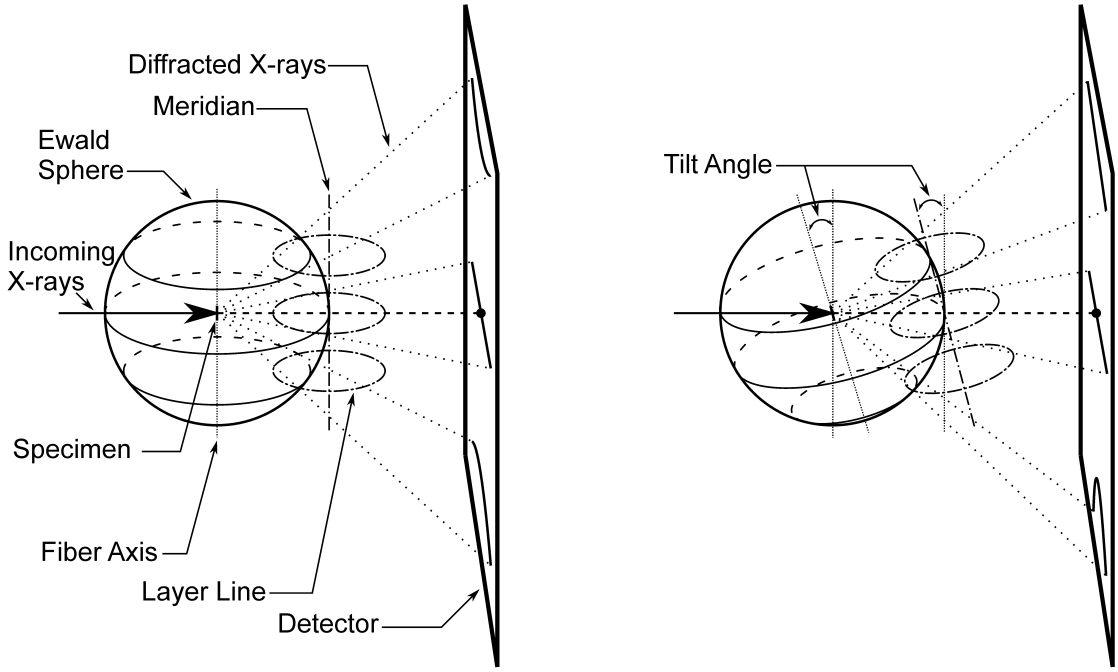

Figure 6: Ewald sphere gemoetry in fiber diffraction. Left: No tilt. Right: Tilted to allow for collection of meridional data on the upper layer line.

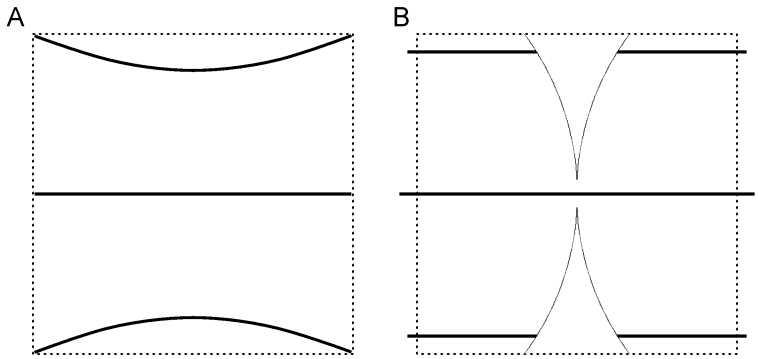

Figure 7: Detector and reciprocal space. A) A diffraction pattern recorded in detector space and B) transformed into reciprocal space. Curved line in B) represents edge of "blind region".

to obtain a full view of reciprocal space with a single diffraction pattern. The unsampled region of reciprocal space is the so-called "blind region," which can be sampled by tilting the specimen, which results the in tilting of reciprocal space (Figure 6, 7). In addition to the "blind region", the curved sampling of reciprocal space results in layer lines taking the shapes of hyperbolas in detector space (Figure 7). By mapping each recorded diffraction pattern from "detector space" to a plane of reciprocal space (Fraser et al. 1976), the full plane of reciprocal space can be reconstructed by overlaying tilted diffraction patterns (Shotton et al. 1998). This geometric correction also remaps the hyperbolas in detector space to layer lines.

II.1.3 Special considerations for amyloid diffraction

The fundamental feature of amyloids is that they are composed of cross-β structure (Astbury et al. 1935; Eanes and Glenner 1968). The core of a cross-β structure consists of β-strands running perpendicular to the fiber axis, forming β-sheets that run parallel to the fiber axis (Rudall 1946). The inter-strand spacing within a β-sheet is generally 4.7–4.8 Å. Subunits in cross-β structures contribute one or more β-strands to the core, with a special condition that single β-strand subunits that arrange in an anti-parallel β-sheet diffract as a two-strand repeating unit. Since the nature of cross-β structure requires that the subunits stack on top of one another in order to form inter-strand hydrogen bonds, the meridional

reflection distance p will be equal to the subunit height, and will be a multiple of ~4.7 Å. The ~4.7 Å meridional reflection is generally the most intense, owing to the large representation of the ~4.7 Å periodicity within the subunit.

Cross-β structure limits the helical twist of the fibrils to small angles. This is caused by the direct stacking of subunits; too high a twist will prevent the formation of correct inter-strand hydrogen bonding. This results in very long helical pitches, and very small $\frac{1}{P}$ values, making the layer lines closer together. The selection rule given above was formulated for comparisons of helices with integral numbers of turns and subunits per repeat, but for amyloids, a more useful formulation may be given as:

$$Z = \frac{1}{P}\, n + \frac{1}{p}\, m. \tag{II.5}$$

With this formulation, m is an identifier for each helical X, that is, m refers to a helical order. n is both the Bessel order and the integer multiple of $\frac{1}{P}$, which provides the Z distance from the closest m. Amyloids also tend to have thin fibril radii, which results in spreading of the Bessel fuction maxima along each layer line. The combination of small $\frac{1}{P}$ and spread Bessel maxima results in more acute angles of the helical X, so in practice, the Bessel functions of each helical order, m, do not overlap with other helical orders, except at higher resolutions where diffraction intensity is low.

II.1.4 Theoretical and practical effects of disorientation

The individual fibrils within a fiber diffraction specimen are never perfectly aligned. While misalignment about the fiber axis results in cylindrical averaging, misalignment of the fiber axes of individual fibrils results in disorientation. A full theoretical account of disorientation is given elsewhere (Holmes and Barrington Leigh 1974), but the salient points in amyloid diffraction are given below.

Disorientation is a localized property which is only observed in the region of the specimen that diffracts the incoming X-rays. The particles within a region are generally oriented about a common axis, which is the apparent meridian in the diffraction pattern (Figure 8).

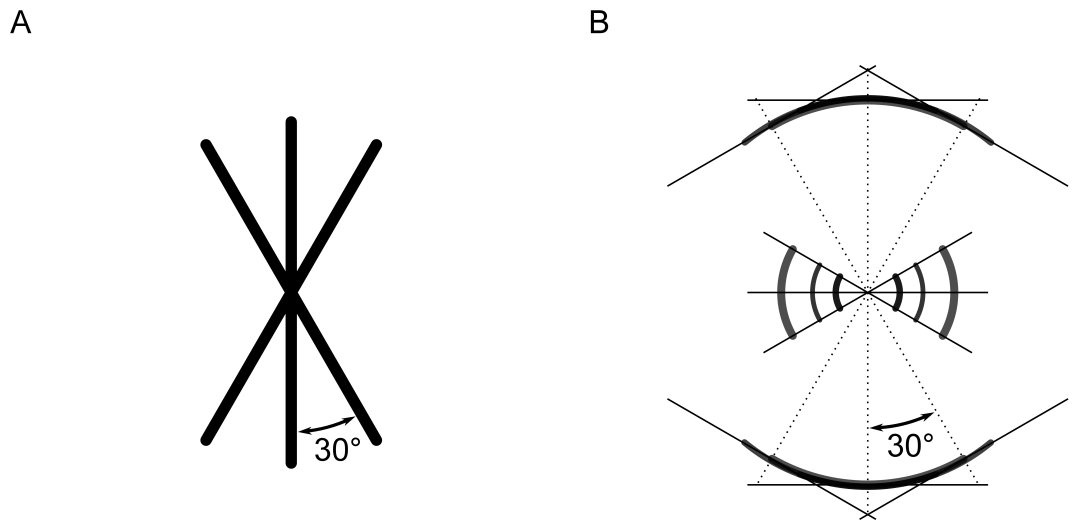

Figure 8: Real and reciprocal space geometry of disorientation. A) Three fibrils at different angles and B) their intensity distributions in reciprocal space.

The meridian is not necessarily aligned with the long axis of the specimen, and the angle between the reciprocal space axes and the detector space axes is called the twist angle. The distribution of individual fibrils about the common axis is assumed to be Gaussian in three-dimensions, resulting in a cone-shaped distribution, though practically, disorientation on a diffraction pattern is well approximated as two-dimensional (Stubbs 1974). High levels of disorientation result in the diffraction pattern smearing into Debye-Scherrer arcs. Less severe disorientation results in the equator smearing into arcs, while the meridional data form caustics (Figure 8). Off-meridional data are not quite arcs centered at the origin of the diffraction pattern, but are approximately so. Equatorial arcs formed by disorientation have a Gaussian profile related to the distribution of the fibrils within the specimen. The disorientation angle is the standard deviation of the angular disorientatoin. In some instances, diffraction patterns may appear as multiple diffraction patterns superimposed on one another, indicating that the incoming X-rays passed through multiple oriented domains, each with its own common orientation axis.

In practice, amyloid fiber diffraction specimens tend to have high to complete disorientation. This is likely to be caused by inherent disorder and high flexibility of amyloid

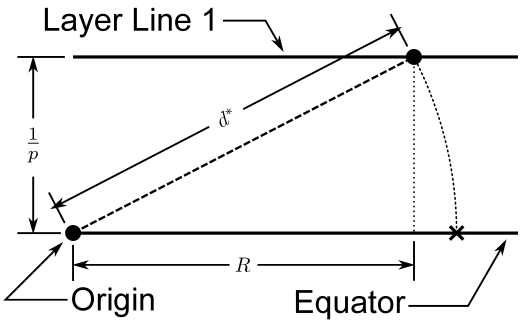

Figure 9: Disorientation geometry on the equator.

fibrils. The effect of this on amyloid diffraction patterns is the inability to deconvolute the individual Bessel functions, thus preventing direct structure determination. On the equator, the convolution of the $m = 0$ Bessel functions results in the inability to measure R values, as they effectively convolute into d^* values (Figure 9). The angular convolution of R into d^* is approximately independent of the disorientation angle, allowing for the use of radially integrated intensity plots, called sector plots, for quantitative analysis. Meridional data cannot be used in the same way, owing to the caustic shape caused by disorientation, which is dependant on the disorientation angle. Data that are sufficiently off meridional should be usable for quantitative analysis, but are generally not used owing to difficulty in accurately measuring intensities.

While sufficient orientation of amyloid fiber diffraction specimens to allow for Bessel function deconvolution is unlikely in practice, it is still best to obtain as much orientation as possible. Low disorientation allows for clear delineation of meridional, off-meridional, and equatorial data, providing a two-dimensional data set rather than a one-dimensional scattering profile. This delineation allows for more precise measurements of maxima positions and meridional spacings. In addition, well oriented data allow for more accurate background subtraction and intensity integration, which will be discussed in more detail in later sections.

II.2 Specimen preparation and data collection

II.2.1 Types of fiber diffraction specimens

In the previous section I discussed types of fiber diffraction in terms of crystallinity within the specimen. In this section I will discuss types of specimens with respect to their method of preparation. While the method of preparation may influence the crystallinity of the specimen, all levels of crystallinity may be seen in any type of specimen, so there is no general direct relationship between preparation method and resultant crystallinity.

Fiber diffraction specimens are prepared with the ultimate goal of maximizing orientation of the fibrils within specimens. As such, specimens can take on many forms including oriented sols (Gregory and Holmes 1965; Kendall and Stubbs 2006), continuously shear-flowed solutions (Sugiyama et al. 2009; Squires et al. 2006), dried fibril solutions in the form of discs (Morris and Serpell 2010), and fibers (McDonald et al. 2008). Each type of specimen has its own strengths and weaknesses, with some being better suited for particular types of applications.

Amyloid structure can be severely impacted by specimen hydration (Kishimoto et al. 2004), and oriented sols and continuously shear-flowed solutions are the most hydrated types of specimens, though in our experience these types of specimens are not amenable to amyloid diffraction. This limitation appears to be caused by large hydration shells surrounding fibrils, even after prolonged ultracentrifugation, resulting in very weak amyloid diffraction with respect to bulk solvent. This further compounds the inherently weak diffraction of amyloids, which is caused by structural disorder. Amyloid specimen orientation is also poor using these methods, which is likely caused by the inability of concentrated solutions to flow-align (Figure 10), possibly because of the high flexibility of amyloid fibrils. Fibrils that behave like rigid rods, such as tobacco mossaic virus, bacterial flagellin, and F-actin have been shown to be well suited for oriented sols prepared by flow-alignment (Gregory and Holmes 1965; Yamashita et al. 1991; Yamashita et al. 1998; Oda et al. 1998; Kendall and Stubbs 2006).

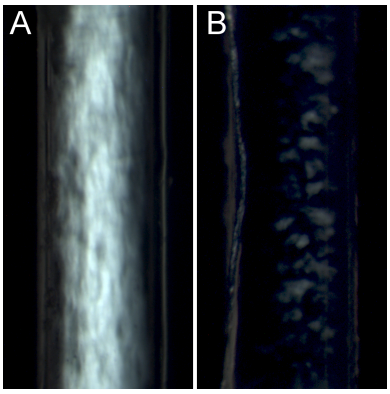

Figure 10: HET-s(218–289) sol under crossed-polarizers. Sol is at A) 45° and B) 90° with respect to polarizer direction. Banding indicates unfused oriented domains, despite flow-alignment and several years of standing.

In order to lower background scatter from bulk solvent, fiber diffraction specimens can be formed by drying concentrated amyloid solutions. While dried amyloid fibrils can undergo structural distortion, maintaining dried specimens at high relative humidities appears to reproduce the hydration state of non-dried specimens (McDonald et al. 2008). In our experience, drying a droplet of amyloid solution between two rods in order to form a dried fiber-like specimen induces greater orientation in specimens. A detailed account of considerations for forming dried fiber specimens is given below.

II.2.2 Preparation of dried fiber specimens

The goal of dried fiber specimen preparation is to orient the individual fibrils within a droplet of amyloid solution about a common axis. This is accomplished by hanging a droplet between two rods and allowing them to dry (Figure 11). As the droplet dries and the volume decreases, surface tension and volume exclusion effects cause the individual fibrils to align. When the droplet finishes drying, a dried fiber is formed, with the individual fibrils aligned approximately parallel to the long axis of the fiber. Long and thin dried fibers tend to have the greatest orientation, but thin fibers have weaker diffraction and may be difficult to algin with the X-ray beam. The formation of well oriented dried fibers depends on a number of factors including fibril solution conditions, the types of rods used, and the drying conditions.

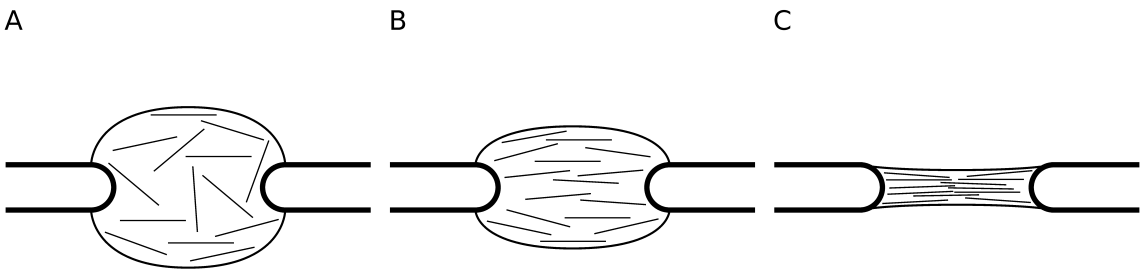

Figure 11: Diagram of a drying droplet of amyloid solution. A) Wet, B) partially dried and C) dry.

Amyloid solutions that yield well oriented fibers tend to consist of purified, well dispersed fibrils, free of large fibrillar aggregates. Fibrillar aggregates can be eliminated by removal with differential centrifugation, by dispersal into individual fibrils, or a combination of the two. Fibrillar aggregates can be dispersed by adjusting buffer conditions or fracturing aggregates. Buffer type and pH can affect the aggregation state of amyloids, but drying results in concentration of buffer salts which can lead to buffer salt crystallization within the dried fiber. This results in crystalline diffraction from the buffer salt superimposed on the fiber diffraction pattern. One way to prevent this is by lowering buffer concentrations or by using volatile buffers. Fracturing of fibrillar aggregates can be done with repeated freeze-thaw cycles or by sonication. While over-fracturing can result in loss of structure and formation of amorphous aggregates, mild fracturing can be beneficial to specimen orientation by shortening fibrils, which lowers their overall flexibility. Ideally, solutions will be clear and free of aggregates while still having sufficient fibril concentration to form a dried fiber. In cases where ideal conditions cannot be found, it may still be possible to form dried fibers, but with substantially lower orientation.

The concentration of the fibril solution can be an important factor in producing well oriented dried fibers. As a droplet dries and the fibril concentration increases, the solution forms a liquid crystalline phase. Droplets that are already liquid crystalline before drying tend to contain many different oriented domains, which do not coalesce upon drying (Figure

12A, B, E, F, I, J). If the starting droplet is at a low enough concentration where no liquid crystalline domains exist, drying results in the formation of a single liquid crystalline domain (Figure 12C, D, G, H, K, L). As a rule of thumb, 20 $\frac{\text{mg}}{\text{mL}}$ is a good starting concentration, but the formation of liquid crystalline phases is dependent on factors than are difficult to control, such as fibril length, so polarization microscopy is a more practical method to determine optimal fibril concentrations. If fibril solutions are too dilute to produce a dried fiber, solutions can be concentrated by ultracentrifugation or additional solution can be added to the fiber as it dries, though this may not yield as well oriented fibers.

We have found that extended drying times aids in obtaining well oriented dried fibers. Extended drying times may provide more time for the individual fibrils within the droplet to reorient into optimal low energy packing arrangements. In order to increase drying times, it is important to allow the specimen to dry under high relative humidity conditions. This can be accomplished by drying in a sealed chamber with a saturated salt solution, which provides up to ~98 % relative humidity (RH), or with water, which provides nominal 100 % RH. Drying times can be further extended by lowering the temperature of the drying chamber. We have found that drying specimens at 4 °C substantially increases the drying time compared to drying at room temperature.

The types of rods used for hanging droplets can have a significant influence on the resultant fiber. The size and shape of the rod ends (Figure 13) affects the amount of solution that can be suspended between the rods, as well as the size of the gap between the rods. Longer gap distances allows for the formation of longer and thinner dried fibers, which can improve specimen orientation. Rods used for hanging amyloid solutions tend to be made from glass capillaries, which are normally hydrophillic. As such, a hydrophobic coating must be added so the suspended droplets hang rather than coat the glass surfaces (Marvin et al. 1974). This can be accomplished by coating the surface with a layer of wax, or by silanizing the surfaces. We have found that silanized glass tends to be too hydrophobic to suspend a droplet, but silization followed by sanding the tip of the rod produces a surface that can suspend droplets larger than those that can be suspended by waxed capillaries.

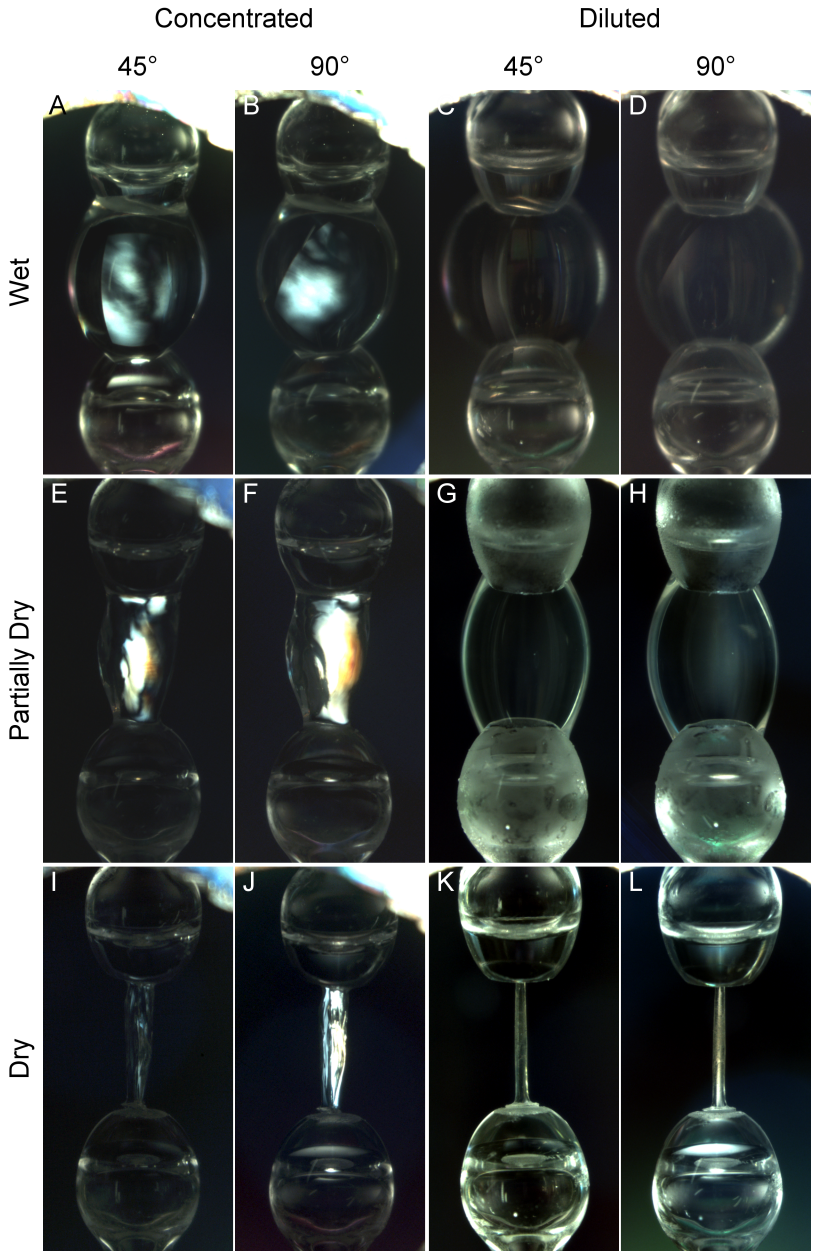

Figure 12: Drying droplets of HET-s(218–289) viewed under crossed polarizers. Concentrated solutions while wet A), B); partially dry E), F); and dry I), J) view at 45° and 90° respectively. Diluted solutions while wet C), D); partially dry G), H); and dry K), L) view at 45° and 90° respectively. Angles are with respect to polarizer direction

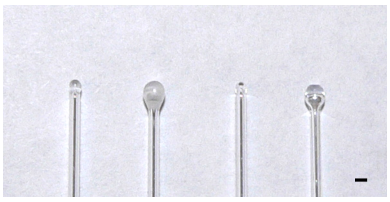

Figure 13: Various types of glass rods. From left to right: flat and bulbous wax tipped, and flat and bulbous silanized and sanded. Scale bar = 1 mm.

Following drying, proper storage of specimens is required to ensure preservation of the specimen prior to collecting diffraction data. Samples must be kept at high humidity, even during data collection, so it is simpler to produce fibers is specimen holders that can maintain high humidity (McDonald et al. 2008). For long term storage, dried fibers remain stable at 4 °C for several months. Depending on the buffer used and the amyloid type, some specimens can become contaminated by fungal growth. This is easily prevented by the addition of sodium azide up to 1 mM. This concentration is sufficient to prevent fungal growth and low enough that it does not interfere with orientation and it does not crystallize when fully dried.

II.2.3 Considerations for data collection

Even for very well oriented specimens, X-ray diffraction from amyloids is weak when compared to other fiber diffraction systems, and very weak when compared to single-crystal diffraction. In order to obtain the best possible signal-to-noise ratio, the use of synchrotron sources is necessary, and the use of beamlines optimized for fiber diffraction is ideal (Tsuruta and Irving 2008). The distinguishing features of a fiber diffraction beamline are a beam size of 100 × 100 µm or smaller, low beam divergence, the use of a beam-tunnel between the specimen and the detector to reduce air scatter, and a broad resolution range. Smaller beam sizes produce better diffraction from thinner specimens, and also allow for probing of smaller oriented domains within the specimen. Beam divergence is also important for obtaining accurate intensities at lower resolutions; beam divergence causes greater intensity near the beamstop, which results in inaccurate intensities in those regions. The diffraction data near the beamstop is generally the most intense region of the pattern, so increasing

intensity from beam divergence also decreases the exposure time that can be used before oversaturating the detector; this can result in the inability to collect weak diffraction data. For amyloid diffraction, vacuum beam-tunnels are ideal, as even helium can produce a substantial background for weakly diffracting specimens. A wide-angle resolution limit for amyloid diffraction of ~3.5 $Å^{-1}$ is generally sufficient. A low-angle resolution limit of ~100 $Å^{-1}$ is usually sufficient as this can generally allow for detection of low angle maxima or paracrystalline reflections and can allow one to determine if the specimen is polycrystalline. For even lower resolution, it is better to reconfigure the camera setup for medium- to low-angle diffraction (~20–300 $Å^{-1}$), as this will provide greater spatial resolution on the detector and allow for more precise measurements. For particularly well-oriented specimens, a low-angle setup can allow for the separation and Z measurement of the first $J_{\pm 1}$ maxima for helical order $m = 0$, which can allow for direct measurement of the helical pitch.

For quantitative use of fiber diffraction data, it is essential that the background is circularly symmetric. This is because for continuous data, local background subtraction does not work, as there are no distinct reflections, but the space between layer lines should have zero intensity, so the background can be fit to these spaces at each annulus. The components of circularly symmetric scattering will be from air gaps along the beam path and bulk solvent in the specimen, so the setup must have no parasitic scatter. This is partly accomplished by having no extraneous equipment along the beam path, but a lead pinhole immediately before the specimen (~1 mm) eliminates upstream air scatter, which can cause parasitic scatter from the sample rods and sample holder windows.

Precise distance measurements require the use of diffraction calibrants. For wide-angle amyloid diffraction, calcite is a useful internal calibrant. Lightly dusting a dried fiber with calcite produces a calcite powder diffraction pattern with reproducible rings beginning at 3.855 $Å^{-1}$, allowing for direct determination of specimen-detector distance, detector misalignment, and centering of the diffraction pattern without overlapping large amounts of data. For low-angle diffraction, an external calibrant is sufficient as the specimen-detector distance is much longer. Silver behenate produces a characteristic powder diffraction pattern

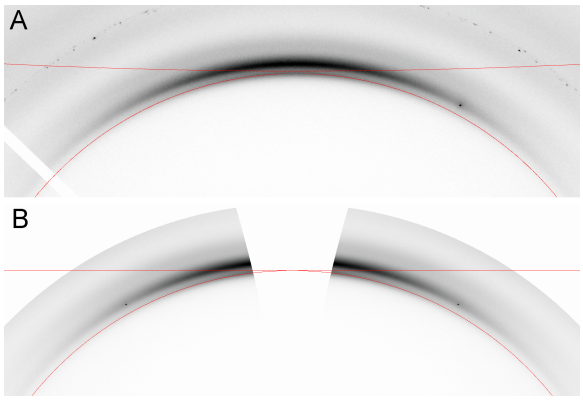

Figure 14: Measuring Z-spacings in detector and reciprocal space. A) Detector space. B) reciprocal space. Red circles represent $d^* = 4.8$ Å and red lines represent $Z = 4.8$ Å

that can be seen in a low-angle setup, and as such is not suitable as an internal standard as it will overlap most of the amyloid diffraction.

II.3 Data processing and comparison

II.3.1 Initial processing of fiber diffraction patterns

Cylindrical averaging makes a central plane through reciprocal space representative of all reciprocal space. As previously discussed, each diffraction pattern is a sampling of reciprocal space through the surface of the Ewald sphere, so no single diffraction pattern can represent a plane of reciprocal space. One side effect of this is that only reciprocal distances can directly be measured on a diffraction pattern (d^*), as the Z and R axes are disorted by the spherical sampling (Figure 7). Even without collecting a tilt-series to reconstruct the blind region, accurate meridional spacings can be determined after transforming the detected pattern from detector to reciprocal space. In general, attempting to directly determine the meridional spacings in detector space results in underestimation of the Z value (Figure 14). The mathematical fomulae for calculating the transformation from detector space to reciprocal space are given elsewhere (Fraser et al. 1976) and can be performed by software such was WCEN (Bian et al. 2006). WCEN can also map detector space coordinates onto reciprocal space, allowing for R and Z measurements of pixels without performing a

transform. In addition to remapping the diffraction patterns, WCEN can apply polarization and Lorentz corrections as well as quadrant averaging.

Before intensities can be accurately measured and compared, background must first be subtracted. As noted earlier, background subtraction in continuous fiber diffraction relies on fitting the background to the blank spaces between layer lines for each annulus of data. In amyloid diffraction, this is actually the space between helical orders, as layer lines within helical orders are convoluted. As such, background subtraction can only be performed if there is sufficient orientation such that the intensities from each helical order do not overlap. In general, accurate intensities can be measured if the disorientation angle is 30° or lower, though this may be less if the structure is more than one β-strand thick. For the most part, only equatorial intensities can be measured this way, since, as discussed previously, meridional data do not convolute into simple arcs and off-meridional data from amyloids is generally limited. The most precise method of background subtraction is probably the one found in the angular deconvolution method (Makowski 1978). This method fits each layer line intensity profile to a Gaussian function and the background to the spaces in between each Gaussian at every annulus. The intensities are then integrated over each Gaussian and the square-root is taken to derive the amplitudes. However, this method was originally devised for specimens with very low disorientation such as tobacco mossaic virus or filamentous bacteriophages, and does not do well with amyloid disorientation angles of more than ~20°. A simpler circularly symmetric approach found in FibreFix (Rajkumar et al. 2005), which has also been added into WCEN, is more suitable for amyloid data. In this approach, at each annulus, intensities of each pixel along the annulus are sorted by increasing intensity and binned into 100 bins (percentage). After binning, the bottom desired percentages are subtracted, i.e. if out of 100 pixels, 1000 is the lowest intensity, then it is the 1 % bin, and subtracting 1 % will result in subtracting 1000 from the entire annulus. While this approach does not directly fit against the blank regions between layer lines, it still requires them to be present, otherwise the smallest bins will contain amyloid diffraction, and as such this method does not work well for disorientation angles over 30°. Diffraction data from fiber diffraction synchrotron beamlines generally deliver very high signal-to-noise ratios, and a

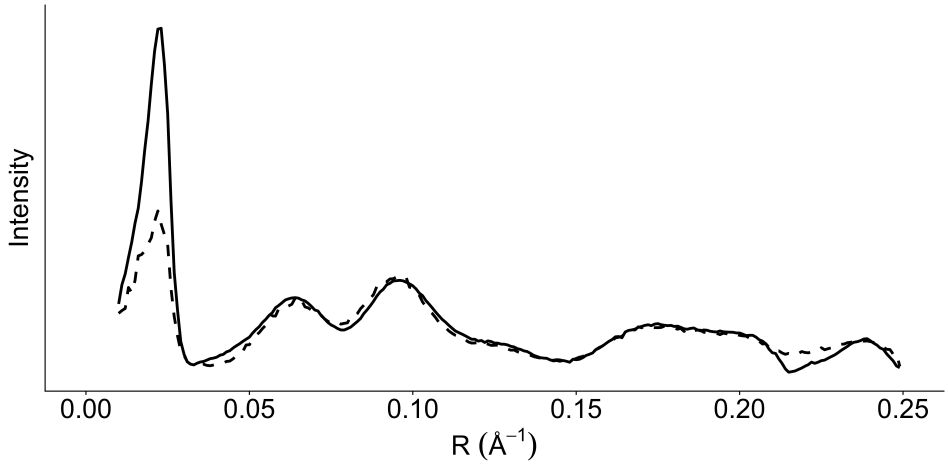

Figure 15: Comparison of background subtraction methods. Traces represent HET-s(218–289) equatorial data after background subtraction using angular deconvolution (solid line) and circularly symmetric subtraction (dashed line).

background subtraction of 1% is sufficient to eliminate background. Intensities can then be integrated using a sector plot – a one-dimensional radial plot that integrates over a given angle around the center of the pattern. Intensities obtained from either method are generally comparable (Figure 15). The main differences between the two methods are at resolutions lower than ~33 Å (0.03Å^{-1}), and the resolution range ~4.7 Å.The lower-resolution data are generally not used in comparative analysis, owing to difficulty in obtaining accurate intensities due to X-ray beam divergence and difficulties in correcting for solvent-contrast effects. The angular deconvolution method over-subtracts around the ~4.7 Å range because of the high intensity and disorientation of the ~4.7 Å reflection. At intermediate resolutions most useful for quantitative amyloid comparisons (33–5 Å, 0.03–0.20 Å^{-1}), the two methods are nearly identical.

II.3.2 Comparing fiber diffraction patterns

Meridional data from amyloid diffraction patterns can generally only be compared qualitatively. This is in part caused by the caustic shapes formed by disoriented meridional reflections as described above, and in part caused by the fact that data along this axis arises from Bragg interference. The number of observed peaks at each interval of ~0.213

$Å^{-1}$ ($\frac{1}{4.7}$ $Å^{-1}$) along the meridian is only equal to the number of strands of each subunit along the fibril axis, so the data are generally too sparse to determine meaningful quantitaive comparisons. Qualitative comparisons such as repeat distances and relative intensities of meridional reflections can be made. Off-meridional data are generally sparse as well as difficult to integrate, so they are also mainly used for qualitative comparisons. By measuring Z distances between the meridional reflections and off-meridional intensities, some assessments regarding how helical the fibril is can be made.

Qualitative comparisons of equatorial data generally make use of the position and relative intensities of diffraction maxima. The positions and relative intensities of diffraction maxima provide information on the periodicities found in the cross-section of the amyloid fibrils. Equators where a single dominant maximum exists indicate a single cross-sectional periodicity, such as the "inter-sheet" maxima found in stacked β-sheet amyloids (Astbury et al. 1935; Eanes and Glenner 1968). Equators consisting of a series of diffraction maxima of comparable intensity indicate a solid core structure, such as that of a β-solenoid (Wille et al. 2009; Wan et al. 2013). Other types of equators can indicate more complex structures such as hollow cylinders (McDonald et al. 2012). Qualitative distinctions can be used to determine overall differences in fibril architectures, but quantitative comparisons can provide a useful metric for comparisons.

Before quantitative comparisons can be made between fiber diffraction patterns, the patterns must be scaled with each other. Since we are generally representing the diffraction data as a plane of reciprocal space, scaling can be accomplished by using a single scaling coefficient across the entire diffraction pattern. The two patterns can be scaled using a common feature of both such as the 4.7 Å meridional reflection. However, the 4.7 Å meridional reflection generally falls within the blind region, so the relative intensity of two patterns is affected by the size of the blind region, which is impacted by specimen tilt angle and wavelength of X-rays used. We find using least squares fitting of equatorial sector plots to be a reliable method of scaling diffraction patterns.

While quantitative comparisons of amyloid fiber diffraction data have been limited, fiber diffraction has generally made use of the R-factor (Stubbs 1989) or the correlation coefficient

(CC) (Gonzalez et al. 1995). The fiber diffraction R-factor is similar in form to that used in crystallography, but is taken as a continuous function across each cylindrically averaged layer line. As such, there is no true free R-factor analog as each data point is correlated with the points around it, and represents the average about the azimuth, though some have omitted resolution shells as a way to produce a free R-factor (Oda et al. 2009). The R-factor is heavily dependent on accurate scaling of the data, which can be difficult to acheive with amyloid data, owing to large disorientation angles and difficulty in correcting for solvent-contrast effects. The CC is generally unaffected by scaling problems as its calculation is adjusted with respect to the mean of each data set. The CC is essentially a comparison of the changes in each data set with respect to their means, across the data set; in effect, it acts as a comparison of maxima rather than of precise intensities at each point. We generally find the CC more useful for amyloid fiber diffraction than the R-factor.

CHAPTER III

Fiber diffraction of HET-s(218–289) fibrillized at physiological pH

III.1 Obtaining well-oriented diffraction patterns

III.1.1 Recombinant protein production and purification

The protein used in our studies is the prion-forming domain of the fungal prion HET-s (Maddelein et al. 2002), residues 218–289 (Balguerie et al. 2003).The plasmid used for the recombinant production of the HET-s(218–289) was provided by Drs. U. Baxa and A.C. Steven (National Institute of Arthritis and Musculoskeletal and Skin Diseases, National Institutes of Health, Bethesda, MD 20892). The construct consisted of synthetic, *Escherichia coli* (*E. coli*) codon optimized, Met-HET-s(218–289)-His6 gene which was cloned into a pET-17b vector (EMD Millipore, Billerica, MA) via NotI/XhoI.

For protein production, the HET-s(218–289) plasmid was transformed into BL21(DE3) competent *E. coli* cells (Life Technologies, Carlsbad, CA) using ampicillin (Reserach Products International, Mount Prospect, IL) (100 $\frac{\mu g}{mL}$) for transformation selection. Transformed cells were grown in ZYM-5052 autoinduction media (Studier 2005) with 200 $\frac{\mu g}{mL}$ ampicillin for approximately 24 h at 37 °C. For optimal aeration, media was limited to 300 mL in 2.8 L baffled Fernbach flasks and shaken at 225 rpm. After growth, cells were pelleted by centrifugation at 5000 × g for 15 min.

Following pelleting, HET-s(218–289) inclusion bodies were purified. The following steps were performed at 4 °C. Cell pellets were resuspended by stirring with a glass rod at a ratio of 3 mL of buffer for each gram of pellet in resuspension buffer (50 mM tris(hydroxymethyl)aminomethane (Tris)-HCl pH 8.0, 100 mM NaCl, 0.1 mM phenylmethylsulfonyl fluoride (PMSF), 5.0 mM ethylenediaminetetraacetic acid (EDTA)). After resuspension, 80 µL of lysozyme (Sigma-Aldrich, St. Louis, MO) solution at 100 $\frac{mg}{mL}$ was added for each gram of cell pellet. The suspension was stirred at 4 °C for 20 min.

Following lysozyme digestion, the *E. coli* suspension was kept on ice and sonicated for a total of 5 min using a 5 s-on, 5 s-off cycle. After sonication, the suspension was centrifuged

at 6000 × g for 15 min. The inclusion body pellet was resuspended in wash buffer (50 mM Tris-HCl pH 8.0, 100 mM NaCl, 0.5 % Trition-X100) with 0.1 mM PMSF, and sonicated as described previously. After sonication, $CaCl_2$ and $MgCl_2$ were added, from 2 M stock solutions,for a final concentration of 10 mM. The inclusion body solution was then digested with 80 µL of 100 $\frac{\text{mg}}{\text{mL}}$ lysozyme and 0.5 U of DNase I (Thermo Scientific, Waltham, MA) per gram of *E. coli* for 40 min at room temperature. The inclusion bodies were then pelleted and resuspended in resuspension buffer three more times. The inclusion bodies were then resuspended in 100 mM Tris-HCl pH 8.0, 100 mM NaCl at the same ratio in as the previous steps, pelleted, and stored at −20 °C until further purified.

HET-s(218–289) was purified from inclusion bodies under denaturing conditions. Inclusion bodies were resuspended at 3 $\frac{\text{mL}}{\text{g}}$ in 20 mM Tris-HCl pH 8.0, 6 M guanidinium (Gdn)-HCl and stirred at room temperature for 30 min. After resuspension, the solution was clarified by ultracentrifugation at 50,000 × g for 45 min. The supernatant was loaded on to a Ni-nitrilotriacetic acid (NTA) column (Qiagen, Venlo, Netherlands) and washed with three bed-volumes of the same buffer. HET-s(218–289) was eluted using 50 mM citric acid pH 2.0, 6 M Gdn-HCl. The HET-s(218–289) fraction was then buffer-exchanged into 150 mM acetic acid pH 2.5, using a Sephadex G-25 superfine column (GE Healthcare Life Sciences, Uppsala, Sweden). Desalted HET-s(218–289) was fibrillized by increasing the pH to 7.5 through titration with 3 M Tris. HET-s(218–289) was fibrillized and stored at room temperature.

III.1.2 Negative stain electron microscopy

To check fibril morphology, HET-s(218–289) fibrils were imaged using negative stain EM. HET-s(218–289) solutions were diluted with water to ~0.5–1.0 $\frac{\text{mg}}{\text{mL}}$ as determined by either absorbance at 200 nm (A280) or bicinchoninic acid protein assay (BCA assay) (Thermo Scientific, Waltham, MA). The diluted HET-s(218–289) solution was adsorbed to 400 square mesh carbon-coated copper grids (Pelco, Redding, CA) for 30 s and blotted with filter paper. The grid was then washed with 7 drops of water and stained with three drops of 1 % uranyl acetate. Grids were allowed to dry and stored in grid boxes at room temperature.

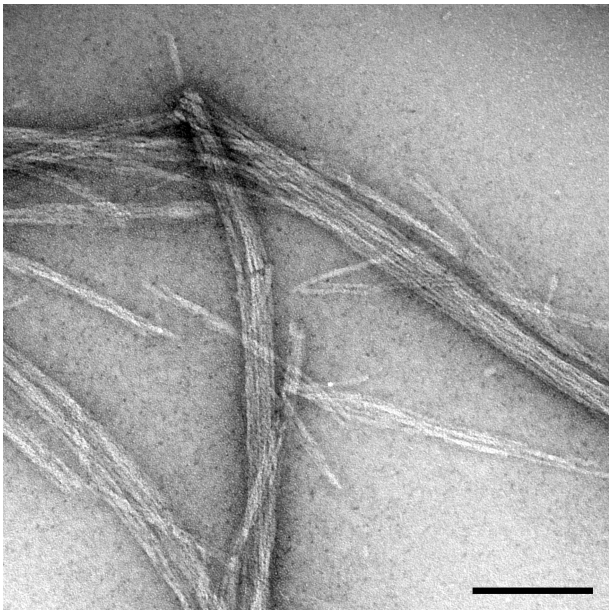

Figure 16: Negative stain EM of HET-s(218–289) fibrillized at pH 7.5. Scale bar = 100 nm

Grids were imaged by transmission electron microscopy on either a Phillips CM12 or a FEI T-12 (FEI, Hillsboro, OR) operating at 80 KeV using a side-mounted 2 k × 2 k charge-coupled device (CCD) camera (Advanced Microscpy Techniques, Woburn, MA), or a Phillips CM20 (FEI, Hillsboro, OR) operating at 200 KeV with a bottom-mounted 2 k × 2 k CCD camera (Advanced Microscpy Techniques, Woburn, MA).

Negative stain EM of HET-s(218–289) fibrils formed at pH 7.5 showed the "cable-like" morphology (Figure 16) previously characterized for infectious HET-s(218–289) fibrils (Sabaté et al. 2007). While morphology does not ensure the same molecular structure, it provided initial evidence of similarity with previously published studies, as the non-infectious polymorphs of HET-s(218–289) do not exhibit the "cable-like" aggregates (Sabaté et al. 2007). However, we did not show *in vivo* infectivity in any of our studies, and as such, we will refer to our polymorphs by their molecular architecture or by their fibrillization conditions.

III.1.3 X-ray fiber diffraction data collection

X-ray fiber diffraction data were collected at three beamlines: the Biological Small-Angle X-ray Scattering beamline 4-2 at the Stanford Synchrotron Radiation Lightsource, and the BioCAT and BioCARS station C beamlines at the Advanced Photon Source in Argonne National Laboratory. Beamline 4-2 was set up with a vacuum tunnel which contained a diagonally mounted beamstop and a mica entry window, an X-ray wavelength of 1.078 Å, and a beam size of 100 × 100 µm. Diffraction patterns at beamline 4-2 were acquired on a Rayonix MX225-HE CCD detector (Rayonix, Evanston, IL) using 2 × 2 binning. The BioCAT beamline was setup with either vacuum or helium tunnels, both with beamstops mounted on the exit windows. Vacuum tunnels used beryllium entry windows, while helium tunnels used either aluminum or polymer-based entry windows. The X-ray wavelength used at BioCAT was 1.033 Å with a beam size of 60 × 60 µm. The detector used at BioCAT was a MAR-165 CCD detector (Marresearch, Norderstedt, Germany) modified with a thinned phosphor layer, using 2 × 2 binning. The BioCARS station C beamline used a vertically mounted beamstop with no beam tunnel, an X-ray wavelength of 0.9787 Å, and a beam size of 150 × 150 µm. The detector used was an ADSC Quantum-315 (Area Detector Systems Corporation, Poway, CA) using 2 × 2 binning. All data were collected at room temperature under controlled humidity conditions (McDonald et al. 2008).

III.1.4 Initial fiber diffraction patterns

Initial fiber diffraction specimens were produced as dried fibers (see Chapter II.2.2). The solutions were made by moving HET-s(218–289) fibrils into water with three rounds of ultracentrifugation at 265,000 × g and resuspension in water; final HET-s(218–289) concentrations were ~20 $\frac{\text{mg}}{\text{mL}}$. 5 µL droplets were suspended between small wax-tipped capillaries and dried at ~98 % RH against a saturated solution of K_2SO_4, and kept at constant humidity during data collection.

Fiber diffraction of HET-s(218–289) suspended in water yielded diffraction patterns with almost no orientation (Figure 17). Enough orientation is present to distinguish the 4.7 and 9.4 Å diffraction maxima as meridional reflections, indicating a repeating unit that

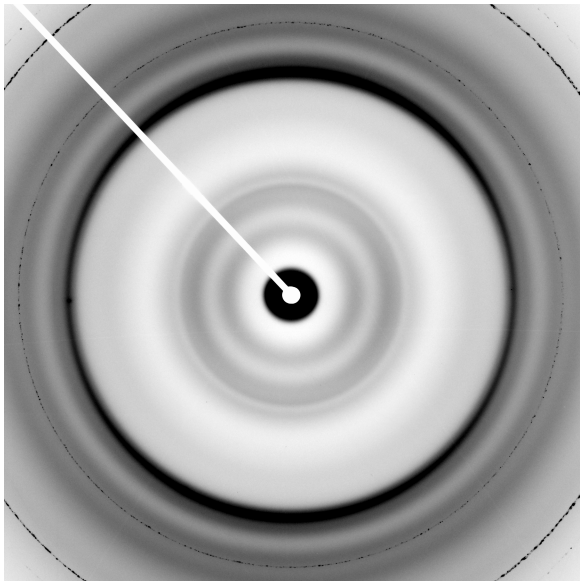

Figure 17: Initial X-ray fiber diffraction pattern of HET-s(218–289).

is two β-strands thick. Intense maxima at ~17 and 10 Å indicate that the structure of the repeating unit is more complex than that of a generic stacked β-sheet, which would dominated by a single equatorial maxima at ~8–10 Å. While these results are generally consistent with published two-rung β-solenoid structures of HET-s(218–289) (Wasmer et al. 2008a; Van Melckebeke et al. 2010), better oriented patterns were required for more precise analysis.

III.1.5 Improving specimen orientation

In order to obtain better oriented fiber diffraction patterns of HET-s(218–289), we set out to determine the conditions for optimal specimen preparation. While careful studies of specimen conditions and their impact on specimen orientations have been carried out for oriented sols (Gregory and Holmes 1965; Yamashita et al. 1991; Oda et al. 1998; Yamashita et al. 1998; Kendall and Stubbs 2006), no such examinations have been carried out for dried fiber specimens. However, basic principles from these methods should be generally applicable to all oriented fiber specimens. The overall goal in trying to orient a fibrous specimen is to get the individual fibrils within a solution to behave as rigid rods; oriented liquid crystalline phases will spontaneously form after a critical concentration is reached.

The rigidity of a rod is generally determined by the inherent flexibility caused by its structure as well as the length of the rod; fibrils above a critical length (the persistence length) no longer behave as rods. Amyloids are inherently very flexible, and it is difficult to obtain precise lengths. Many amyloids also form large aggregates which settle out of solution, so obtaining a true amyloid solution is often difficult.

The first step in obtaining well oriented HET-s(218–289) diffraction patterns was to produce HET-s solutions. The apparent problem was propensity of pH 7.5 HET-s(218–289) to form cable-like aggregates. It was previously noted that HET-s(218–289) cables could be reversibly dissociated by reducing the solution pH to 4 (Sabaté et al. 2007). The pH of pH 7.5 HET-s(218–289) fibrils was changed by pelleting and resuspension of fibrils in high molarity buffers and progressive lowering of molarity through repeated cycles of pelleting and resuspension. We found that with vigorous resuspension of fibrils, either by stirring or shearing through a 25 G needle, reducing the solution pH to 4 resulted in the formation of clear liquid-crystalline gels. After examining several buffers, including citric acid and phthalic acid, we found that 5 mM sodium acetate buffer and dilute hydrocholric acid at pH 4 were optimal. It was suggested that optimal pH for sols might be around the fibril isoelectric point (Yamashita et al. 1998), but pH 4 is significantly different from the isoelectric point of HET-s(218–289) (theoretical pI = 8.3). The ssNMR structure of HET-s(219–289) (Van Melckebeke et al. 2010) shows three solvent-exposed salt-bridges and the reduction of pH should give the fibril a net positive charge, which probably accounts for the reversible dissociation of the cable-like bundle morphology.

Several methods to control fibril length were attempted with mixed results. We found that fracturing fibrils after preparing gels through repeated freeze-thaw cycles or light sonication produced the best results. Other methods we experimented with included precipitation of fibrils and attemps to fractionate fibrils by length. Precipitation of fibrils using chemical additives was shown to be successful for determining fibril length in preparations of flagellin (Yamashita et al. 1998) and actin (Oda et al. 1998). Our method was to increase fibrillization rate using concentrated ammonium sulfate (0.5 M–3.0 M). While

fibrillization was more rapid, the fibrils solutions prepared by repeated pelleting and re-suspension did not produce improved orientation in dried fiber specimens. Fractionation of fibrils after freeze-thawing was attempted using centrifugation through sucrose step gradients or gel-filtration chromatography. For sucrose step-gradients, separations were seen in the different density layers, but removal of sucrose required additional pelleting which appeared to cause re-aggregation of fractured fibrils. Similar difficulties were seen with separations with gel-filtration chromatography; the dilute concentrations required to prevent column clogging resulted in the need to concentrate fibrils by lyophilization, apparently causing re-aggregation, and no substantial gain in orientation. The ease and improvement in orientation by freeze-thawing prior to use for dried fibers made it our general method. Freeze-thawing was performed by 5 cycles of rapid freezeing in liquid nitrogen followed by thawing in room-temperature water.

After fracturing, fibril gels required dilution before being used for dried fibers. This was because the fractured gels tended to still be in liquid-crystalline phases, as determined by birefringence under crossed polarizers. Enough buffer was added to remove birefringence; a 1:1 ratio of gel to buffer was usually sufficient. Dried fibers complete drying before fusion of individual domains can occur, so it is required to remove all domains before drying in order to prevent the formation of heterogeneously oriented fibers (Figure 12). Drying time and hydration were also increased by drying against water, at either room temperature or 4 °C. Since our freeze-thaw method produced random fracturing of fibrils, length distributions were also random, so the liquid crystalline properties were different for each preparation; finding particularly well oriented patterns requires many fibers from many preparations, even when the same protocols are used.

One of the best HET-s(218–289) diffraction patterns we have obtained has a disorientation angle of 13° (Figure 18). The improved orientation allows for clear separation of meridional, off-meridional, and equatorial intensities. While this pattern has very low disorientation for an amyloid pattern, we have had specimens with lower disorientations but much weaker signal owing to the particularly small diameter of the specimen that made it a weaker diffraction specimen as well as one that was much harder to align with the X-ray

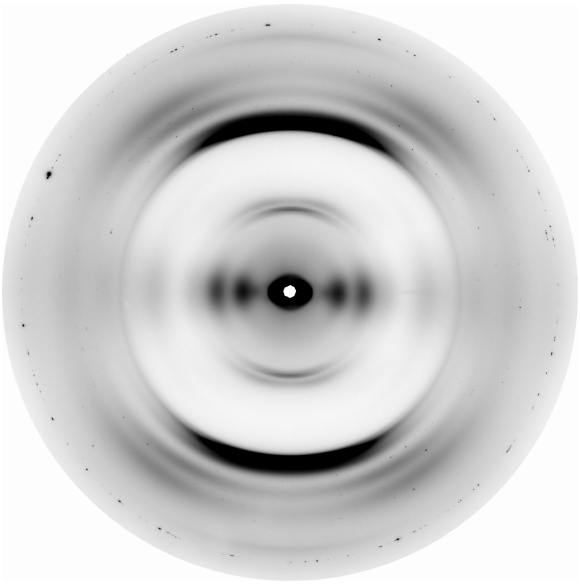

Figure 18: Well-oriented X-ray fiber diffraction pattern of HET-s(218–289).

beam. This pattern is considered among the best because of the good compromise between orientation and intensity.

III.2 Analysis of diffraction patterns

III.2.1 Initial analysis of diffraction patterns

Initial analysis of the well-oriented HET-s(218–289) diffraction pattern (Figure 18) showed diffraction that was consistent with a two-rung β-solenoid structure. Meridional reflections at ~9.4 Å, ~4.7 Å, and ~3.1 Å (Figure 19A) were consistent with the first, second, and third order meridional reflections expected from a two β-strand thick structure. The off-meridional intensity maximum at $d^* = 4.0$ Å falls on the 4.7 Å layer line (Figure 19B), indicating that it is a subsidiary maximum of this layer line. Off-meridional intensities at $d^* = 8.5$ Å and $d^* = 3.6$ Å do not fall on the 9.4 Å (Figure 19C)or 4.7 Å (Figure 19B)layer lines, indicating that these maxima are from non-zero order Bessel functions. The separation of these Bessel functions on the Z-axis indicates the presence of helical twist within the fibril. The series of diffraction maxima on the equator (Figure 18) is indicative of a cylindrical core. That equators have no single dominant intensity maximum, but instead have

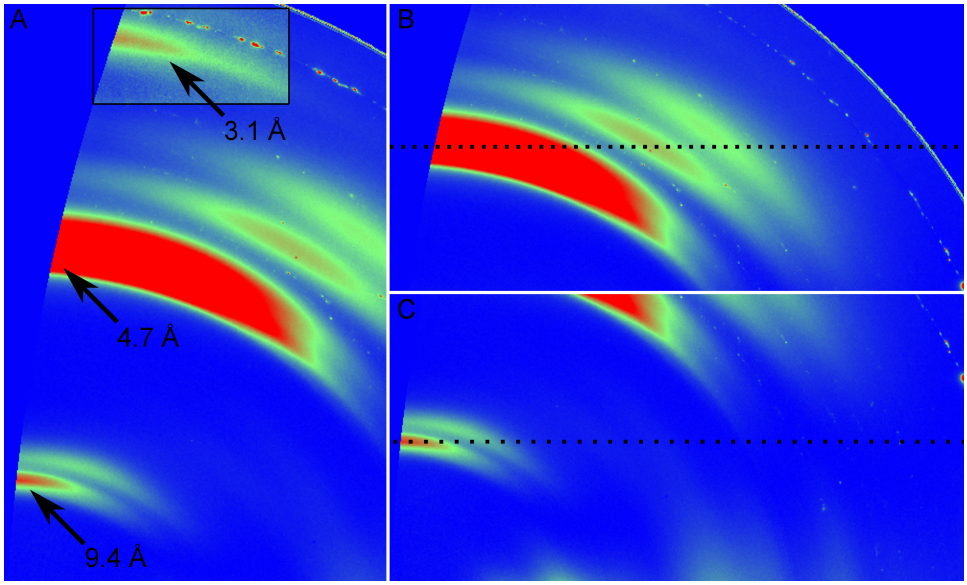

Figure 19: pH 7.5 HET-s(218–289) meridional and off-meridional diffraction. Panels are from the diffraction pattern in Figure 18 after transformation into reciprocal space and background subtraction. A) Meridional reflections. Inset intensities adjusted to show 3.1 Å reflection. B) 4.7 Å and C) 9.4 Å layer lines. Layer line positions are shown as dotted lines.

a series of maxima, indicates that the cross-sectional structure does not have a particularly strongly represented periodicity.

III.2.2 Calculated diffraction from the ssNMR model

In order to compare our diffraction patterns with the published HET-s(218–289) ssNMR structure, we calculated diffraction patterns from the model. The ssNMR PDB (protein data bank) file consisted of an ensemble of the 20 lowest energy models, each consisting of three Met-HET-s(218–289)-His6 subunits. For our initial model, we used the middle subunit of the lowest energy model, and prepared it by aligning the rungs of the β-solenoid parallel to the xy-plane and placing the center of mass at the z-axis, which also serves as the fiber axis (Figure 20A). Calculated patterns were produced using DISORDER, a program that calculates diffraction using Fourier-Bessel methods (Cochran et al. 1952; Klug et al. 1958) and disorientation using a three-dimensional approach (Holmes and Barrington Leigh 1974). Helical parameters used were $p = 9.48$ Å and 60 subunits per turn. Temperature factors (Table 1)used were chosen to reflect the relative flexibilities of the structural features

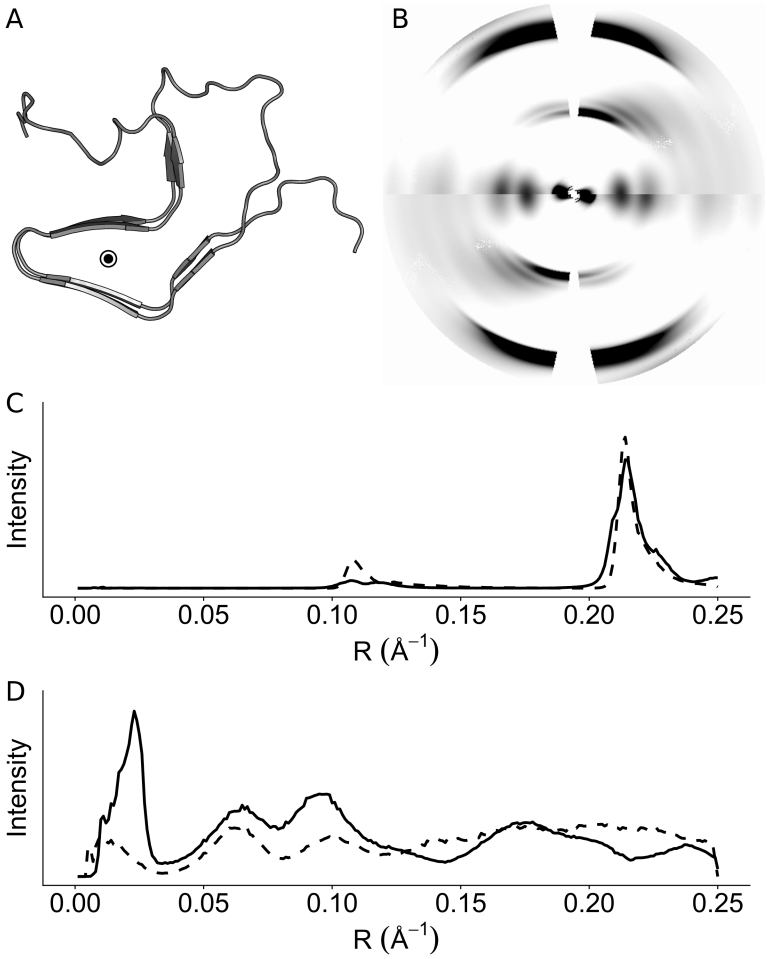

Figure 20: Initial comparions of experimental and calculated HET-s(218–289) diffraction. A) ssNMR model of HET-s(218–289). Circle indicates fiber axis. B) Comparison of calculated and experimental fiber diffraction patterns. Upper-right and lower-left are calculated while lower-right and upper-left are experimental. Sector plots of C) meridional and D) equatorial data. Meridional intensity scale is 10 times that of the equatorial intensity scale. Solid line: experimental data. Dotted line: calculated data.

Table 1: Temperature factors used for simulated diffraction of β-solenoid HET-s(218–289)

Structure type	Start residue	End residue	Temperature factor
N-terminus	217	222	1000
β-1a	223	228	10
K229	229	229	10
β-1b	230	234	10
Turn	235	236	10
β-2a	237	241	10
G242	242	242	10
β-2b	243	249	30
Loop	250	259	1000
β-3b	260	264	10
E265	265	265	10
β-3a	266	270	10
Turn	271	272	10
β-4a	273	277	10
G278	278	278	10
β-4b	279	281	30
C-terminal loop	282	285	100
Hydrophobic patch	286	287	100
C-terminus	288	289	1000
6×His-tag	290	295	1000

as indicated by ssNMR (Wasmer et al. 2008a; Van Melckebeke et al. 2010). Scaling between experimental and calculated data were performed using a single scale factor determined by least-squares fitting of equatorial data from 0.03–0.25 $Å^{-1}$ (~33–4 Å). Lower resolution data was not used because of possible errors in intensity caused by beam divergence, and an inability to accurately determine solvent-contrast.

Overall, the experimental and calculated diffraction pattens appeared to give a good qualitative fit (Figure 20B), though there were clear differences on the meridian. The meridional reflections were in the correct positions, as these were parameters put into the calculation, but off-meridional positions were a bit off, indicating disagreement in the high-resolution structures (Figure 20B, C). The most significant difference was the relative intensities between the 4.7 Å and the 9.4 Å reflections (Figure 20C), with the calculated pattern having a very intense 9.4 Å reflection. This may have been caused by some type of disorder within the subunit that we are unable to accurately model. Equatorial data showed

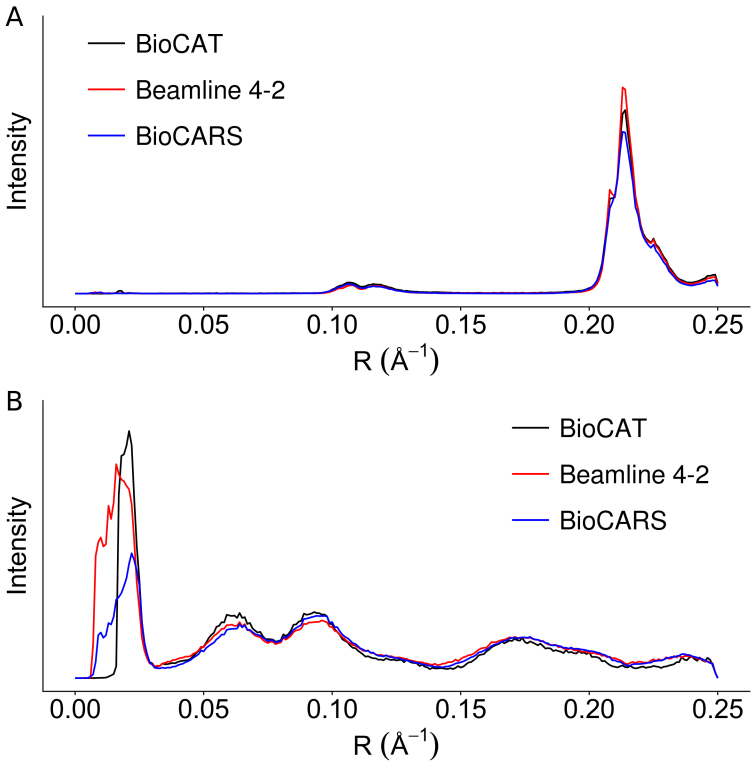

Figure 21: Diffraction of HET-s(218–289) from different specimens at various beamlines. A) Meridional and B) equatorial sector plots.

a good qualitative fit, in that the maxima positions were roughly in the correct places. One major difference is in the intense low-resolution maxima at ~45 Å, which isn't seen in the calculated pattern. This may be caused by poor modelling of solvent-contrast in the calculated pattern, resulting in low calculated intensity, but is also possibly caused by some level of paracrystallinity in the specimen. It is likely solvent-contrast combined with some paracrystalline effect increasing the intensity, but the maximum position is relatively constant between different HET-s(218–289) specimens at different beamlines (Figure 21). While medium to high resolution (0.3–0.25 Å, ~33–4 Å^{-1}) equatorial diffraction have similar diffraction maxima and relative intensities, the CC calculated for this resolution range is only 0.24; a good CC is generally taken as 0.80 or higher (Gonzalez et al. 1995). The poor CC is unlikely to be caused by scaling issues; CCs are generally unaffected by scaling the same way R-factors are. CCs are mean-adjusted making them primarily a measure of the

covariance of each function with respect to the mean, essentially providing a comparison of intensity maxima positions. Scaling only becomes an issue in the presence of a very large maxima; large maxima can throw off the mean, making the CC insensitive to the variations of lower intensity maxima. CCs between the diffraction patterns in Figure 21 are between 0.96 and 0.98. Another source of disagreement between experimental and calculated patterns could be errors in temperature factors, as this may manifest as a resolution-dependent scaling error; non-linear scaling errors may effect CCs.

To try and improve the fit between the calculated diffraction from the ssNMR model and our experimental diffraction patterns, we used a grid-search approach to modify the orientation of the subunit. Our search approach is similar to one used to obtain models of F-actin (Holmes et al. 1990). The grid-search was performed by first iterating rough translations alternating with rough rotation steps (± 2 or 4 degrees or Å) until improvements in the CCs between equatorial traces of the calculated and experimental patterns settled within the edges of the search. Equatorial traces were used rather than sector plots because of output limitations of DISORDER; equatorial plots under-represent intensities with respect to increasing resolutions, owing to the angular spread of intensities caused by disorientation. However, this may not be a significant limitation as a rigid-body search will mostly be useful for refining low-resolution features; high-resolution features cannot be refined by such an approach. Following the rough search, fine searches (± 0.5 or 1.0 degrees or Å steps) were performed until CCs converged. In total, 8 iterations were performed (Figure 22).

The grid-search shifted the fiber axis (Figures 20A, 23A) and produced a calculated diffraction pattern with a better overall match to the experimental pattern (Figure 23B). Interestingly, the relative intensity of the meridional reflections with respect to the equator has increased after the grid-search (Figures 20C, D, 23C, D). This may be caused by the shift in the fiber axis position (Figures 20A, 23A) which effectively increases the diameter of the fibril without adding mass; the electron density of the cross section becomes reduced with respect to the electron density parallel to the fiber axis. Despite improvements to the qualitative fit, the medium to high resolution (0.3–0.25 $Å^{-1}$, ~33–4 Å) CC is still only 0.33.

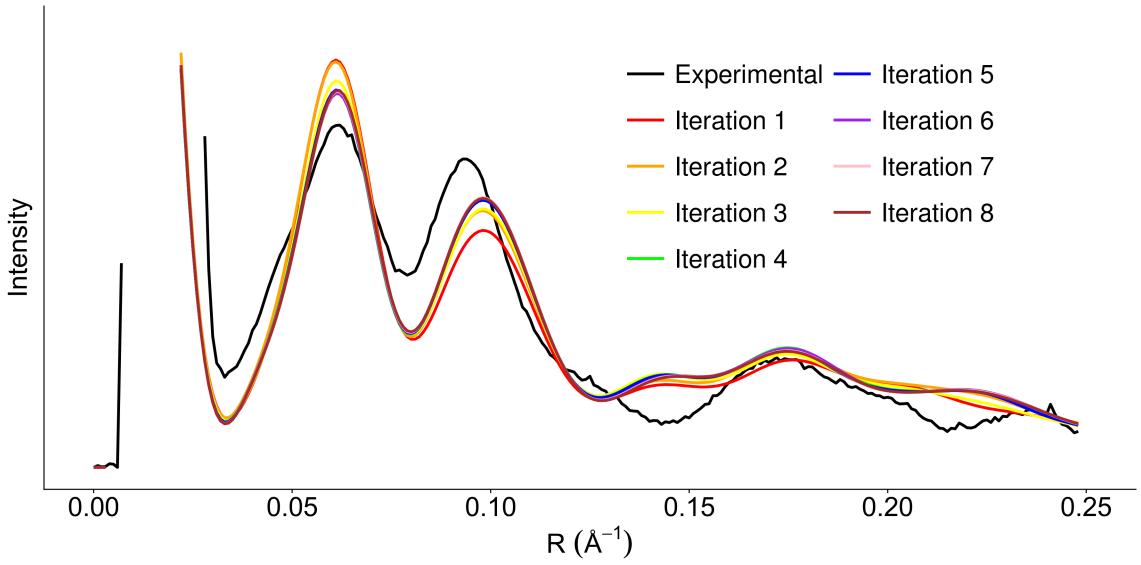

Figure 22: Equatorial traces of grid-search iterations.

To visualize the difference in CC with respect to resolution, we plotted CCs between the initial or grid-searched equators and the experimental equator with respect to resolution range (Figure 24). The effect of the grid search changes the CC profile slightly and generally increases the CC across the whole range. The CC for the initial model drops below 0.80 at 0.13Å^{-1} (~7.69 Å), while the grid-searched model extends this to 0.137Å^{-1} (~7.30 Å). This resolution can define the overall triangular shape of the β-solenoid core and is of similar resolution to those of cryo-electron microscopy (cryo-EM) reconstructions of HET-s(218–289) fibrils formed at acid pH values (~6.4 Å) (Mizuno et al. 2011). We have confirmed that the HET-s(218–289) diffraction patterns we have obtained have the same β-solenoid structure as the published model by ssNMR in collaboration with the Wemmer laboratory at the University of California at Berkeley (Wan et al. 2013). The disagreement between diffraction patterns calculated from the ssNMR model and our experimental diffraction patterns may be caused by several factors. The ssNMR model represents a dynamic ensemble structure and a single subunit may not accurately represent the static averaged structure observed by X-ray diffraction. An additional problem is that the ssNMR model is not defined with respect to the fiber axis the way fiber diffraction is; when this is also taken with the fact

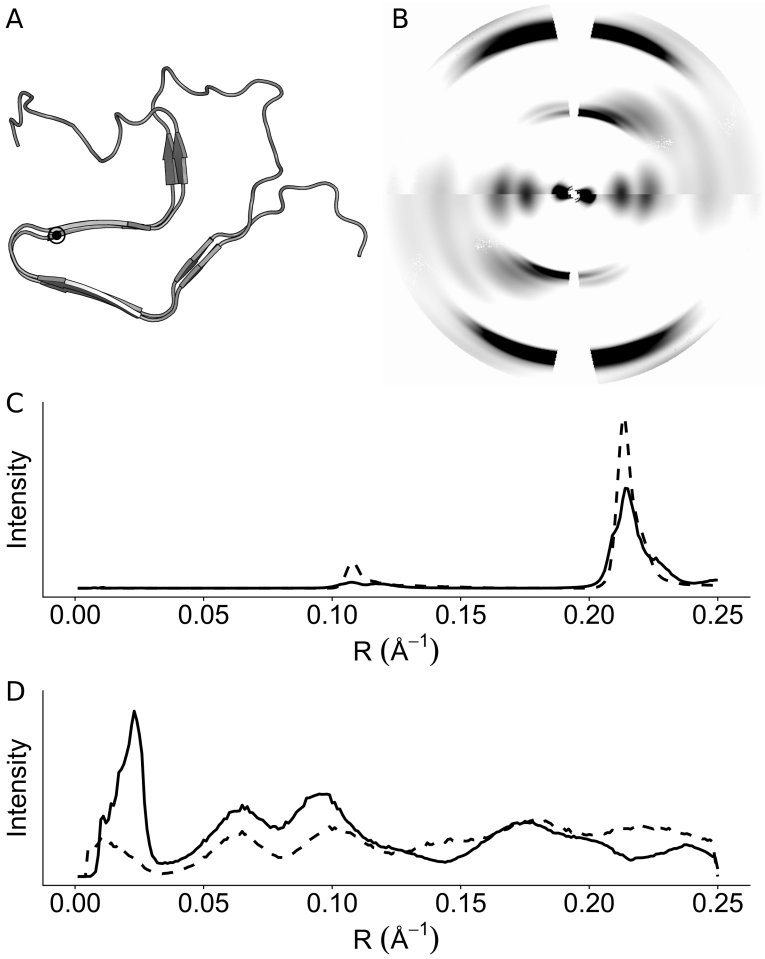

Figure 23: Experimental and calculated HET-s(218–289) diffraction after an iterative grid-search. A) ssNMR model of HET-s(218–289). Circle indicates fiber axis. B) Comparison of calculated and experimental fiber diffraction patterns. Upper-right and lower-left are calculated while lower-right and upper-left are experimental. Sector plots of C) meridional and D) equatorial data. Meridional intensity scale is 10 times that of the equatorial intensity scale. Solid lines: experimental data. Dotted lines: calculated data.

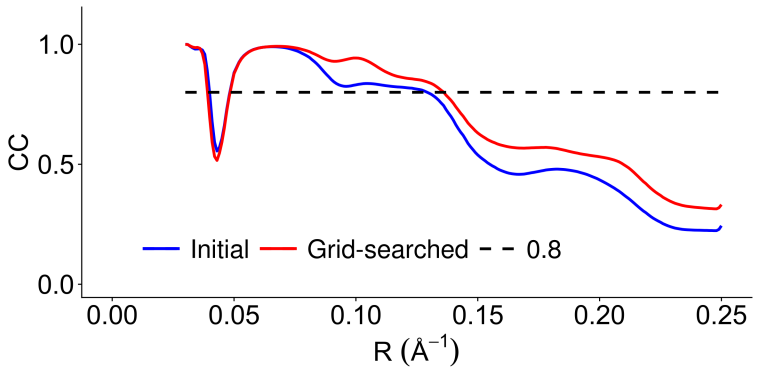

Figure 24: Cumulative CC between calculated and experimental equators. The lower end of the resolution range is 0.03Å^{-1} (~33 Å).

that the ssNMR model was produced using three subunits rather than a simulated infinte fibril, the long range interactions may not have been accurately reproduced. The direct subunit stacking of amyloids may make long-range interactions important for defining the positions of atoms with respect to the fiber axis. Since ssNMR data is inherently short-range, ssNMR models of amyloids seem to accurately define subunit structures but cannot accurately reproduce fibril structure.

III.2.3 Determining the pitch of HET-s(218–289)

In order to directly determine the pitch of HET-s(218–289), we attempted to measure the separation between the J_0 and J_1 Bessel functions along the Z axis, that is, $\frac{1}{p}$. The instrumentation required for measuring this type of diffraction includes a long diffraction camera in order to increase the spatial resolution of the detector, virtually no beam divergence in order to accurately measure diffraction close to the beam stop, and a setup with minimal background scatter because the intensity at each pixel of the detector is decreased by a factor related to the square of the increase in spatial resolution. In order to be able to separate individual Bessel functions, very well oriented, strongly diffracting specimens are required. We performed our diffraction experiments at the BioCAT beamline using a specimen to detector distance of ~990 mm.

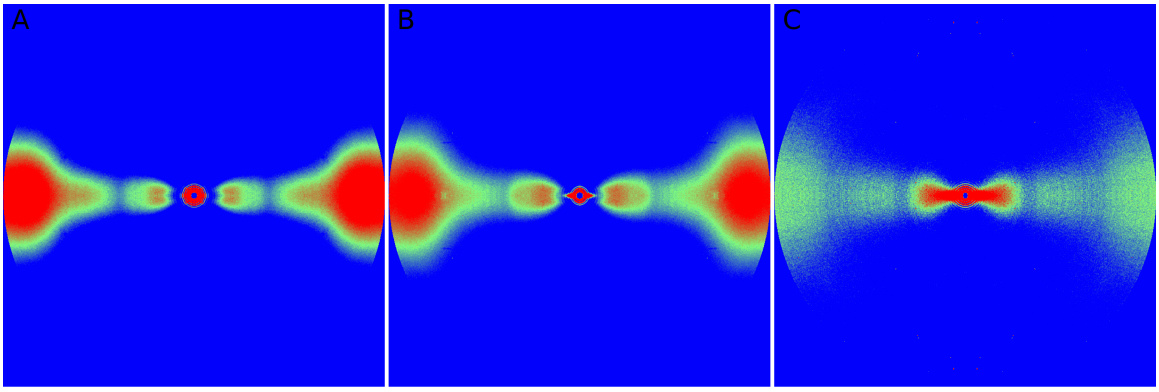

Figure 25: Low-angle fiber diffraction of HET-s(218–289). A) Well oriented showing clear separation of the J_1 maxima. B) Poorly oriented, and C) weakly diffracting specimens.

While we were able to obtain diffraction patterns oriented enough to clearly distinguish the J_1 maxima (Figure 25A), most diffraction patterns were either not well oriented enough (Figure 25B), or too weak to measure anything (Figure 25C) The pitch of HET-s(218–289) measured from Figure 25A was 625 Å (0.0016 $Å^{-1}$), though at the current spatial resolution (0.0002 $Å^{-1}$ per pixel), a one pixel error would put the range of the pitch from 714–556 Å. Better precision would require an even longer diffraction camera, which may not be feasible owing to the already weak diffraction. Diffraction patterns with measurable pitch were only obtained from certain domains within a single dried fiber. From these results, it is difficult to conclude if HET-s(218–289) actually has a reproducible pitch. Variable pitch should theoretically produce discernable differences in the convoluted wide-angle patterns, but we find that wide-angle diffraction is very reproducible (Figure 21). That it is possible to obtain a pitch measurement at all indicates a fairly high level of order, as a pattern that can provide such a measurement requires a substantial number of fibrils with the same pitch. However, without reproducible pitch measurements from different preparations and specimens, we cannot conclude that this pitch is a true structural constant.

III.3 The effect of hydration on HET-s(218–289) molecular structure

Previous research on the effects of hydration on amyloid structure have yielded differing results. Studies on stacked β-sheet amyloids have suggested that dehydration does

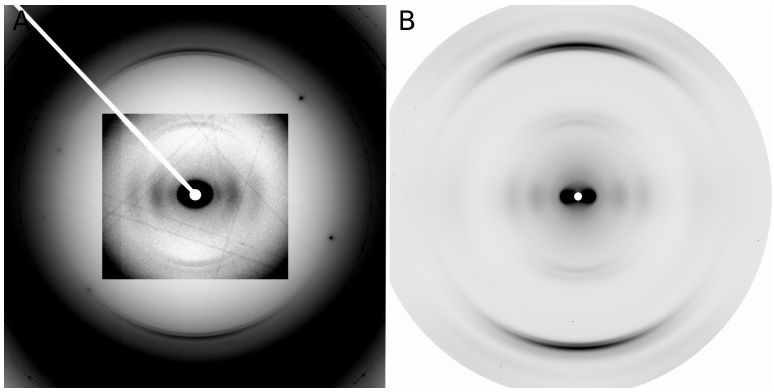

Figure 26: Comparison of HET-s(218–289) oriented sols and dried fibers. A) Oriented sol and B) dried fiber diffraction patterns. Inset in A) had adjusted intensities to show low-angle diffraction data.

not impact fibril structure (Squires et al. 2006; Maurstad et al. 2009; Morris et al. 2013), while studies on the yeast prion-forming domain Sup35 NM (Kishimoto et al. 2004) showed dehydration-related changes in the diffraction pattern, leading to the suggestion that Sup35 NM forms a water-filled nanotube, similar to those suggest for the Huntington's disease-related poly-glutamine amyloid (Perutz et al. 2002). Recent models of the Alzheimer's disease related Aβ1–40 have included central water-accessible channels, indicating that water structure may play an important role in the overall amyloid structure (Miller et al. 2011; McDonald et al. 2012; Lu et al. 2013). Studies on HET-s(218–289) have shown that the hydrophobic core is not solvent-accessible (Van Melckebeke et al. 2011). We have investigated the structural impact of hydration on HET-s(218–289) by comparing X-ray fiber diffraction patterns under various humidity conditions.

III.3.1 Comparison of HET-s(218–289) sols and dried fibers

For specimens with complete hydration, HET-s(218–289) sols were made; sols are specimens consisting of gels in sealed capillaries, thus ensuring complete hydration. Sols were made from freeze-thawed liquid-crystalline pellets by flow-alignment in glass X-ray capillaries with 0.3 mm inner diameters. This method was not used as a general method for X-ray diffraction as HET-s(218–289) showed poor flow-alignment properties (Figure 10) and gave very weak X-ray diffraction patterns (Figure 26A). The protein diffraction from

oriented sols is weak owing to the large amount of water present, which can be seen as a large dark ring along the pattern edge at ~3.5 Å resolution (~0.3 $Å^{-1}$). The water diffraction is so overwhelming that the low resolution diffraction below 10 Å is not visible without saturating the rest of the pattern (Figure 26A). This weak protein diffraction precluded quantitative analysis as accurate background subtraction and integration of intensities was not possible. However, qualitative examination of intensity maxima locations and relative intensities with a dried fiber specimen stored at nominal 100 % RH (Figure 26B) indicated that the structures were similar, consistent with previous comparions of Sup35 NM sols and fibers (McDonald et al. 2008; Kishimoto et al. 2004).

III.3.2 Fiber diffraction of HET-s(218–289) at various relative humidities.

To determine the impact of dehydration on HET-s(218–289) structure, we collected diffraction data from specimens first dried at nominal 100 % RH, and further dried to 0 %, 33 %, 75 %, 83 %, and 98 % RH (Figure 27A–F). To assess the reversibility of dehydration, the 0 % RH specimen was rehydrated at nominal 100 % RH, and diffraction data were collected (Figure 27G). For easier comparison, meridional and equatorial intensities were integrated and plotted, and scaling was performed by least-squares fitting between ~30 and 4 Å (~0.03–0.25 $Å^{-1}$) resolution (Figure 27H, I). Dehydration did not affect the projection of the structure on the fiber axis, since meridional relative intensities remained consistent. Meridional diffraction spacings were also not perturbed, indicating that the helical parameters of the fibrils were unchanged. Diffraction along the equator, however, showed substantial decreases in low resolution intensity on dehydration. By 83 % RH, there was virtually complete loss of ~50 Å and ~17 Å maxima. While very low resolution diffraction such as the ~50 Å maximum can sometimes be related to inter-fibril packing within a specimen, this is unlikely to be the case in HET-s(218–289), as we have consistently observed this intensity maximum in diffraction from many different preparations and specimens (Figure 21). The loss of low resolution diffraction maxima and the relative strengthening of the ~11 Å (0.09 $Å^{-1}$) maximum indicates a collapse of the triangular hydrophobic core of HET-s(218–289)

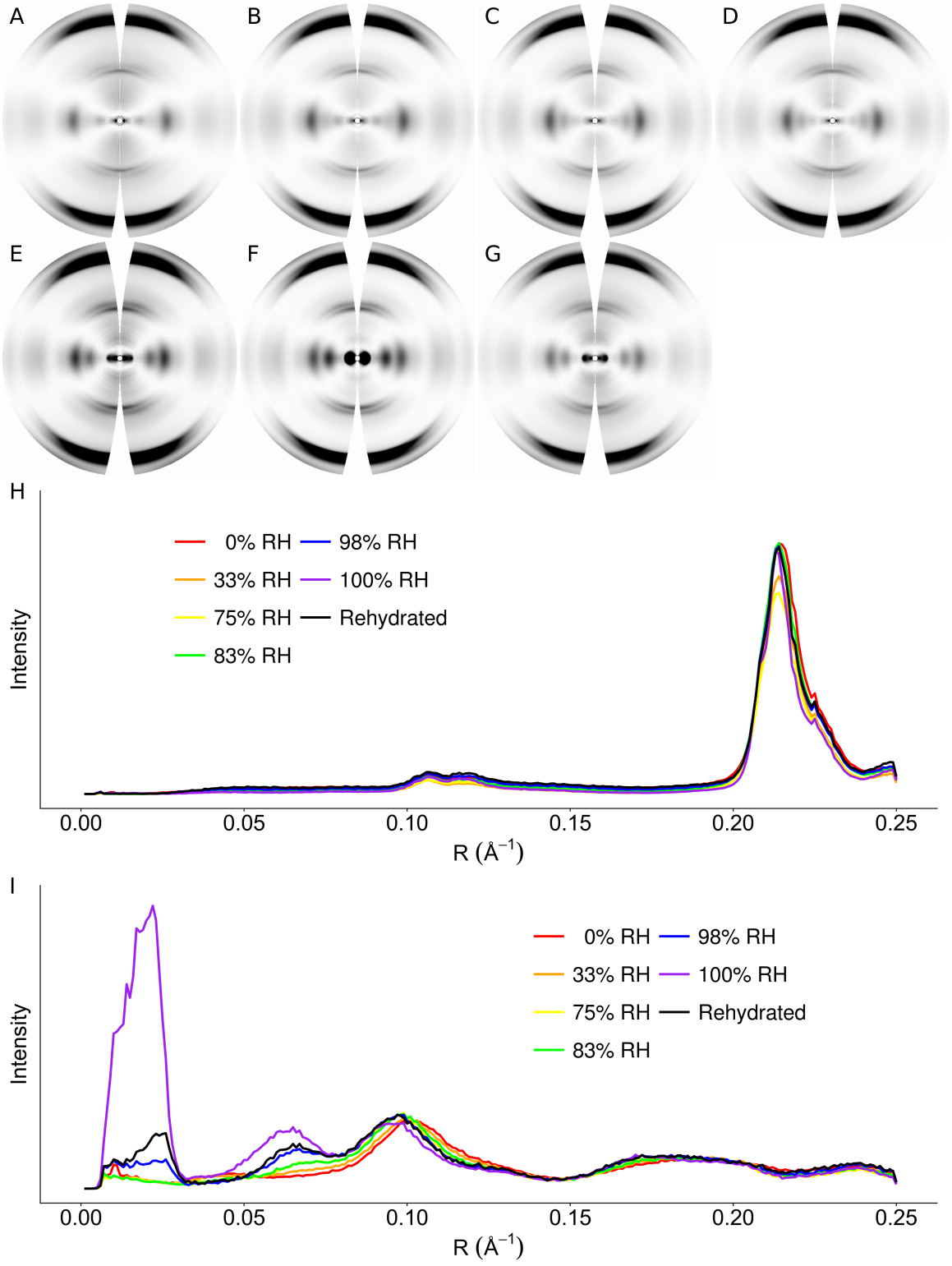

Figure 27: Fiber diffraction of HET-s(218–289) at different relative humidities. Background-subtracted diffraction patterns of (A) 0 % RH, (B) 33 % RH, (C) 75 % RH, (D) 83 % RH, (E) 98 % RH, (F) 100 % RH, (G) 0 % RH rehydrated to nominal 100 % RH. Plots of (H) meridians and (I) equators. Relative intensities are 5x stronger in (H) than (I).

Table 2: Correlation coefficients from ~30–4 Å resolution (~0.03–0.25 $Å^{-1}$) of HET-s(218–289) at various humidities.

Sample	0 % RH	33 % RH	75 % RH	83 % RH	98 % RH	100 % RH	Rehydrated
0 % RH	1.00	0.98	0.90	0.92	0.80	0.52	0.76
33 % RH		1.00	0.97	0.98	0.89	0.65	0.86
75 % RH			1.00	1.00	0.97	0.78	0.95
83 % RH				1.00	0.96	0.76	0.94
98 % RH					1.00	0.87	0.99
100 % RH						1.00	0.90
Rehydrated							1.00

into a more parallel arrangement, resembling a stacked β-sheet. Rehydration of the desiccated specimen resulted in incomplete recovery of low resolution diffraction maxima, with an equatorial plot closely resembling the 98 % RH plot.

To quantitate the level of structural distortion caused by dehydration, CCs were calculated between the equatorial data from each pair of specimens in two different resolution ranges. In the intermediate resolution range (~30–4 Å, ~0.03–0.25 $Å^{-1}$) meaningful correlation (CC > 0.8) with the 100 % RH specimen was lost by 83 % RH (Table 2). Quantitative comparisons across the full resolution range are not as useful as the intermediate resolutions, owing to the high sensitivity to dehydration of the ~50 Å intensity maximum. Perturbation of the ~50 Å intensity maximum maybe caused by solvent-contrast or paracrystalline effects. CCs also showed that the rehydrated specimen correlated more closely with the 98 % RH specimen than with the nominal 100 Å RH specimen.

The dehydration of amyloid fibrils with complex structures can significantly perturb their molecular structures. While this had been suggested for the special case of Sup35 NM (Kishimoto et al. 2004), our results with HET-s(218–289) show that dehydration effects can occur even in the absence of water-accessible channels. This observation indicates that for complex amyloid structures, ordered water on the surface of the fibril can play a substantial role in its molecular structure. This apparently does not affect stacked β-sheet amyloids in the same way (Squires et al. 2006; Maurstad et al. 2009; Morris et al. 2013), possibly because the crystalline nature of the β-sheet packing provides structural stability

against deformation caused by dehydration. Dehydration studies must be performed on each amyloid system to safely assume that dehydrated fibrils truly reflect the biologically active amyloid. Our results show that water can play an important role in amyloid structure even when no obvious water-accessible internal features are present, emphasizing the importance of surface solvent.

CHAPTER IV

Biophysical characterization of polymorphic HET-s(218–289) structures

IV.1 Characterization of proteolyzed HET-s(218–289) amyloid

IV.1.1 Initial structural characterization of polymorphic HET-s(218–289) amyloid

Our initial experiments with HET-s(218–289) fibrillized under acidic conditions used the conditions described for forming non-infectious HET-s(218–289) amyloid (Sabaté et al. 2007). The overall expression and purification protocol was as described in Chapter III.1.1, except that purified monomer solution in 6 M Gdn-HCl was desalted into 40 mM boric acid, 10 mM citric acid, 7 mM NaCl, pH 2.0. Desalted monomer solutions were allowed to fibrillize at room temperature. Negative stain EM and X-ray fiber diffraction were carried out as previously described (Chapter III.1.2–3).

HET-s(218–289) formed at pH 2.0 shows different morphologies and fiber diffraction patterns depending on incubation time. The β-solenoid form of HET-s(218–289) fibrillizes immediately upon bringing the pH of the monomer solution to 7.5, and the resultant fibrils have the characteristic cable-like morphology (Figure 28A) and two-rung β-solenoid diffraction pattern (Figure 28D), as previously described (Chapter III). HET-s(218–289) fibrillized at pH 2.0 tended to form fibrils more slowly, sometimes requiring several months before solutions became turbid. EM from pH 2.0 HET-s(218–289) fibrils after 3 months showed a more disperse and slightly twisted morphology (Figure 28B), distinct from the cable-like aggregates of pH 7.5 HET-s(218–289) (Figure 28A). However, fiber diffraction patterns of pH 2.0 HET-s(218–289) (Figure 28E) showed diffraction patterns that were remarkably similar to the two-rung β-solenoid patterns (Figure 28D). The meridional spacings between diffraction patterns from the two fibril types matched up well and the medium resolution (0.03–0.20 $Å^{-1}$, ~33–5 Å) equatorial CC was 0.94.

After prolonged incubation, pH 2.0 HET-s(218–289) fibrils took on different morphologies and gave different fiber diffraction patterns. The morphology of fibrils incubated at pH

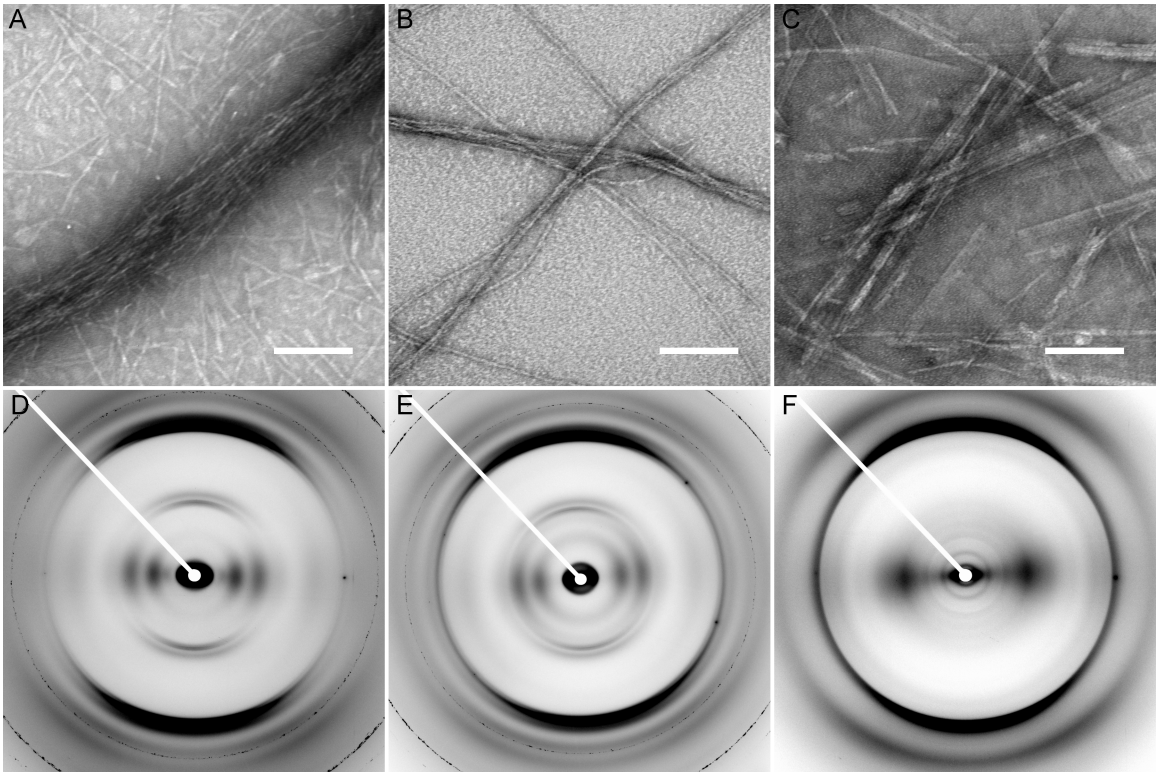

Figure 28: Negative stain EM and fiber diffraction of HET-s(218–289) polymorphs. Electron micrographs are on the top row and fiber diffraction patterns on the bottom row. HET-s(218–289) was formed at A) and C) pH 7.5, B) and E) pH 2.0 at 3 months, and C) and F) pH 2.0 at over 12 months. Scale bar = 100 nm

2.0 for over 12 months were more rigid and sheet-like (Figure 28C), distinct from the more flexible twisted fibrils seen with less aged samples (Figure 28B). The fiber diffraction pattern from these aged pH 2.0 HET-s(218–289) fibrils (Figure 28F) was substantially different from the two-rung β-solenoid pattern (28D, E), with an equatorial CC of only 0.22. While the ~4.7 Å meridional reflection still demonstrates the presence of cross-β structure, there is no longer a ~9.4 Å layer line, indicating that the two-rung structure is not present. The equatorial reflections have also changed significantly, and are now dominated by a strong ~11 Å reflection.

The combination of a 4.7 Å meridional reflection and a strong equatorial intensity maximum near 10 Å was first observed by Astbury (1935), and has long been widely recognized as the distinctive signature of stacked β-sheet structure (Rudall 1946; Eanes and Glenner 1968; Geddes et al. 1968; Bonar et al. 1969; Sunde et al. 1997; Kishimoto et al. 2004; Nelson et al. 2005; Sawaya et al. 2007; Jahn et al. 2010). As with all cross-β structures, the ~4.7 Å meridional reflection corresponds to the distance between β-strands within a sheet (Figure 29), which is sometimes called the inter-strand spacing. The equatorial intensity maximum at ~10 Å is generally called the inter-sheet spacing (Figure 29), referring to the distance between adjacent stacked β-sheets, and its precise spacing depends on the side-chains in the interfaces between adjacent sheets. The complete lack of a ~9.4 Å meridional reflection even in patterns from the exceptionally high quality beamlines used (Tsuruta and Irving 2008), indicates that the β-sheets are parallel, not anti-parallel. The strong isolated equatorial ~11 Å intensity indicates that the sheets are stacked and not solenoidal; the distinction has been noted for the yeast prion protein Sup35 NM (McDonald et al. 2008; Kishimoto et al. 2004), and the differences are illustrated in the extensive simulations described elsewhere (Wille et al. 2009); in no case did a solenoidal structure give rise to a pattern resembling the stacked β-sheet pattern.

IV.1.2 HET-s(218–289) proteolyzes during prolonged incubation

SDS-PAGE analysis of HET-s(218–289) solutions and re-dissolved fiber diffraction samples (Figure 30) showed that although newly-purified pH 7.5 HET-s(218–289) fibrils were

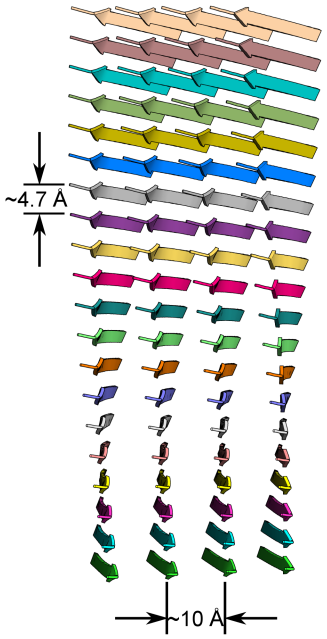

Figure 29: Model of a generic stacked β-sheet. The ~4.7 Å measurement corresponds to the inter-strand spacing while the ~10 Å measurement corresponds to the inter-sheet spacing.

composed of homogeneous full-length peptide (Figure 30A), all of the low pH fibrils that exhibited stacked β-sheet-like diffraction were extensively proteolyzed, forming several well-defined molecular species (Figure 30B). Tryptic digests were performed on the degraded protein bands and tandem mass spectrometry (MS/MS) was used to analyze the composition of the resulting peptides (Figure 30D). There was no coverage between residues Asn266 and Arg238 owing to the large number of tryptic proteolytic sites in this area. Nevertheless, the presence of the first peptide and otherwise complete coverage to the 6×His-tag from band 1 showed that this was the complete recombinant protein. Band 2 did not contain the first tryptic peptide, indicating N-terminal proteolysis into the uncovered region, most probably including strand β1-a. Band 3 contained a unique tryptic peptide showing proteolysis up to Gly242 and the loss of the first rung of the β-solenoid core. Band 4 contained the first and second tryptic peptides but was missing the last three tryptic peptides, indicating proteolysis from the C-terminus, including the loss of the second rung of the β-solenoid core.

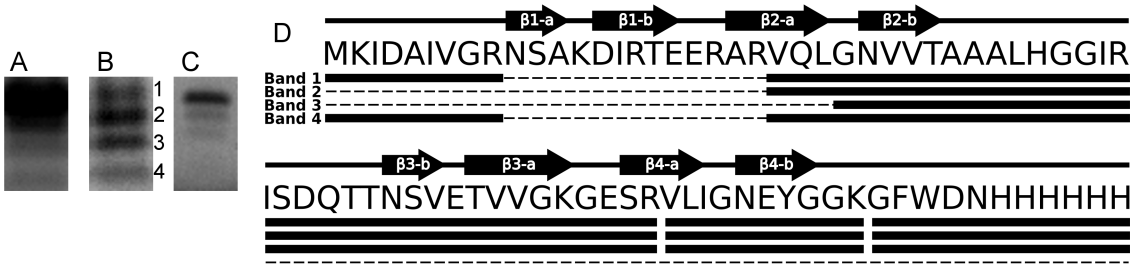

Figure 30: SDS-PAGE and mass spectrometry analysis of HET-s(218–289) fibril preparations. A) SDS-PAGE after pH 7.5 fibrillization. B) SDS-PAGE after pH 2.0 fibrillization over 12 months. Numbers indicate the bands analyzed by MS/MS. C) SDS-PAGE after seeded pH 2.0 fibrillization. D) Secondary structure from ssNMR structure (Wasmer et al. 2008a; Van Melckebeke et al. 2010), amino acid sequence, and peptides found by MS/MS analysis. Black arrows: β-strands. Solid lines connecting arrows: loops or disordered regions. Heavy solid lines below the sequence correspond to tryptic peptides from SDS-PAGE bands in B). Dashed lines denote regions that did not appear in MS analysis.

With these significant losses of secondary structure, it is not surprising that these molecular species do not form solenoids, but instead polymerize into simple stacked β-sheets.

IV.1.3 Seeding stacked β-sheets with degraded fibrils

Fibrils were also made at pH 2.0 by seeding freshly-prepared HET-s(218–289) solutions with degraded fibrils that had been formed at low pH. Seeded fibrils formed orders of magnitude more rapidly than unseeded fibrils under comparable conditions, requiring times from minutes to two or three days, in contrast to unseeded fibrils, which required from a few days to several months to form. The seeded fibrils exhibited heterogeneous, flexible morphology (Figure 31A) distinct from that of proteolyzed fibrils (Figure 28C), and stacked β-sheet diffraction (Figure 31B), but showed little proteolysis in SDS-PAGE (Figure 30C). Densitometry of the seeded fibril gel shown in Figure 30C, which was from a re-dissolved fiber used for diffraction, indicated that intact protein made up about 80 % of the diffracting sample, but the diffraction pattern showed no evidence of solenoid structure. We conclude that stacked β-sheets formed from the degraded protein were able to act as templates for undegraded protein, even though we did not at any time observe spontaneous formation of stacked β-sheets by undegraded protein.

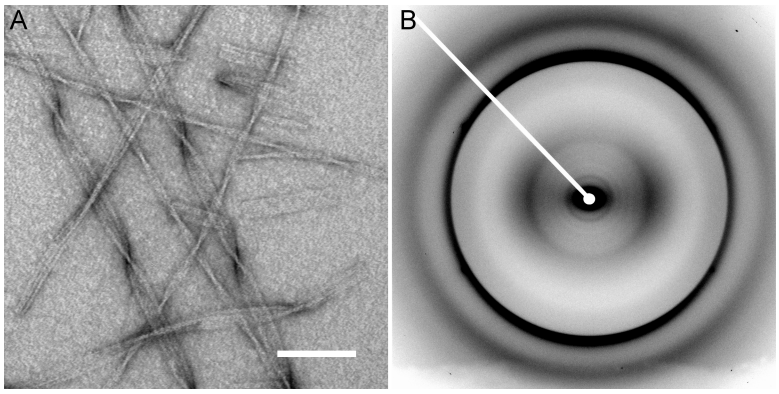

Figure 31: Negative stain EM and fiber diffraction of pH 2.0 HET-s(218–289) seeded with degraded fibrils. A) EM and B) fiber diffraction pattern.

IV.1.4 Characterizing HET-s(218–289) preparations with thioflavin-T

Thioflavin T (ThT) is a dye that exhibits strong fluorescence after binding certain types of amyloid (Nilsson 2004). In the case of HET-s(218–289) it has been shown that the infectious β-solenoid fibrils do not induce fluorescence in bound ThT while non-infectious HET-s(218–289) does (Sabaté et al. 2007). In order to determine if our fibrils reproduced similar fluorescence inducing properties, we conducted ThT fluorescence experiments. Specimens consisted of solutions containing 10 µM HET-s(218–289) fibrils and 25 µM ThT in Tris-buffered saline pH 7.5. Fluorescence measurements were performed using an excitation wavelength of 450 nm and recorded over the emission range of 470–570 nm. Measurements were performed either with quartz cuvettes in a Horiba Jobin Yvon Fluoromax-3, or in black non-binding 96-well plates (Greiner Bio-One, Frickenhausen, Germany) using a PerkinElmer EnSpire (PerkinElmer, Waltham, MA).

ThT fluorescence induced by binding to the various HET-s(218–289) fibrils (Figure 32) matched the structural differences observed by fiber diffraction. The β-solenoid structure of the pH 7.5 fibrils induced minimal ThT fluorescence, while samples composed primarily of stacked β-sheet fibrils (degraded pH 2.0 fibrils and seeded freshly-prepared pH 2.0 fibrils) showed significant fluorescence (Figure 32). Seeded pH 2.0 fibrils with minimal degradation exhibited ThT fluorescence even stronger than that of degraded fibrils. Some short incubation time pH 2.0 HET-s(218–289) fibrils also showed significant amounts of fluorescence,

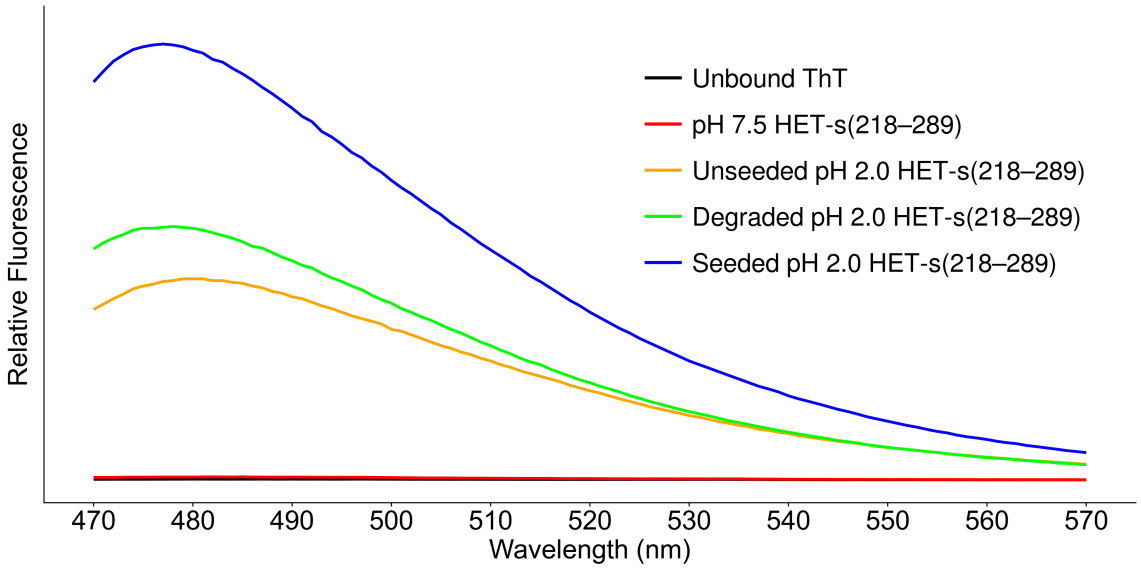

Figure 32: Induced ThT fluorescence on binding to several forms of HET-s(218–289).

although their diffraction patterns were characteristic of β-solenoid structure. We attribute this fluorescence to the presence of a low proportion of degraded fibrils with the stacked β-sheet conformation, enough to bind a significant fraction of the ThT and induce fluorescence, but not enough to greatly affect the diffraction pattern. The non-infectious pH 2.0 fibrils described by Sabaté et al. (2007) also exhibited strong ThT fluorescence, suggesting that those fibrils may have been degraded and contained significant amounts of stacked β-sheet structures.

IV.2 Undegraded HET-s(218–289) polymorphs formed under acidic conditions

IV.2.1 pH dependence of HET-s(218–289) polymorphism

In order to determine the pH dependence of HET-s(218–289) polymorphism, we found acidic conditions where the fibrils would not proteolyze. These fibrils were recombinantly expressed and purified as described earlier (Chapter III.1.1), but desalted and fibrillized into either 50 mM phosphoric acid or citric acid from pH 2.0–3.0 in 0.25 pH unit increments. X-ray fiber diffraction and negative stain EM were performed on each of these preparations (Figure 33). Diffraction patterns from pH 2.00 and 2.25 fibrils (Figure 33A, B, K, L) exhibited strong equatorial diffraction maxima at ~11 Å, indicative of the inter-sheet spacing

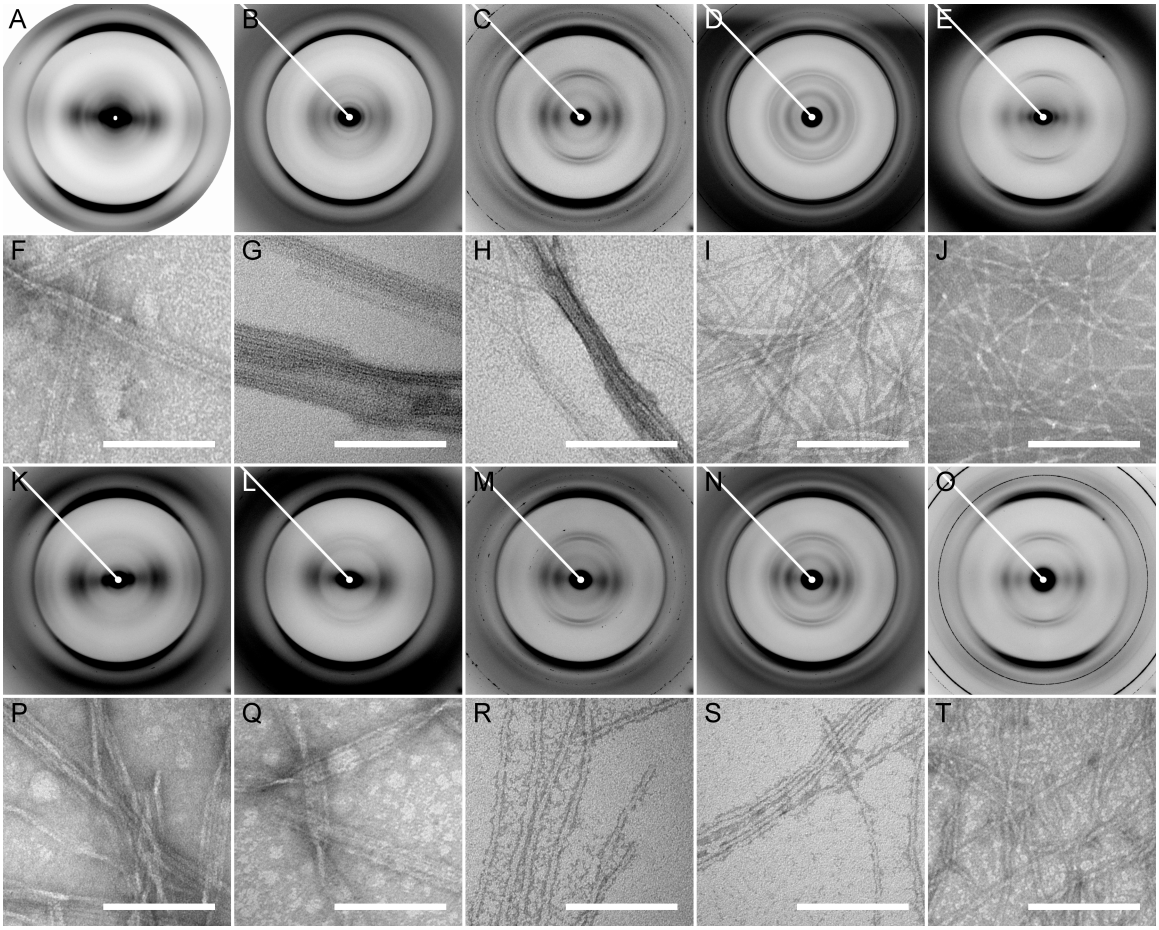

Figure 33: X-ray fiber diffraction and negative stain EM of HET-s(218–289) fibrillized over a low pH range. A-E) Fiber diffraction and F-J) EM of pH 2.00, pH 2.25, pH 2.50, pH 2.75, pH 3.00 50 mM citric acid fibrils. K-O) Fiber diffraction and P-T) EM of pH 2.00, pH 2.25, pH 2.50, pH 2.75, pH 3.00 50 mM phosphoric acid fibrils. Scale bars = 100 nm.

Table 3: CCs from ~30–4 Å resolution (~0.03–0.25 $Å^{-1}$) of low pH fibrils in different buffers.

pH	CC
2.00	0.87
2.25	0.84
2.50	0.97
2.75	0.96
3.00	0.76

of a stacked β-sheet architecture. Even after long exposures and with very low background scattering, the only diffraction on the meridian at these pH values was the intense ~4.7 Å cross-β reflection, showing that the repeat distance along the fibril axis corresponds to the thickness of a single β-strand. Diffraction patterns from pH 2.50–3.00 fibrils (Figure 33C–E, M–O) showed a series of equatorial intensities roughly decreasing with distance from the origin, indicating a structure that approximates a solid cylinder (Wille et al. 2009). These patterns also contained meridional reflections at ~9.4 Å and ~4.7 Å, indicating two-layered cross-β structures. These patterns are consistent with patterns from HET-s(218–289) fibrillized at pH 7.5 (Figure 28D 18), indicating that these fibrils share a common two-layer, approximately cylindrical structure. The structure probed by these diffraction patterns was confirmed by ssNMR (Wan et al. 2013) to be the same as that of the previously determined atomic model (Van Melckebeke et al. 2010), a two-rung β-solenoid. The differences in structure as assessed by X-ray diffraction corresponded to differences in morphology seen by EM (Figure 33F-J, P-T). The stacked β-sheet fibrils tended to aggregate parallel to each other, forming heterogeneous ribbon-like aggregates (Figure 33F, G, P, Q), while the β-solenoid fibrils appeared as dispersed homogeneous filaments (Figure 33H-J, R-T).

The equators for each diffraction pattern were background subtracted and plotted (Figure 34). For each pH, equatorial plots from citric acid and phosphoric acid fibrils displayed the same general features (Figure 34). At each pH, equators generally had high CCs between each buffer (Table 3), indicating similar architectures. The CC for the pH 3.00 specimens is low, probably owing to a combination of background and disorientation, an evidenced

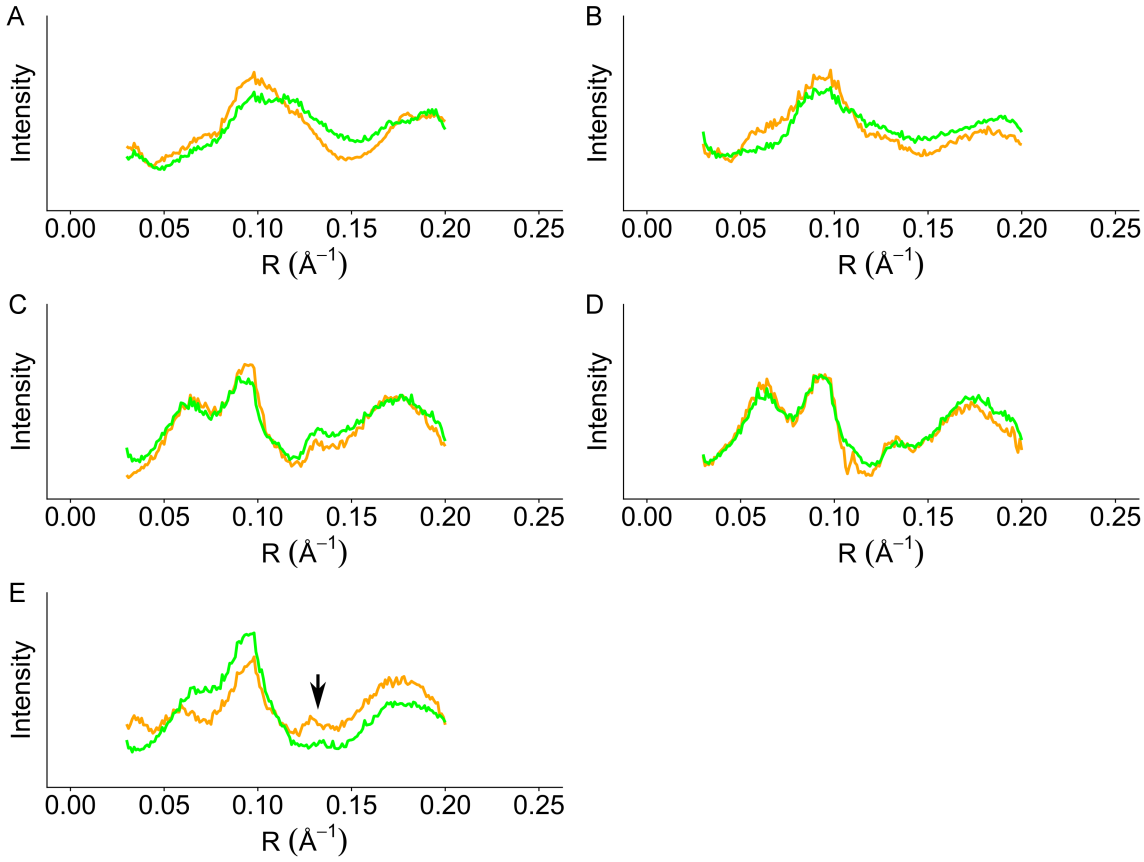

Figure 34: Equatorial plots of low pH citric acid and phosphoric acid fibrils. A) pH 2.00, B) pH2.25, C) pH 2.50, D) pH 2.75, E) pH 3.00. Green: phosphoric acid. Orange: citric acid. Arrow indicates superimposed 9.4 Å meridional reflection.

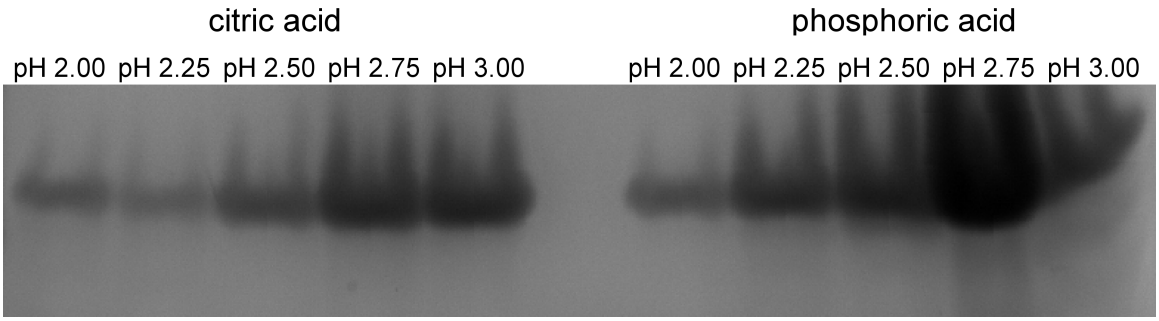

Figure 35: SDS-PAGE of resuspended low pH fiber diffraction specimens.

by the apparent presence of the 9.4 Å meridional reflection and 8.5 Å subsidiary maximum superimposed on to the pH 3.00 citric acid equatorial plot (Figure 34E).

In order to determine if these fibrils were degraded, SDS-PAGE was performed on resuspended fiber diffraction specimens used in Figure 33 (Figure 35).

IV.2.2 Molecular modeling of stacked β-sheets

Diffraction patterns from stacked β-sheet amyloids have historically been interpreted with the aid of data from mechanical manipulation of specimens, as in the case of supercontracted epidermin (Rudall 1946), or with the help of constraints provided by crystallinity and simple repeating amino acid sequences, as in the case of the lacewing fly egg stalk (Geddes et al. 1968). These approaches are not available for HET-s(218–289), but we can identify architectural features by comparing experimental data with data calculated from models of stacked β-sheets — an approach that has previously been used qualitatively (Wille et al. 2009). In order to provide a quantitative comparison with the analysis described here, we constructed a stacked β-sheet model of HET-s(218–289), retaining the β- and random-coil regions from the β-solenoid, but re-arranging them to form a stacked β-sheet structure (Figure 36A). Apart from avoiding close atomic contacts, no other constraints were used. The model is not meant to represent the actual structure of pH 2.0 fibrils, but is intended to demonstrate the general appearance of diffraction from stacked β-sheets.

A diffraction pattern of the model was calculated using the same temperature factors as the β-solenoid calculations (Table 1), making the β-strands the primary contributors to

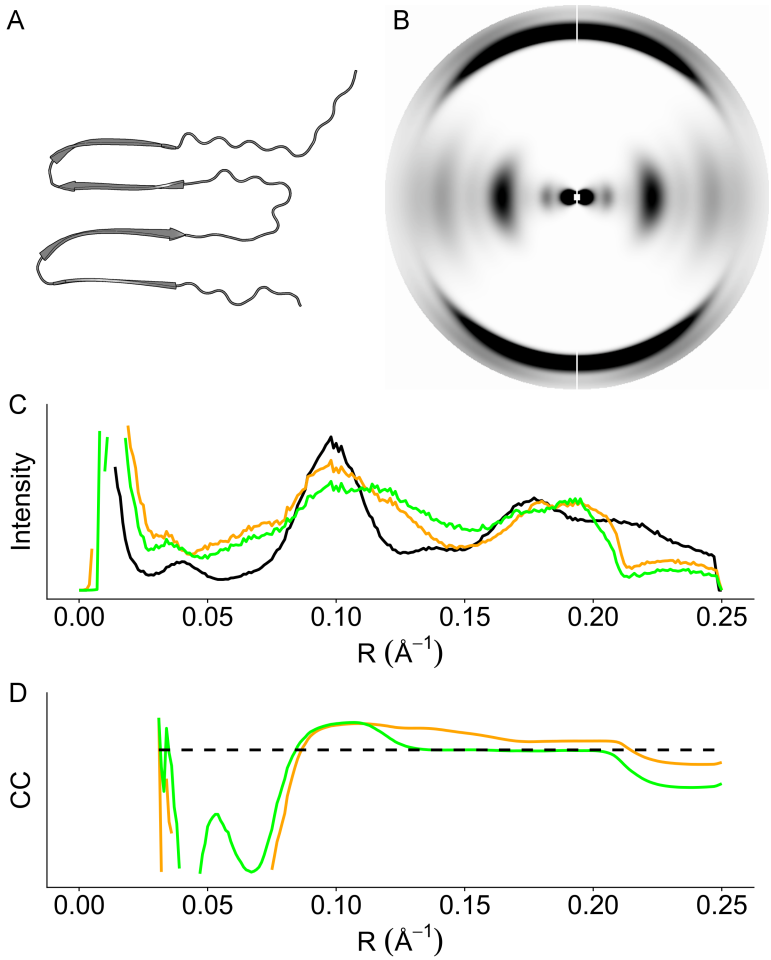

Figure 36: Molecular model of a stacked β-sheet. A) Stacked β-sheet model constructed from the HET-s(218–289) β-solenoid structure (PDB: 2KJ3). B) Calculated diffraction pattern from the model in A). C) Equatorial sector plots of calculated and experimental data. Black line represents calculated stacked β-sheets, orange line represents data from fibrils formed in pH 2.0 citric acid, and green line represents data from pH 2.0 phosphoric acid. D) CCs between calculated equators and experimental data as a function of cumulative resolution range, starting at $R = 0.03$ Å^{-1}. Orange line: pH 2.0 citric acid. Green line: pH 2.0 phosphoric acid. Black dashed line is at CC = 0.8.

the pattern. The calculated diffraction pattern (Figure 36B) shows the ~4.7 Å meridional reflection and the ~10 Å equatorial intensity maximum expected from a stacked β-sheet model. Equatorial plots of experimental pH 2.0 patterns and the calculated model pattern (Figure 36C) showed the same general distributions, though as with the two experimental patterns, there were variations in detail. CCs between the experimental and calculated data were calculated to various resolutions (Figure 36D). The correlation below ~12 Å resolution (~0.08 $Å^{-1}$) is poor but higher resolution data improve the fit, leading to good correlations up to ~5 Å (~0.20 $Å^{-1}$) resolution for pH 2.0 citric acid and phosphoric acid fibrils (CC = 0.86 and 0.80, respectively). Low-resolution fiber diffraction data correspond to structural details such as fibril diameter while data above 5 Å resolution begin to correspond to individual peptide structures. The high CCs between the models and experimental data at intermediate resolutions indicate close similarities in the main chain architecture.

IV.2.3 The effect of salt concentration on aggregation

Upon adjusting freshly purified HET-s(218–289) monomer solution to 1 M NaCl at a pH between 2 and 3, immediate precipitation of fibrils occurred. The precipitated fibrils exhibited stacked β-sheet amyloid patterns (Figure 37A) similar to those of fibrils formed at pH 2.0 without NaCl. A variety of divalent and monovalent cation salts was used, each yielding fibrils with a similar stacked β-sheet diffraction pattern (Figure 38). The addition of 1 M NaCl when fibrillizing HET-s(218–289) at pH 7.5 produced no noticeable change in fibrillization time, and the resultant fibrils maintained a β-solenoid diffraction pattern (Figure 37B). The addition of 1 M ammonium sulfate at pH 2.0 induced immediate formation of disordered fibrils, which produced poorly oriented diffraction patterns (Figure 37C). At pH 7.5, the addition of 1 M ammonium sulfate resulted in immediate formation of β-solenoidal fibrils (Figure 37D). These results indicate that formation of stacked β-sheet structures is preferred at lower pH values and masking of charges through the addition of salt appears to overcome fibrillization barriers at low pH. Fibrillization at pH 7.5 is unaffected by NaCl, but ammonium sulfate greatly enhances fibrillization rate, indicating

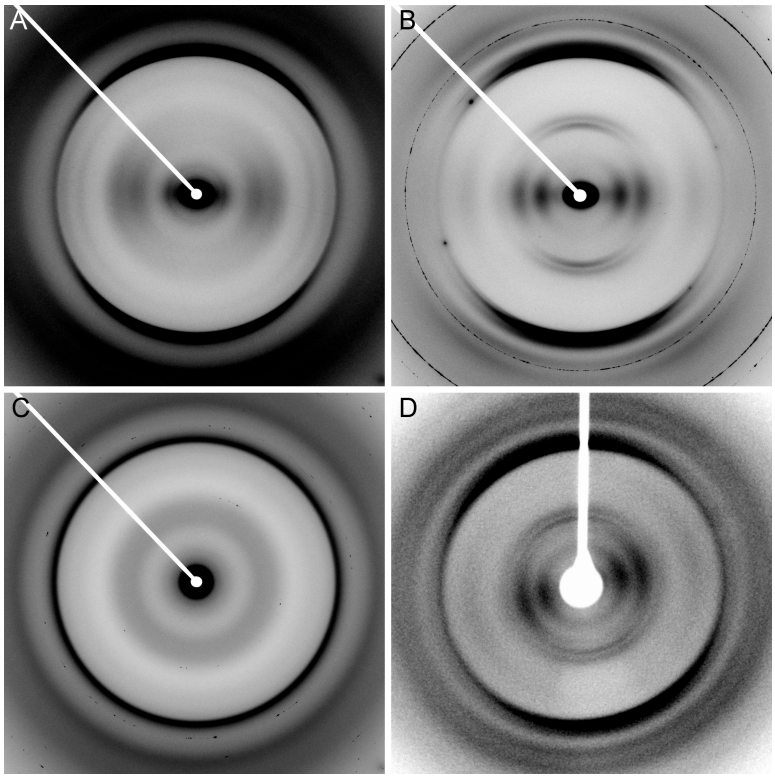

Figure 37: X-ray fiber diffraction from HET-s(218–289) fibrillized in high salt concentrations. Fibrils formed in 1 M NaCl at A) pH 2.0 and B) pH 7.5. Fibrils formed in 1 M ammonium sulfate at C) pH 2.0 and D) pH 7.5.

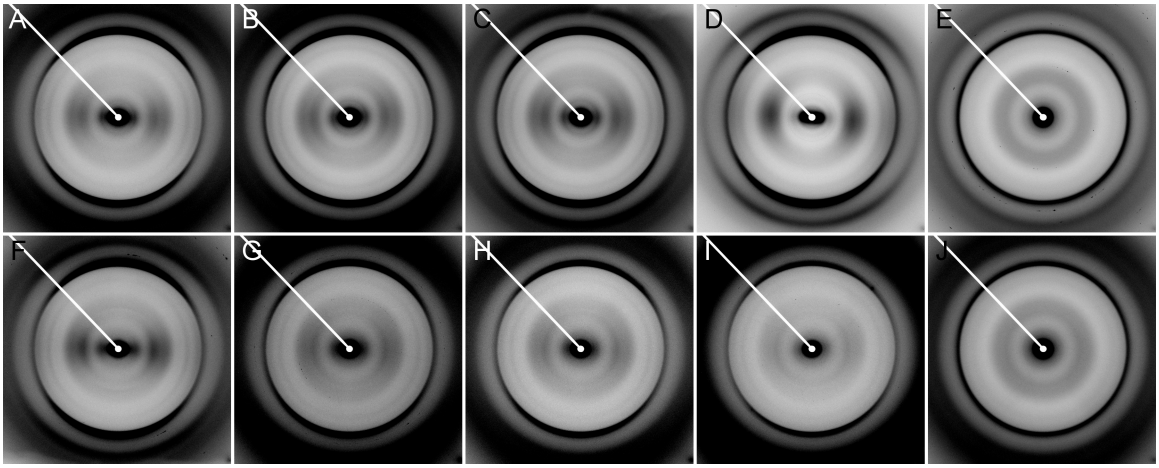

Figure 38: X-ray fiber diffraction patterns from HET-s(218–289) fibrillized at pH 2.0 with different salts. Final concentration of each salt was 1 M. A-E) 50 mM citric acid and F-J) 50 mM phosphoric acid, with NaCl, KCl, $CaCl_2$, $MgCl_2$, $(NH_4)_2SO_4$ respectively.

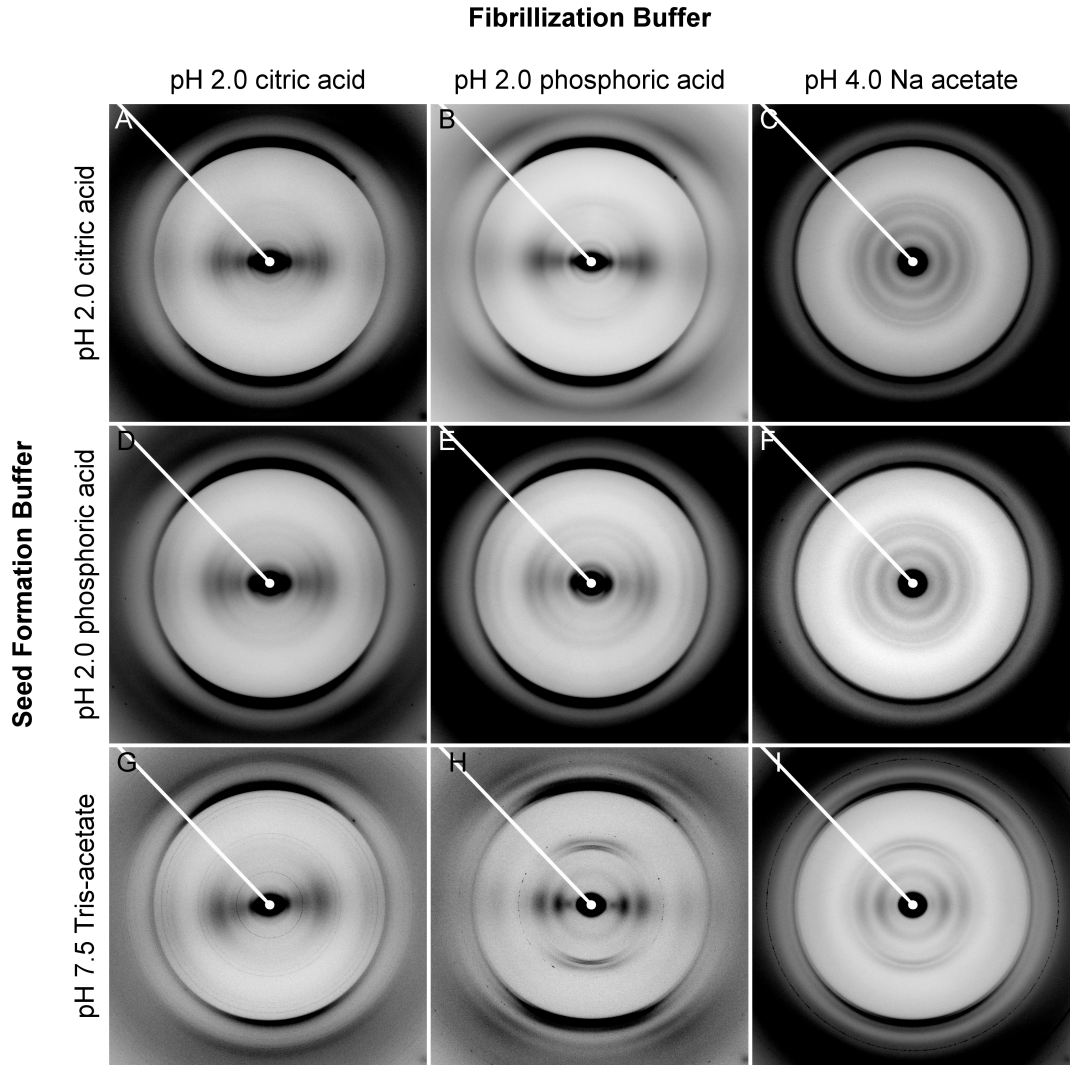

Figure 39: X-ray fiber diffraction patterns from seeded HET-s(218–289) fibrils.

that at this pH, charge interactions may not be barriers to fibrillization, but hydrophobic collapse may be a significant driving factor.

IV.2.4 Effects of seeding on fibril structure

Freshly purified solutions of HET-s(218–289) were seeded with pre-formed fibrils (1:10 molar ratio of seed to monomer) and the resultant fibrils were examined by X-ray fiber diffraction (Figure 39). Fibrils formed in pH 2.0 buffers seeded with pH 2.0 fibrils produced diffraction patterns similar to those of their seeds (Figures 33A, K, and 39A, B, D, E).

However, there was no substantial decrease in fibrillization time, so whether or not seeding actually occurred is undetermined. Fibrils formed at pH 2.0 seeded with pH 7.5 β-solenoid fibrils gave results depending on the pH 2.0 buffer used. With β-solenoid seeds, fibrils formed in citric acid buffer exhibited stacked β-sheet structures (Figure 39G), as if unseeded, while fibrils formed in phosphoric acid buffer exhibited β-solenoid structures (Figure 39H). Seeding experiments were also carried out on solutions of HET-s(218–289) in pH 4 sodium acetate, in which β-solenoid fibrils form but at lower fibrillization rates than at pH 7.5. The slower fibrillization should increase any templating effect that seeds might have. In all cases (Figure 39C, F, I) pH 4 solutions yielded β-solenoid fibrils. These experiments indicate that at pH 2.0, although β-solenoid fibrils are not nucleated spontaneously, the addition of β-solenoid seeds can induce homogeneous templating under certain buffer conditions. At higher pH values, where β-solenoid fibril formation occurs, the β-solenoidal structure formation is not perturbed by seeds of a different structure. While this confirms that stacked β-sheets do not act as efficient structural templates at higher pH, it does not address the issue of nucleation effects, that is, whether or not heterogeneous seeding occurs.

IV.2.5 Heterogeneous seeding between polymorphic structures

In order to determine if heterogeneous seeding was occuring between stacked β-sheet and β-solenoid fibrils, fibrillization kinetics were assayed and compared.

Fibrillization kinetics assays were carried out using a modified version of one described elsewhere (Wasmer et al. 2010), and performed in triplicate. HET-s(218–289) monomers were purified into 500 mM acetic acid and fractionated into 60 nM aliquots as determined by absorbance at 280 nm (A280). Aliquots were immediately lyophilized and the resultant powder was dissolved in 200 µL of hexafluoroisopropanol (HFIP), lyophilized again, and stored at −20 °C. For assays, powder was resuspended in 1.5 mL of 175 mM acetic acid. Assays were started by the 1:1 addition of 1 M Tris-HCl pH 8.0 and mixing by inversion, providing a final protein concentration of 20 µM. For seeded assays, 6 nM (for a final concentration of 2 µM, a 1:10 molar ratio) of seed fibrils were moved into the Tris-HCl buffer by ultracentrifugation and resuspension, and probe sonicated for 30 s with ~90 W of

power immediately prior to use. Stacked β-sheet fibrils were first washed with 50 mM citric acid pH 2.0 three times by centrifugation and resuspension to remove any monomers or small aggregates without inadvertently forming β-solenoids. Serially seeded assays were performed by treating fibrils from previous passages as described above. Seeds from triplicates were serially passaged individually. To prevent cross contamination, assays were performed with disposable cuvettes.

Unseeded and stacked β-sheet-seeded first passage assays were monitored using optical density at 400 nM (OD400) measured every 10 min for 240 min. Assays seeded with β-solenoid or serially passaged stacked β-sheet-seeded solutions were measured at 1 min intervals for 20 min followed by measurements every 10 min up to 120 min. Assays to assess early stacked β-sheet seeding kinetics were measured at 1 min intervals for 20 min followed by 10 min intervals until 240 min was reached. Prior to each measurement, cuvettes were mixed by inverting several times. For display, the averages of the triplicates were fit to a Boltzmann function:

$$y = \frac{A_1 - A_2}{1 + e^{(x - x_0/dx)}} + A_2 \tag{IV.1}$$

where A_1 is the low limit, A_2 is the high limit, x_0 is the half-amplitude point, and dx is the width. Standard deviations between triplicates are shown as error bars.

OD400 and normalized values of OD400 are shown in Figure 40 as a function of elapsed time for unseeded solutions and solutions seeded with stacked β-sheet fibrils or β-solenoid fibrils. The unseeded kinetics appeared to follow a roughly sigmoidal curve with a brief lag-phase. Solutions seeded with β-solenoid fibrils exhibited no apparent lag-phase and much faster fibrillization than unseeded solutions. Solutions seeded with stacked β-sheet fibrils exhibited a rapid initial rise in OD400 (Figure 40A), but proceeded to completion (Figure 40B) more slowly than either the unseeded or the β-solenoid-seeded solution. The rapid initial rise is seen more clearly in Figures 40C and 40D, for which the stacked β-sheet-seeded experiments were repeated with increased sampling in the first 20 min. Light scattering and rate to completion are slightly greater in the experiments with increased

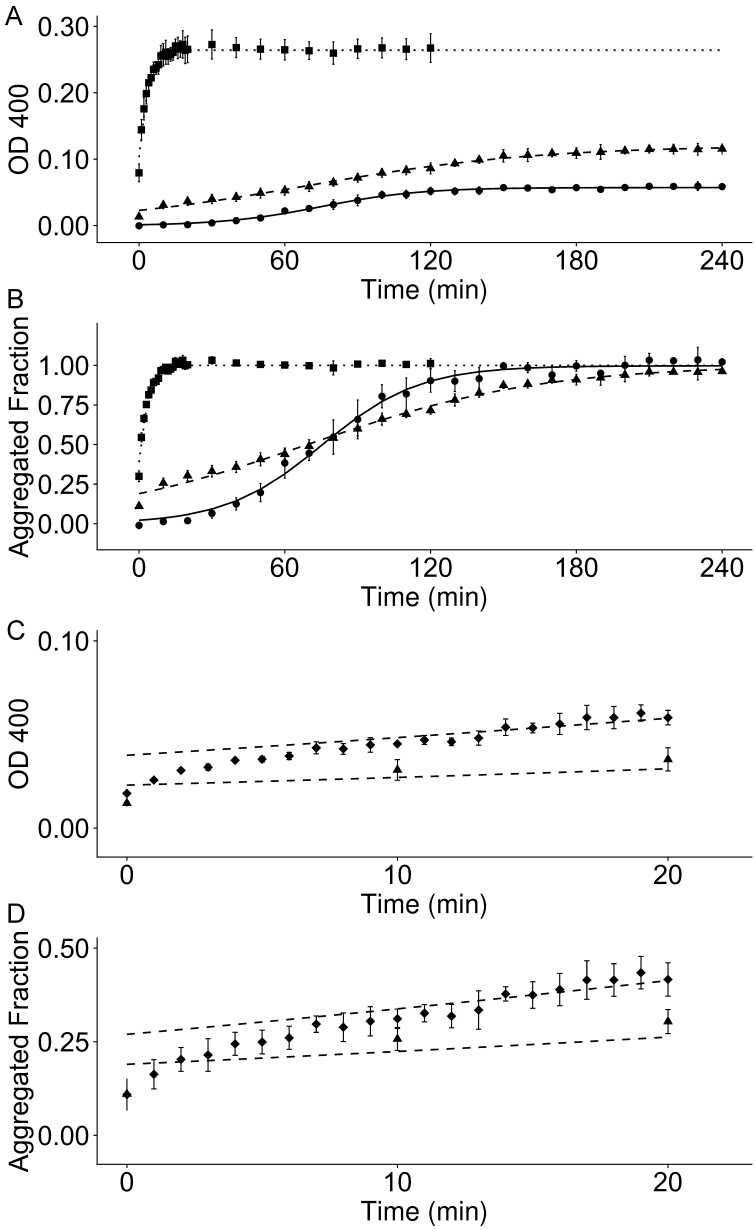

Figure 40: Fibrillization kinetics of seeded and unseeded assays. A) Raw and B) normalized assays of unseeded, β-solenoid seeded and stacked β-sheet seeded fibrils. C) Raw and D) normalized stacked β-sheet seeded assay early kinetics with extra readings. Solid line and (●): unseeded fibrillization. Dashed line and (▲): fibrillization with stacked β-sheet seeds. Dotted line and (■): fibrillization with β-solenoid seeds. Dash-dotted line and (⧫): fibrillization with β-solenoid seeds and early kinetics readings. Error bars represent standard deviation of triplicates.

sampling, probably owing to increased fibril fragmentation during mixing prior to each reading, leading to an increased number of nuclei (Cohen et al. 2013).

Although the final OD400 values for each seeding condition were significantly different (Figure 40A), supernatants from ultracentrifugation of fibril solutions after 4 h showed no detectable protein using A280, indicating complete fibrillization. These observations indicate that the differences in final OD400 values were due to differences in aggregate size. The rapid early increase in OD400 with no lag-phase for both the β-solenoid and stacked β-sheet-seeded solutions indicates that seeding is occurring in the initial aggregation process.

Serial seeding from stacked-sheet fibrils increases fibrillization rates — fibrils formed by seeding with stacked β-sheet fibrils (first passage) were used as seeds in subsequent fibrillization kinetics assays, to four passages (Figure 41). Consecutive passages showed progressively faster kinetics, but reached a maximum by the third passage, for which the kinetics were within experimental error of the kinetics shown by β-solenoid-seeded solutions (Figure 40).

Seeded fibrillization kinetics assays were also carried out using degraded pH 2.0 HET-s(218–289) fibrils to seed full-length monomer solutions (Figure 42). While the fibrillization kinetics appears to be slighly faster for the solutions seeded with degraded fibrils, the overall features of heterogeneous seeding are present: an initial rapid increase in aggregation followed by a slower rate to completion. The fact that the kinetics between solutions seeded with degraded and undegraded fibrils are comparable suggests that heterogeneous seeding does not make use of the complete HET-s(218–289) structure, but instead relies on fragments of secondary structure.

IV.2.6 Amyloid polymorphisms and the stacked β-sheet architecture

Amyloids were for many years believed to have a common fold consisting of stacked β-sheet architecture, which likely represented a generic low-energy protein fold (Astbury et al. 1935; Rudall 1946; Sunde et al. 1997; Jahn et al. 2010). This commonality, with variations in detail, does appear to hold for short synthetic amyloidogenic peptides (Nelson et al. 2005; Sawaya et al. 2007), which have been the subject of most detailed amyloid

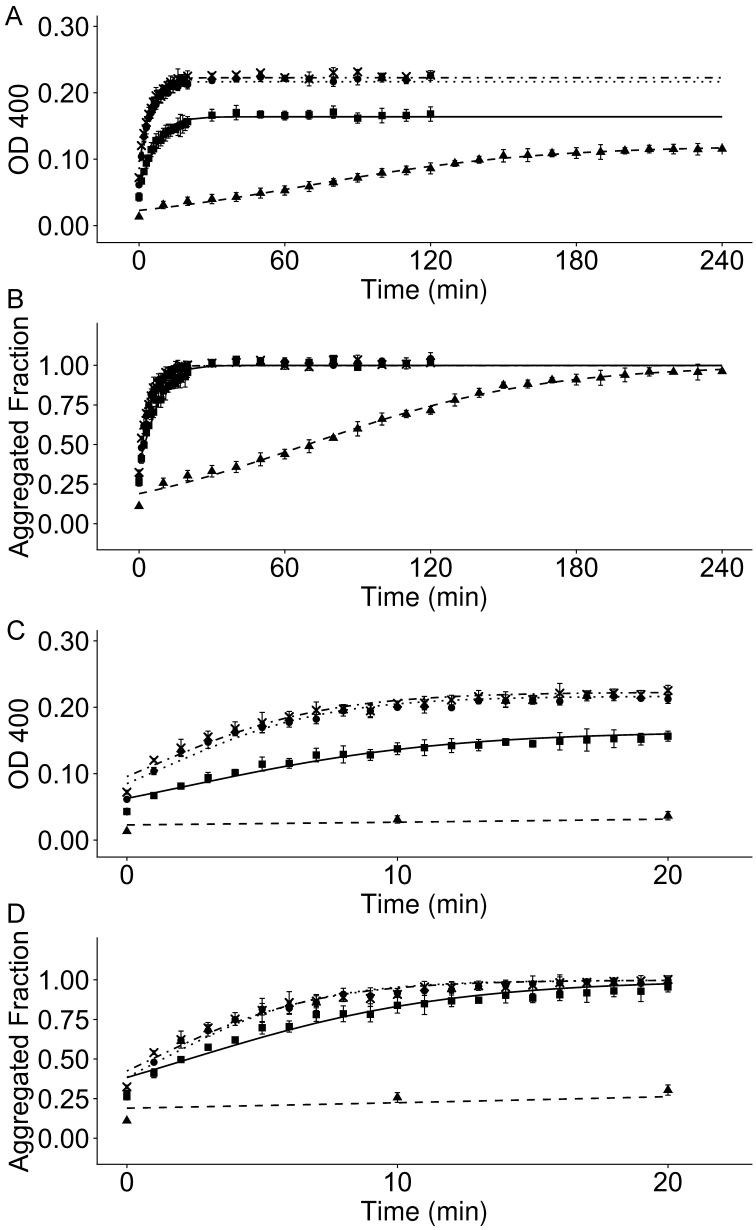

Figure 41: Serially seeded stacked β-sheet fibrillization kinetics. A) Raw and B) normalized kinetics over the full time course. C) Raw and D) normalized early kinetics. Dashed line and (▲): first passage. Solid line and and (■): second passage. Dotted line and (●): third passage. Dash-dot line and (×): fourth passage. Error bars represent standard deviation of triplicates.

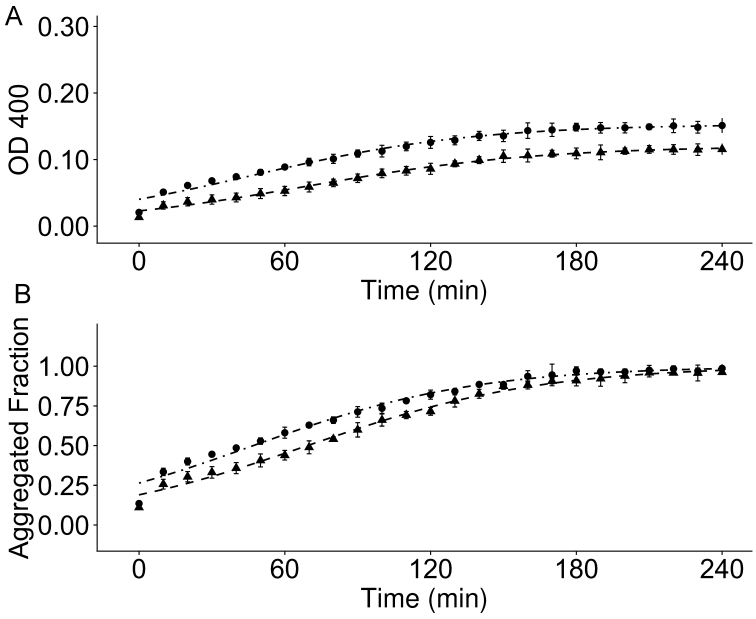

Figure 42: Seeded fibrillization kinetics with undegraded and degraded stacked β-sheets.A) Raw and B) normalized kinetics. Dashed line and (▲): undegraded stacked β-sheets. Dash-dot line and (●): degraded stacked β-sheets. Error bars represent standard deviation of triplicates.

structural studies, but as HET-s(218–289) illustrates particularly well, biological amyloids may have more complex structures. These complex structures retain the fundamental cross-β motif (β-strands perpendicular to the fibril axis) (Rudall 1946), but often do not retain the simple regular inter-sheet stacking that gives rise to the equatorial ~10 Å intensity maximum. While the ssNMR structure of HET-s(218–289) provides a highly detailed view of a particularly complicated amyloid, a number of pathological amyloids have also shown complex structures, including the Alzheimer's-associated Aβ 1–40 (Petkova et al. 2005; Paravastu et al. 2008; McDonald et al. 2012; Lu et al. 2013), diabetes-associated islet amyloid polypeptide (Luca et al. 2007), and PrP^{Sc} (Govaerts et al. 2004; Wille et al. 2009).

The HET-s(218–289) polymorphs studied here all have stacked β-sheet architecture. If stacked β-sheets are simply a generic low energy state, this would suggest that HET-s(218–289) polymorphs can be considered denatured states that occur when the conditions are not conducive to proper β-solenoid folding. In the case of degraded HET-s(218–289), this is caused by alterations in the primary structure. In the case of undegraded HET-s(218–289),

this appears to be caused by acidic conditions which may preclude intra- and inter-molecular interactions that allow for folding. However, the ability of both these polymorphs to heterogeneously seed the formation of β-solenoids indicates that there is sufficient structure left to induce some level of templating activity. However, the unique kinetics profiles from heterogeneous seeding suggest distinct differences from homogeneous seeding.

Although aggregation was rapid in the initial stages of heterogeneously-seeded growth, the solutions did not reach the high OD400 values observed for homogeneous β-solenoid seeding (Figure 40). The initial rapid kinetics are probably related to the extension of seeds into fibrils, that is, true fibrillization, which is followed by the formation of large aggregates of individual fibrils. This slow aggregation process dominates the later OD400 readings, which can be fitted quite well by a sigmoid curve. The apparent rate to completion (Figure 40B) is slower than that seen for unseeded and homogeneously seeded fibrils, suggesting that the aggregation process is not identical for the different seeding protocols.

The two aggregation processes (fibrillization and subsequent fibril aggregation) are probably present in unseeded and β-solenoid-seeded assays, but may not be apparent because of similar rates. The processes may be temporally separated in heterogeneously seeded assays because the formation of large β-solenoid aggregates first requires β-solenoid fibrillization from stacked β-sheet seeds. The rate of formation of large aggregates of heterogeneously seeded fibrils may be slower than homogeneously seeded fibrils because of the amount of stacked β-sheet present, but this effect is diminished in serial propagation, which effectively dilutes the stacked β-sheet segments. Monomer and seed solutions are in a 10:1 molar ratio, so by the third passage, the slower rates associated with heterogeneous seeding fade into experimental error.

Weak seeding by low pH fibrils has been seen previously, including *in vivo* transfection assays showing very low but not complete lack of infectivity (Sabaté et al. 2007). However, those results showed modest fibrillization rate increases, but not the distinct changes in kinetic profiles observed here. Increased agitation of heterogeneously seeded assays may produce a kinetics profile resembling an attenuated homogeneously seeded assay, as seen in our assay of early heterogeneous seeding. Heterogeneous seeding of HET-s(218–289) has

also been observed with a homolog found in the fungus *Fusarium graminearum*, although the seeding has been attributed to high levels of structural similarity as both form two-rung β-solenoids (Wasmer et al. 2010), and even in this case homogeneous fibrils appear to be preferred (Benkemoun et al. 2011).

The heterogeneous seeding in our experiments resembles the adaptation mechanism proposed for the transition from recombinant PrP (recPrP) amyloid to infectious PrP^{Sc} prion (Makarava et al. 2011). RecPrP has a distinctly different architecture from that of brain-adapted strains such as scrapie-derived prions or synthetic prions derived from recPrP (Wille et al. 2009). Like the HET-s(218–289) amyloid formed at pH 2, recPrP has a stacked β-sheet architecture, while PrP^{Sc} has a more complicated, multi-tiered structure probably related to that of infectious HET-s(218–289). In each case, the stacked β-sheet architecture displays the least biological activity and increasing infectivity is concomitant with structural complexity (Legname et al. 2004; Wille et al. 2009). Stacked β-sheet structures seem to be accessible to many proteins under otherwise denaturing conditions, suggesting that this architecture is a low-energy state common to all proteins (Astbury et al. 1935; Chiti and Dobson 2006). However, fibrillization conditions can affect details of the stacked sheet architecture and eventually lead to distinct phenotypes, indicating that stacked-sheet fibrils share features with the end-state infectious structures (Makarava et al. 2011).

The concomitance between structural complexity and self-propagation is likely to be common to prions in general. Q/N-rich yeast prions may be an exception; scrambling of the prion domains in Ure2p and Sup35p often yields functional prions, indicating that the prion-forming activity is largely independent of the precise sequence (Ross et al. 2004; Ross et al. 2005; Shewmaker et al. 2008). The robust infectivity and phenotypic propagation of these prions may simply be due to the Q/N-rich sequence. Amide ladders formed from Q/N side-chain interactions between subunits appear to play a key role in prion assembly and infectivity, and the particular spacing of amide interactions within the sequence appears to define the prion phenotype (Shewmaker et al. 2008; Toyama et al. 2007). Fiber diffraction from the prion-forming region of Sup35p has suggested that this structure collapses into a stacked β-sheet on dehydration, indicating that the hydrated form does not possess a

well-packed core (Kishimoto et al. 2004). These considerations, however, do not apply to HET-s, PrP, or many other self-propagating amyloidogenic molecules, since there are major differences in function and composition between the Q/N-rich yeast prions and other prions including HET-s. Yeast prions sequester protein leading to a loss of function while HET-s causes a gain of function, that is heterokaryon incompatability (Saupe 2011; Debets et al. 2012). This gain of function is similar to what is seen with PrP^{Sc}, where the diseased state is not caused by the loss of PrP^{C} function, but by the gain of toxicity (Hetz et al. 2003). In terms of composition, infectious folding of HET-s(218–289) seems to be driven by the formation of salt-bridges and a packed hydrophobic core (Van Melckebeke et al. 2010) rather than a large number of amide interactions. Interactions between formal charges also appear to play a role in the formation of recPrP, as subtle changes in pH affect nucleation and the formation of oligomeric structures that are off-pathway from amyloid formation (Baskakov et al. 2002; Baskakov 2004).

The ability of the low pH amyloid form of HET-s(218–289) to nucleate the wild-type infectious structure *in vitro* shows that amyloids with decidedly different architectures can interact with one another, and that heterogeneous seeding does not require *in vivo* cofactors, but can be achieved in minimal systems. Although the polymorphs studied here are to some extent contrived, being apparently a low-energy state that compensates for repulsive charge interactions that are unlikely to occur *in vivo*, the heterogeneous seeding indicates that there is a preferred prion structure that can be reached regardless of the structure of the nucleating agent. In the case of recPrP, this adaptation requires several passages through animals (Makarava et al. 2012a), but HET-s(218–289) arrives at the infectious fold immediately, although reproduction of fibrillization kinetics requires several passages. Heterogeneous seeding can thus provide a relatively simple mechanism for strain adaptation and interspecies prion transmission.

CHAPTER V

Studying self-propagation of HET-s(218–289) with site-directed mutagenesis

V.1 Site-directed mutagenesis of HET-s(218–289)

HET-s(218–289) forms a two-rung solenoid (Figure 43), with a long flexible loop joining the two rungs, a pair of buried hydroxyl-containing residues, three salt-bridges, and two asparagine ladders. In order to study the role of these structural units in the proper folding

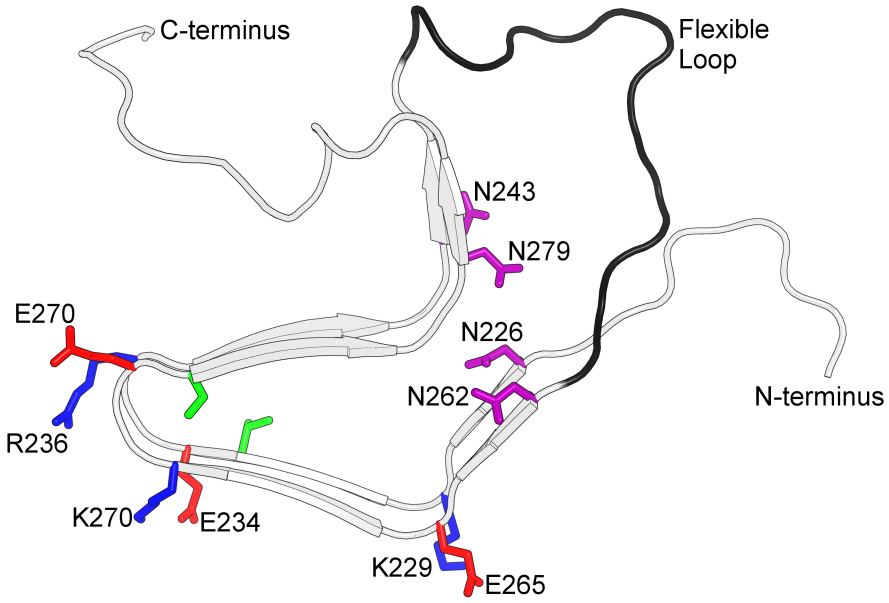

Figure 43: Structure of HET-s(218–289) and positions of mutated residues. Model is from the solid state NMR structure (PDB: 2kj3). Green: buried polar residues. Red and blue: positive and negative salt-bridge residues, respectively. Purple: asparagine ladders. Black: flexible loop.

and self-propagation of HET-s(218–289), we used site-directed mutagenesis to modify these interactions. Site-directed mutagenesis was carried out using a two-stage QuikChange (Agilent Technologies, Santa Clara, CA) protocol (Wang and Malcolm 1999). Oligonucleotide primers were synthesized by Integrated DNA Technologies (Coralville, IA).

Site-directed mutagenesis was used to replace individual residues involved in salt-bridges and asparagine ladders, and buried hydroxyl residues, with alanine, effectively abrogating

interactions within individual pairs. Combination mutants were also made, replacing both of the buried hydroxyl residues, all positive or negative salt-bridge partners, all permutations of asparagines that abrogate both ladders, and in two mutants, residues that abrogate all solvent-exposed surface interactions. Mutations were also made to reverse or scramble the flexible loop sequence, and to remove the loop residues 251–253; the Δ251–253 mutant had previously been shown to form infectious fibrils (Ritter et al. 2005). Loop residues (residues 247–261) were mutated to TTQDSIRIGGHLAAA for the reversed-loop, and ATRIGLIQGTHASDA for scrambled-loop mutants. Mutants are listed with abbreviations in Table 4.

To determine the molecular architecture of each mutant, X-ray fiber diffraction patterns were obtained for each mutant (Figure 44). Diffraction patterns were compared to wild-type β-solenoid diffraction patterns by indexing meridional spacings and calculating equatorial CCs (Table 4). The mutant molecular architectures fell into two groups: β-solenoid and stacked β-sheet (Table 4). Mutants that formed β-solenoids were subjected to fibrillization kinetics (Figure 45, Table 4) and guanidine denaturation (Figure 46, Table 4) assays to compare the effects of the mutations on the biophysical properties of the β-solenoid structure. The methods used for these assays are described in the next section.

V.2 Methods for biophysical characterization

V.2.1 Fibrillization kinetics assays

The fibrillization kinetics assays used to characterize the HET-s(218–289) mutants were similar to those described in Chapter IV.2.5. The methods of protein purification and HFIP treatment to remove residual secondary structures were identical. The assays used the same buffers, cuvettes, and OD400 readout, with the main difference being an increased final protein concentration of 60 µM. Protein concentration was increased three-fold from previous assays because of the significantly reduced fibrillization kinetics of certain mutants. Readings for each assay were taken at 10 min intervals until a steady state was reached. Assays for each mutant were done in triplicate and averaged readings were fitted to an empirical equation (Nielsen et al. 2001):

Table 4: Molecular architecture, fibrillization kinetics, and chemical stability of HET-s(218–289) mutants

Mutation	Mutation Type	Abbreviation	9.4Å meridional	Equatorial CC	Architecture	Lag time (min)	kapp (min-1)	m1/2 (M)
wild-type	—	wt	yes	1.00	b-solenoid	21.8±0.6	0.103±0.002	2.77±0.03
reversed loop	loop	RL	no	0.63	stacked b-sheet	—	—	—
scrambled loop	loop	SL	no	0.66	stacked b-sheet	—	—	—
D251–253	loop	D251–253	yes	0.96	b-solenoid	147±2	0.071±0.004	2.30±0.1
T233A	buried polar	PA	yes	0.91	b-solenoid	23.0±1	0.133±0.007	2.94±0.02
S273A	buried polar	PB	yes	0.83	b-solenoid	77.0±2	0.103±0.007	1.98±0.02
T233A-S273A	buried polar	PAB	yes	0.99	b-solenoid	38.0±2	0.098±0.005	2.73±0.06
E234A	salt-bridge	SA-	yes	0.99	b-solenoid	28.3±0.9	0.151±0.006	2.76±0.03
E265A	salt-bridge	SB-	yes	0.94	b-solenoid	35.0±2	0.120±0.009	2.53±0.02
E272A	salt-bridge	SC-	yes	0.99	b-solenoid	94.0±2	0.106±0.005	3.40±0.2
E234A, E265A, E272A	salt-bridge	SABC-	yes	0.98	b-solenoid	219±3	0.051±0.003	2.27±0.06
K229A	salt-bridge	SB+	yes	0.90	b-solenoid	66.0±1	0.138±0.006	3.20±0.1
K270A	salt-bridge	SA+	yes	0.98	b-solenoid	30.0±1	0.170±0.01	2.63±0.06
R236A	salt-bridge	SC+	yes	0.99	b-solenoid	59.0±1	0.134±0.007	2.78±0.07
K229, K270A, R236A	salt-bridge	SABC+	yes	—	b-solenoid	111±2	0.078±0.003	1.94±0.08
N226A	N-ladder	NA	yes	0.94	b-solenoid	95.0±3	0.087±0.006	1.30±0.2
N243A	N-ladder	NB	yes	0.96	b-solenoid	91.0±2	0.093±0.005	1.84±0.05
N262A	N-ladder	NC	yes	0.89	b-solenoid	124±4	0.068±0.005	1.40±0.2
N279A	N-ladder	ND	yes	0.90	b-solenoid	121±2	0.066±0.003	2.39±0.08
N226A, N243A	N-ladder	NAB	yes	0.84	b-solenoid	139±6	0.054±0.006	0.470±0.05
N226A, N279A	N-ladder	NAD	yes	—	b-solenoid	97.0±6	0.070±0.01	0.250±0.02
N243A, N262A	N-ladder	NBC	yes	—	b-solenoid	311±4	0.039±0.002	0.700±0.04
N262A, N279A	N-ladder	NCD	yes	0.84	b-solenoid	298±1	0.048±0.003	1.28±0.03
E234A, E265A, E272A, N226A, N243A	salt-bridge, N-ladder	SN-	no	—	stacked b-sheet	—	—	—
K229, K270A, R236A, N262A, N279A	salt-bridge, N-ladder	SN+	no	—	stacked b-sheet	—	—	—

Mutation type refers to the type of structure affected by the mutation. Presence of the 9.4 Å meridional reflection indicates a two-rung structure. Equatorial CC is the correlation coefficient between wt and mutant equators; mutants with no listed CC were too disordered to perform quantitative analysis, so qualitative comparisons are shown in Table 5. Lag time is an empirical parameter representing time before exponential growth and k_{app} is an empirically calculated apparent first order rate constant. Lag time and k_{app} for NAB and NAD are for the second aggregation step. $m_{1/2}$ is the guanidine concentration at the half-denaturation point.

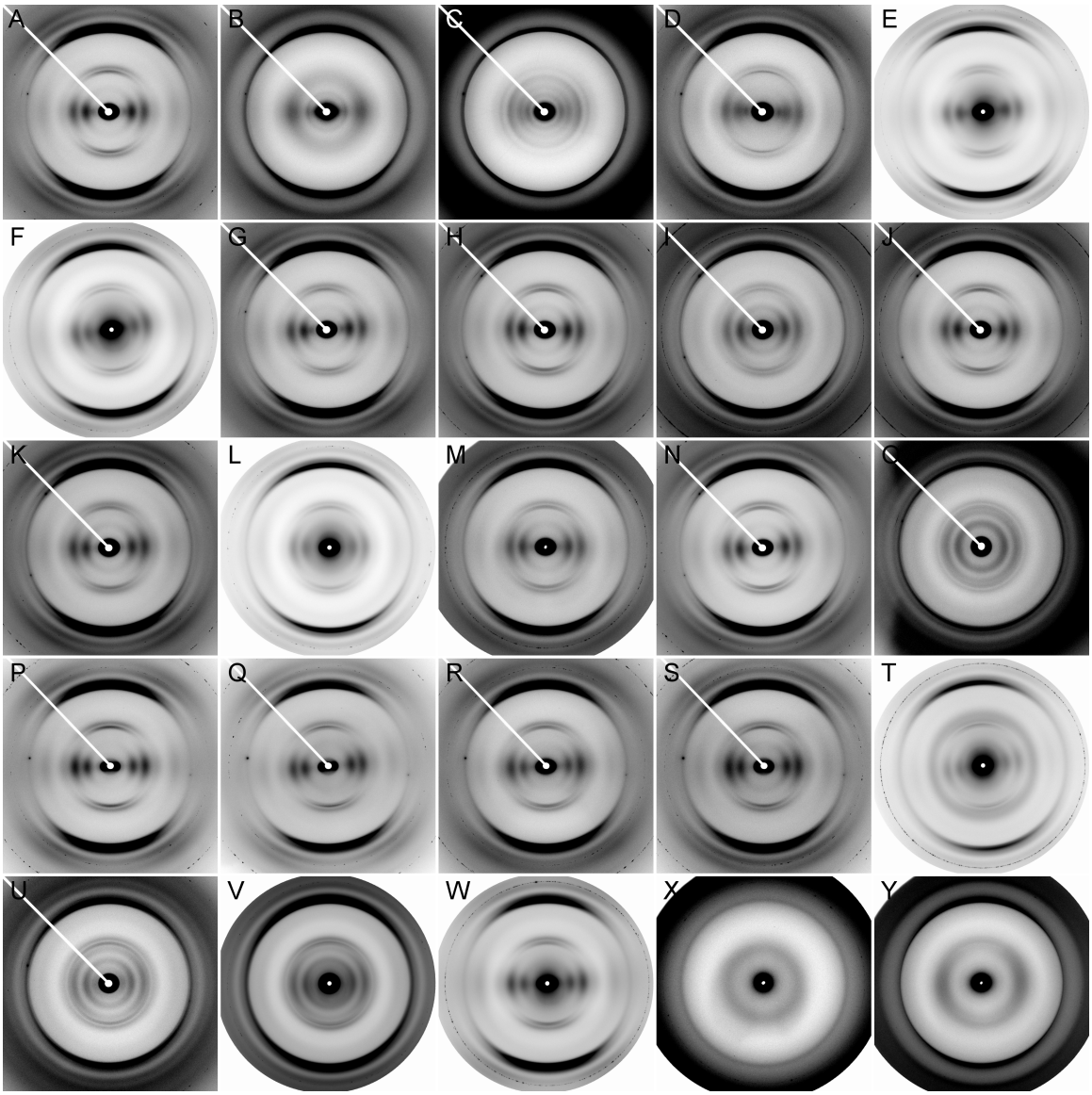

Figure 44: X-ray fiber diffraction from HET-s(218–289) mutants. A) wt, B) RL, C) SL, D) Δ251–253, E) PA, F) PB, G) PAB, H) SA-, I) SB-, J) SC-, K) SABC-, L) SB+, M) SA+, N) SC+, O) SABC+, P) NA, Q) NB, R) NC, S) ND, T) NAB, U) NAD, V) NBC, W) NCD, X) SN-, Y) SN+

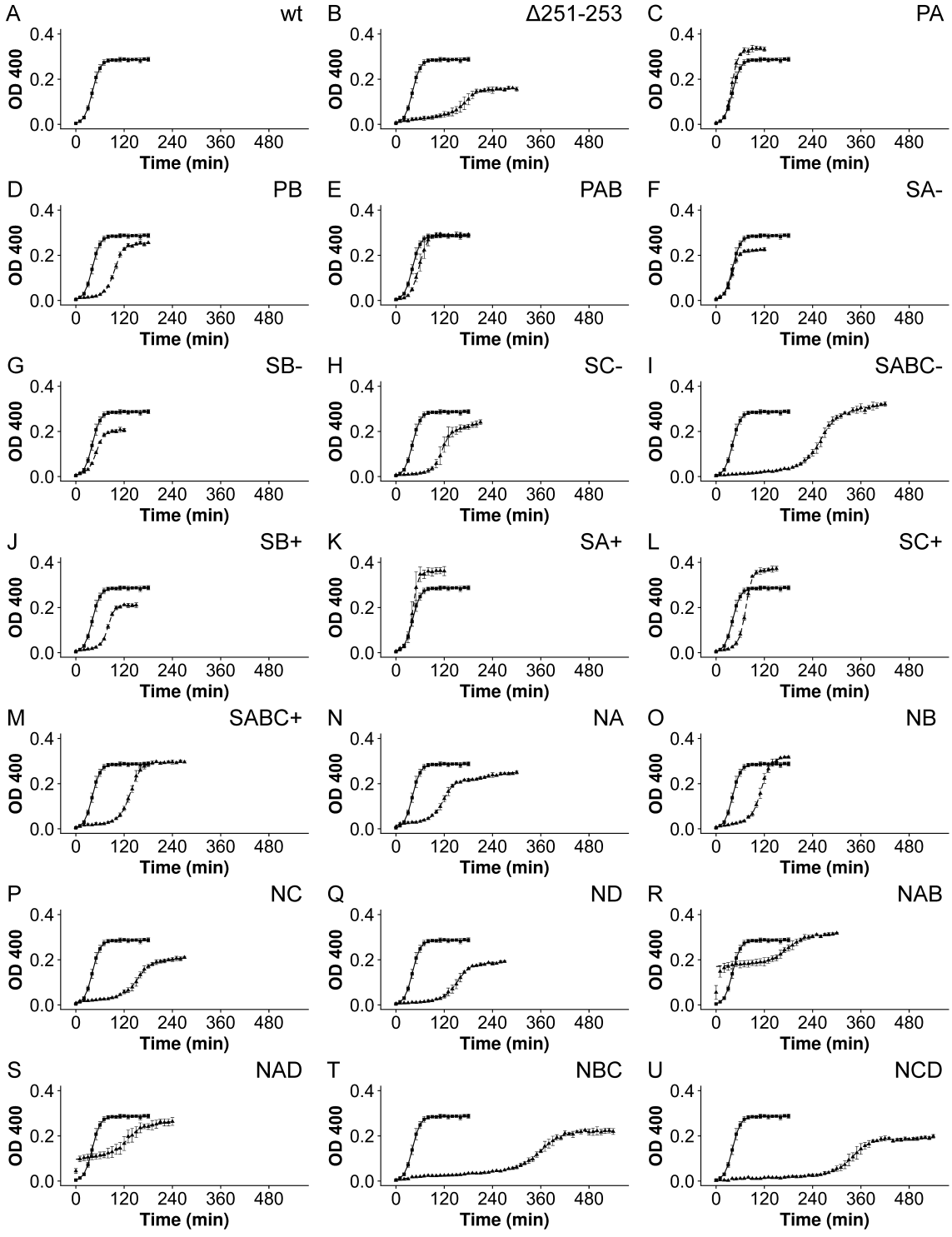

Figure 45: Fibrillization kinetics assays of HET-s(218–289) mutants. A) wt, B) Δ251–253, C) PA, D) PB, E) PAB, F) SA-, G) SB-, H) SC-, I) SABC-, J) SB+, K) SA+, L) SC+, M) SABC+, N) NA, O) NB, P) NC, Q) ND, R) NAB, S) NAD, T) NBC, U) NCD. Points represent averaged data, error bars represent standard devation, and lines indicate fitted curves. Wt is shown as ■ and solid lines, mutants are shown as ▲ and dotted lines.

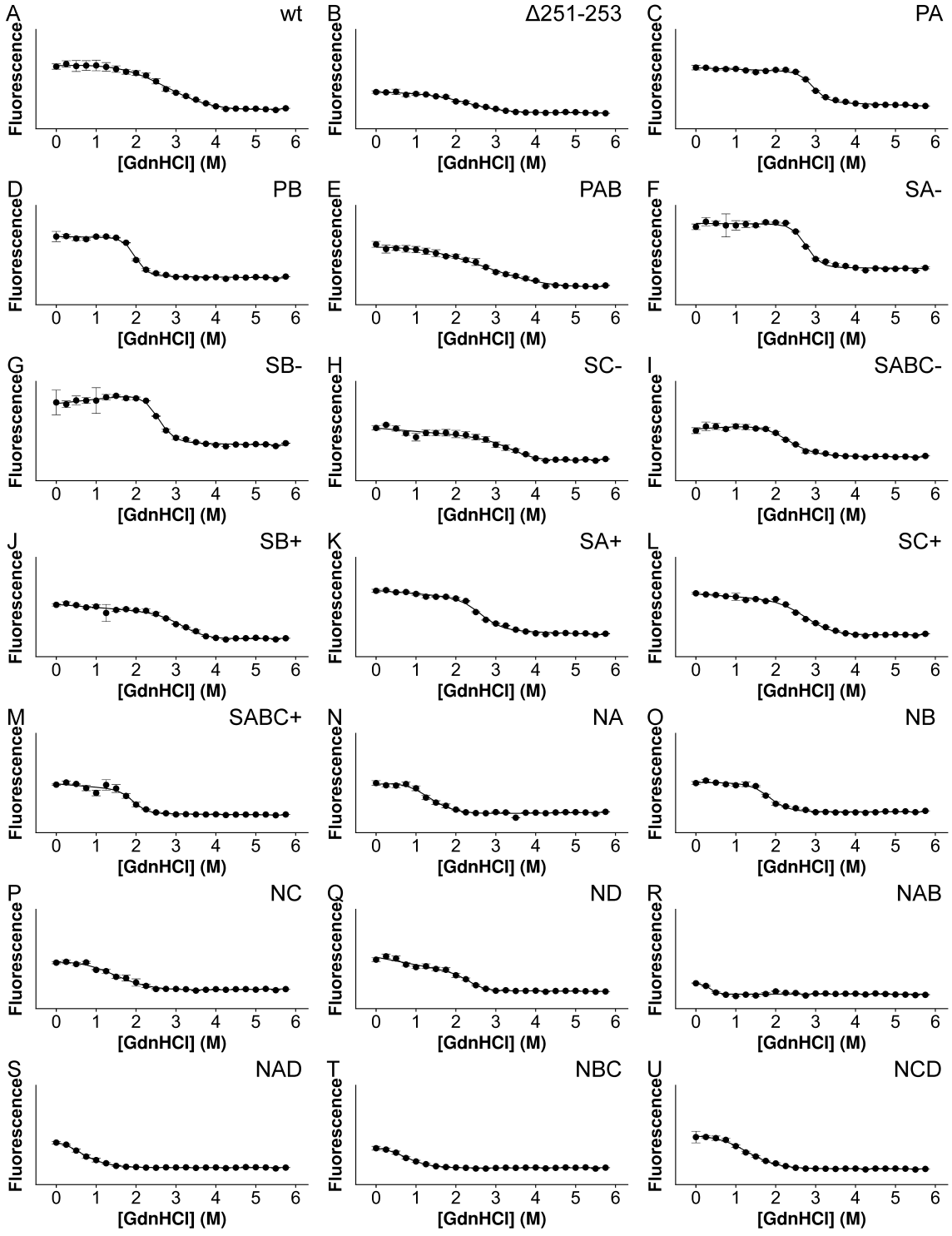

Figure 46: Guanidine denaturation assays of HET-s(218–289) mutants. A) wt, B) Δ251–253, C) PA, D) PB, E) PAB, F) SA-, G) SB-, H) SC-, I) SABC-, J) SB+, K) SA+, L) SC+, M) SABC+, N) NA, O) NB, P) NC, Q) ND, R) NAB, S) NAD, T) NBC, U) NCD. (•) represents averaged data points, error bars represent standard deviation, lines represent fitted curves.

Table 5: d^*-spacings for disoriented fiber diffraction specimens

Mutant	Meridional	Equatorial	Rings
wt	9.47, 8.70, 4.83, 4.70	16.3, 10.6, 5.66	—
SABC+	9.61, 8.68, 4.82, 4.70	16.5, 11.0, 5.67	—
NAD	9.54, 8.52, 4.84, 4.72	16.3, 10.7, 5.71	—
NBC	9.42, 8.64, 4.70	16.1, 10.7, 5.59	—
SN-	—	—	4.45, 9.91
SN+	—	—	4.48, 9.84

$$Y = y_i + m_i x + \frac{y_f + m_f x}{1 + e^{(x-x_0)/\tau}} \tag{V.1}$$

where $y_i + m_i x$ and $y_f + m_f x$ represent the initial and final linear phase. $2x_0 - 2\tau$ is the lag time, that is, where the equation of the initial linear phase intersects with the k_{app}, the empirical rate constant of the exponential phase. k_{app} is $\frac{1}{\tau}$. To compare mutants, lag time and k_{app} were used as empirical estimates of nucleation and fibril extension, respectively.

V.2.2 Guanidine denaturation assays

Guanidine denaturation assays were performed in black non-binding 96-well plates (Greiner, Frickenhausen, Germany). Guanidine concentrations used were from 0 to 5.75 molar in 0.25 M increments over two rows of wells, with each assay performed in triplicate over 6 rows of wells. The remaining two rows of wells were blanks containing no protein, and were used for background subtraction. Wells were prepared by mixing 9 parts concentrated guanidine stock solutions with one part concentrated fibril stock solution to reach final concentrations. Final volume in each well was 100 µL. Final buffer concentration was 50 mM Tris-HCl pH7.5. Final protein concentrations were 10 µM, as determined by BCA assay (Thermo Scientific, Rockville, IL). To ensure equilibrium was reached, plates were sealed and incubated at room temperature for 7 days. 96 well plates were assayed by reading fluorescence using a Perkin Elmer EnSpire (Waltham, MA) with $\lambda_{Ex} = 280$ nm, and

$\lambda_{Em} = 340\,\text{nm}$. Fluorescence readings were background subtracted, averaged, and fit to an empirical equation modified from the equation used for fibrillization kinetics assays:

$$Y = y_i + m_i x + \frac{y_f + m_f x}{1 + e^{-(m_{1/2} - x)/\tau}} \tag{V.2}$$

where y_i, m_i, y_f, and m_f are the initial and final intercept and slope, and $m_{1/2}$ is the half-maximal fluorescence point, the guanidine concentration required for 50 % denaturation. $m_{1/2}$ was used as a convenient measure for comparing the guanidine stability of the mutants.

V.2.3 Calculating errors in fitted parameters

The values used for comparing fibrillization kinetics or stability against guanidine denaturation are for parameters derived from empirical fits of experimental data. In order to compare these values between different mutants, errors must be derived to determine the significance of differences. To derive errors of fitted parameters, a Monte Carlo approach was used (Lambert et al. 2012). Briefly, root mean square errors (RMSE) were calculated between the fitted and experimental data points. Random numbers were generated using the RMSE as the standard deviation, and these numbers were added to the fitted data points to produce virtual data sets. 99 virtual data sets were produced and fitted, and along with the original fit to the experimental data, provided 100 sets of fitted parameters. The standard deviations of these 100 fitted parameters were used as errors.

V.3 Biophysical characterization of site-directed mutants

V.3.1 Mutations to the flexible loop

X-ray fiber diffraction data from the HET-s(218–289) loop mutants RL and SL (Figure 44B, C) agreed poorly with wt diffraction data (Figure 44A,Table 4), but RL data agreed well (CC = 0.84) with the stacked β-sheet model (Figure 36), indicating a stacked β-sheet architecture. SL diffraction showed poor agreement with the stacked β-sheet model (CC = 0.62) and the wt pattern (Figure 44A, Table 4), but good correlation with RL (CC = 0.88). Comparison of equatorial plots (Figure 47) shows that the equators of RL and SL

are almost identical except for an additional intensity minimum indicating that SL is also a stacked β-sheet structure, but with sampling in the pattern, perhaps caused by higher-order fibril structure.

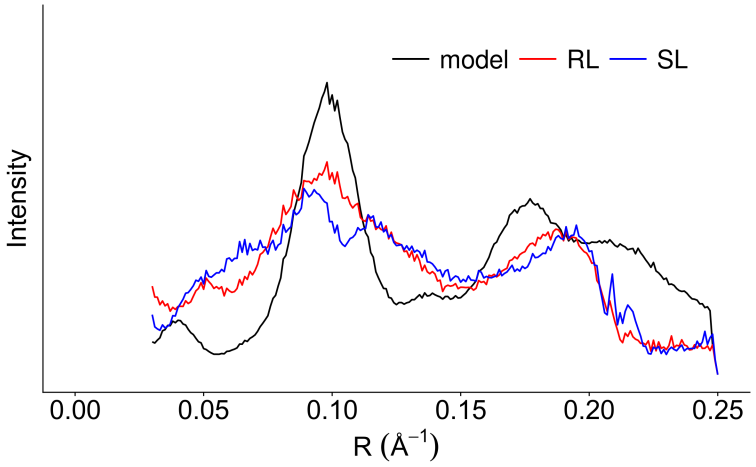

Figure 47: Equatorial plot of scrambled and reversed loop mutants. Black trace shows the calculated stacked β-sheet model data (Figure 36), red shows experimental data from RL, and blue shows experimental data from SL. Resolution range shown is ~33–4 Å (0.03–0.20 Å^{-1}).

In order to determine whether the inability of RL and SL to form β-solenoids was due to barriers to fibril nucleation, we obtained fiber diffraction data from fibrils seeded with HET-s(218–289) wild-type (wt) fibrils (Figure 48). Seeding was performed at a 1:100 molar ratio. Seeded diffraction data for RL showed stacked β-sheet architecture (Figure 48A), but SL exhibited weak diffraction consistent with a two-rung β-solenoid structure (Figure 48B).

The partial loop deletion mutant Δ251–253 exhibited a two-rung β-solenoid diffraction pattern (Figure 44D, Table 4), as was expected given its confirmed *in vivo* infectivity. Kinetics assays showed that fibrillization of Δ251–253 had a much longer lag time and lower k_{app} than wt fibrils (Table 1). Guanidine denaturation assays showed that Δ251–253 had a lower $m_{1/2}$ than wt. These differences suggest that shortening the loop has a particularly large impact on fibril nucleation, as well as a significant effect on growth and stability of fibrils.

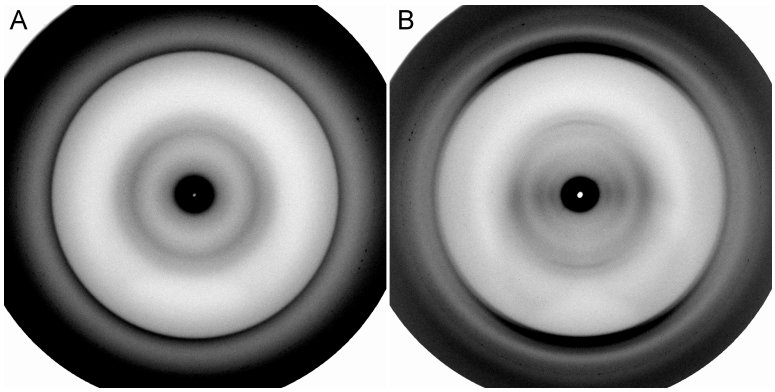

Figure 48: X-ray fiber diffraction from HET-s(218–289) loop mutants seeded with wt fibrils. A) RL, B) SL.

V.3.2 The role of buried polar interactions

Fiber diffraction from HET-s(218–289) buried polar mutants PA, PB, and PAB indicated a two-rung β-solenoid structure (Figure 44E–G, Table 4). The lag time of PA was roughly the same as wt, though k_{app} and $m_{1/2}$ were greater. PB showed a significantly longer lag time and lower $m_{1/2}$ than wt, but the same k_{app}. PAB had the same k_{app} and $m_{1/2}$ as wt as well as a longer lag time, though not as long as PB.

V.3.3 Contribution of salt-bridge mutants

Fiber diffraction from all the single and triple salt-bridge mutants revealed β-solenoid architecture (Figure 44H–O, Table 4). Single mutants all had longer lag times, but k_{app} and $m_{1/2}$ tended to be the same or greater than wt, though SB- and SA+ had lower $m_{1/2}$ values. There was no obvious correlation in kinetics or stability between mutations affecting the same salt-bridge pairs. The triple salt-bridge mutants all showed longer lag times and lower k_{app} and $m_{1/2}$ values than wt or single salt-bridge mutants. SABC- had a much longer lag time and lower k_{app} than SABC+ but a higher $m_{1/2}$. The biophysical differences with respect to wt between the triple mutants and their constituent single mutations were decidedly larger, indicating that the stabilizing and kinetics-enhancing effects of salt-bridges have a cumulative relationship.

V.3.4 The significance of asparagine ladders

Fiber diffraction from single and double asparagine ladder mutants showed the presence of β-solenoid architecture (Figure 44P–W, Table 4). Single asparagine ladder mutants had longer lag times and lower k_{app} values than wt, with NC and ND showing significantly longer lag times and lower k_{app}values than NA and NB (Table 1). The $m_{1/2}$ for each single mutant was lower than wt, but NA, NB, and NC showed $m_{1/2}$ values lower than either triple salt-bridge mutant.

Double asparagine ladder mutants exhibited two types of kinetics curves: a standard two-state curve for NBC and NCD (Figure 45T, U), and an apparent three-state curve for NAB and NAD (Figure 45R, S). The three-state curves have a rapid initial aggregation step, followed by a lag phase, and a subsequent aggregation phase. To characterize the different stages, negative stain EM was performed on mature wt fibrils and on NAB and NAD fibrils at the mid- and final steady-states. Negative stain EM was performed as described in Chapter III.1.2. Mature wt fibrils are characterized by long cable-like aggregates (Figure 49A), while NAB and NAD at 30 mins had disperse fibrils associated with large and small amorphous aggregates (Figure 49B, C). NAB and NAD at 4 hrs had almost no amorphous aggregates and fibrils were laterally organized similarly to wt fibrils (Figure 49D, E). The times between initiation and the second aggregation step of NAB and NAD were much longer than the wt lag time, and k_{app} of the second step for each mutant was also lower than wt (Table 4). The $m_{1/2}$ values for NAB and NAD were the lowest of all the mutants assayed (Table 4). NBC and NCD had the longest lag times and smallest k_{app} values of any mutants studied, and $m_{1/2}$ values lower than all mutants except NAB and NAD (Table 4).

In preparing double asparagine ladder mutants for fiber diffraction using the procedure in Chapter III.1.5, we found that moving fibrils to pH 4 resulted in specimens giving stacked β-sheet diffraction patterns (Figure 50). Diffraction specimens in water from the same fibril preparations, however, exhibited β-solenoid patterns (Figure 44V–W). These results indicate that abrogation of the salt-bridge interactions through low pH, combined with the loss of asparagine ladders, resulted in denaturation and refolding of fibrils. NBC and NCD

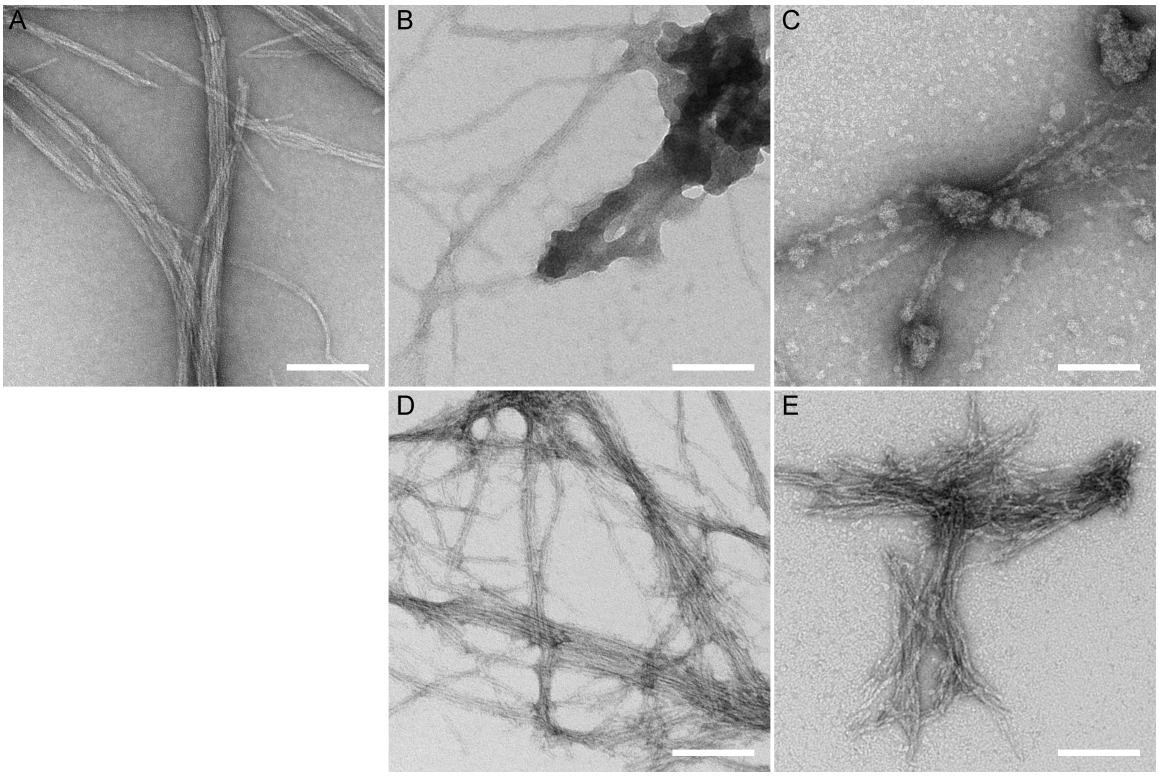

Figure 49: Negative stain EM of HET-s(218–289) wt and double asparagine ladder mutants. A) mature wt. B) NAB and C) NAD at 30 min. D) NAB and E) NAD at 4 hrs. Scale bar = 100nm.

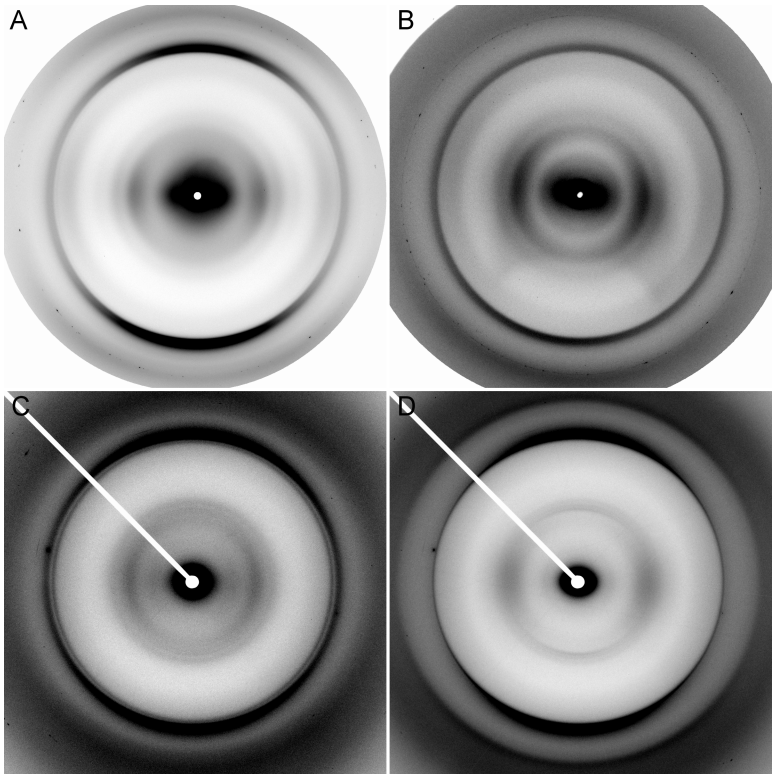

Figure 50: X-ray fiber diffraction from double asparagine-ladder mutants at pH 4.0. A) NAB, B) NAD, C) NBC, D) NCD.

stacked β-sheets showed very faint 9.4 Å meridional reflections (Figure 50C, D), possibly from residual β-solenoid contamination.

V.3.5 Mutants with no surface interactions

X-ray fiber diffraction from the double asparagine ladder / triple salt-bridge mutants SN- and SN+ showed that the fibrils had stacked β-sheet architecture (Figure 44X and Y, Table 5). To determine whether the inability of SN- and SN+ to form β-solenoids was due to barriers to fibril nucleation, SN- and SN+ monomer solutions were seeded with pre-formed wt β-solenoid fibrils. Fiber diffraction data from seeded fibrils (Figure 51C, D) showed similar architectures to unseeded patterns, indicating that the abrogation of β-solenoid formation was not related to nucleation.

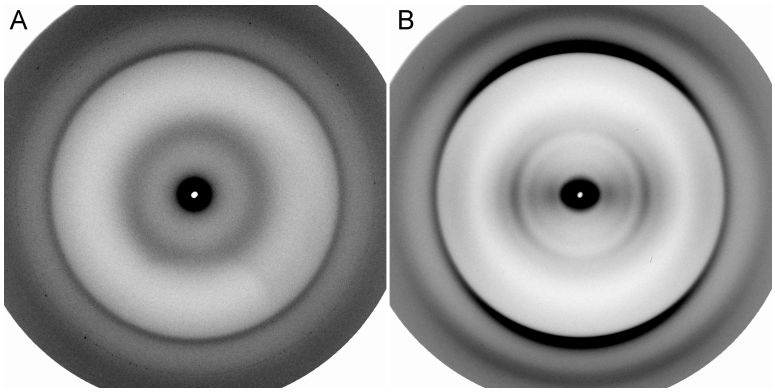

Figure 51: Fiber diffraction from HET-s(218–289) salt-bridge and asparagine ladder mutants seeded with wt fibrils. A) SN- and B) SN+.

V.4 Discussion

V.4.1 General impressions and caveats concerning experimental data

The β-solenoid architecture of HET-s(218–289) proved to be surprisingly robust. Although many of the mutations studied had a significant effect on fibril nucleation, fibrillization rates, and fibril stability, X-ray fiber diffraction showed that in most cases the β-solenoid structure of the wt prion was still formed, rather than a generic stacked β-sheet structure. Only complete scrambling or reversal of the flexible loop connecting the two rungs of the

β-solenoid, or removal of both asparagine ladders as well as all three salt-bridges, perturbed the structure sufficiently to abolish the β-solenoid.

Some caution is appropriate when considering fibrillization kinetics and denaturation results, since the results may depend on the particular approach. Fibrillization kinetics data were fitted to an empirical function, so the fitted parameters are not necessarily directly related to specific events in the fibrillization process. However, they do allow for convenient comparisons and provide qualitative and relative assessments of the mutational impacts, although the precise parameter values may not be directly relatable to other systems. Similar caution must be used in the interpretation of guanidine denaturation results, as HET-s(218–289) denaturation is dependent on the particular chemical used. For example, urea is insufficient for denaturing HET-s(218–289) β-solenoid fibrils and does not prevent the formation of infectious β-solenoids from monomers (Sabaté et al. 2007). This variability with respect to denaturing agent suggests that the relationship between chemical denaturation of HET-s(218–289) and thermodynamic stability may not be a simple one, although denaturation results are nevertheless informative when obtained under comparable conditions.

V.4.2 The effects of site-directed mutagenesis

The only loop mutant that we observed forming β-solenoids was the deletion mutant Δ251–253. The flexible loop joining the two rungs of the β-solenoid structure has previously been shown to tolerate deletions of up to three residues without losing infectivity (Ritter et al. 2005). Our kinetics assays indicate that the loop reduction in Δ251–253 causes reduced fibrillization kinetics, possibly related to the degrees of freedom required to adequately search conformational space and align the two rungs. This deletion also resulted in decreased guanidine stability, which may be due to reduced loop entropy. The stacked β-sheet structure of the RL and SL mutants shows that the amino acid sequence in the loop is important for β-solenoid folding; it may be important for loop flexibility. Residues A247 and A248 are not completely disordered (Wasmer et al. 2008a; Van Melckebeke et al. 2010), and deletion of residues 244–248 results in loss of infectivity (Ritter et al. 2005), suggesting

that these residues are functionally important despite their lack of β-strand structure. The ability of SL to form β-solenoids when seeded indicates that the β-solenoid-abrogating effect of loop scrambling may be kinetic rather than thermodynamic, or at least an effect on fibril nucleation rather than elongation.

Mutations of the buried polar residues T233 and S273 indicate that S273 provides a small benefit to fibrillization rate, but T233 does not. Results from the serine mutant PB demonstrate that T233 interacts unfavorably with the hydrophobic core, but is stabilized by the adjacent S273 in wt. S273 does not appear to need stabilization by T233, probably because it interacts with the adjacent turn (Wasmer et al. 2008a) (Figure 43); the threonine mutant PA is very like wt. The double mutant PAB removes the need for polar compensation of T233; k_{app} and $m_{1/2}$ are identical to wt, but a longer lag time indicates that the buried polar structure is useful during early folding stages.

Salt-bridge mutations affect both folding kinetics and guanidine stability. The non-equivalence of biophysical differences between single mutants, even between partners in the same salt-bridge, indicates complex electrostatic interactions during and after fibrillization. The effective removal of all salt-bridges in the triple mutants shows that these interactions are cumulative, but as with the single mutants, the non-equivalence of the two triple mutants further emphasizes the complexity of the electrostatic interactions.

Single residue asparagine ladder mutations slowed fibrillization and lowered stabilities in guanidine much more than single salt-bridge mutants. The changes observed for ladder partners were not equivalent, indicating the presence of complex polar interactions, as seen in the salt-bridge mutants. We did observe similar kinetics in single mutants affecting the same rung. Double asparagine ladder mutants fell into two types: NBC and NCD exhibited extremely slow but otherwise normal fibrillization kinetics, while NAB and NAD appeared to have a three-state fibrillization process. The mutants with apparent three-state fibrillization had N226A as a common mutation, but the single N226A mutant had typical kinetics. The three-state mutants appear to form stable fibrillization intermediates or off-path products consisting of amorphous aggregates, oligomers, and protofibrils (Figure 49). Mature β-solenoid fibrils of these mutants have particularly low guanidine stabilities.

These observations, taken with fibrillization kinetics data, appear to indicate a flatter energy landscape than that of the two-state double mutants, which have higher guanidine stabilities but much slower fibrillization rates.

Double asparagine mutants refold under acidic conditions to form generic stacked β-sheet amyloids. The equatorial diffraction shows stacked β-sheet architecture, and the absence of 9.4 Å meridional reflections in the diffraction patterns of these amyloids suggests denaturation followed by refolding rather than collapse of the triangular hydrophobic core. These observations indicate that without stabilizing surface interactions, the cross-β hydrogen bonding network of the β-solenoid can be disassembled by adding a net positive charge to the fibril surface. This emphasizes the particular importance of asparagine ladders, as wt β-solenoid is not only stable at pH 4 (Sabaté et al. 2007), but can fibrillize under those conditions (Wan et al. 2013). It is likely that the resultant stacked β-sheet structure allows for repulsive charge compensation, similarly to non-infectious HET-s(218–289) polymorphs fibrillized under acidic conditions (Sabaté et al. 2007; Wan et al. 2013).

V.4.3 Evolutionary conservation of structural features

HET-s has 8 homologs in the *Fusaria* genus, the most studied of which is from *F. graminearum* (Saupe 2011). The *F. graminearum* HET-s(218–289) homolog, FgHET-s(218–289), cross-seeds with *P. anserina* HET-s(218–289), which has been attributed to the fact that they form similar β-solenoid structures (Wasmer et al. 2010). Within the long flexible loop, sequence alignment (Wasmer et al. 2010) shows scattered residues that are identical or similar, which may explain why our RL and SL mutants did not fold into β-solenoids. S273 was highly conserved, while T233 was not, consistent with the accelerated fibrillization kinetics associated with S273 but not T233. While salt-bridges in HET-s(218–289) afforded benefits to fibrillization kinetics and guanidine stability, they were not highly conserved, although some salt-bridge residues in the alignment maintained polar or alternating charge interactions, and there were generally no like-charged pairs. Asparagine ladders are very well conserved, with identical residues in nearly all positions for each homolog. Homology

comparisons suggest that the conserved features necessary for the formation of a two rung β-solenoid are a long flexible loop, alternating polar and non-polar residues to define the buried and exposed surfaces of the hydrophobic core, S273 to stabilize a β-turn in the triangular core structure, and asparagine ladders for the intra- and inter-molecular alignment of rungs.

V.4.4 Implications for other amyloids and prions

Our results suggest some general principles that may be applicable to other prions and amyloids that, like HET-s, do not have any particular amino acid composition bias. In HET-s(218–289), asparagine ladders play a very important role in reproducible folding and fibril stability, even without the extremely high percentages of asparagine and glutamine found in polyQ/N amyloids such as yeast prions (Wickner et al. 1999) and Huntington-related amyloids (Perutz et al. 2002). In HET-s(218–289), asparagine ladders and salt-bridges provide a level of redundancy; β-solenoid formation is not perturbed by mutation of either class of interaction, but only by mutation of both. However, salt-bridges are likely to be found only in amyloids with multi-tier repeats such as β-solenoids and anti-parallel β-sheets. Amide ladders formed by asparagines and glutamines do not require properly matched charge pairs, and as such are more promiscuous in their interactions, as demonstrated by prion formation from scrambled polyQ/N domains (Ross et al. 2004; Ross et al. 2005). The low number of asparagines in HET-s(218–289) may underlie the absence of in vivo polymorphs, whereas functional polyQ/N amyloids such as yeast prions can take on a number of stable strains (Toyama et al. 2007).

It is clear from these results that solvent exposed surface interactions play complex but vital roles in high-fidelity amyloid fibrillization and self-propagation. Our inability to induce β-solenoid formation in the double asparagine ladder / triple salt-bridge mutants SN- and SN+ further emphasizes the necessity for surface interactions, demonstrating that the shape of the triangular hydrophobic core alone is insufficient as a structural template. Computational studies have indicated that these solvent exposed interactions contribute to the high stability of HET-s(218–289) (Lange et al. 2009), and our observation of acidic denaturation of double asparagine mutants suggests that stability is not due to cross-β

hydrogen bonding networks. HET-s(218–289) as a model prion has thus allowed us to elucidate the role of structural features that cannot be probed by short-peptide models (Sawaya et al. 2007). The hydrophobic core of HET-s(218–289) is similar to those found in other β-solenoid proteins (Kajava and Steven 2006) and does not exhibit the extremely tight, interdigitated packing found in steric zippers (Nelson et al. 2005; Sawaya et al. 2007), although the hydrophobic core and solvent exposed surfaces of HET-s(218–289) can be thought of as analogous to the dry and wet steric zipper interfaces.

An inverse relationship between incubation time and conformational stability has been observed for the infectious form of PrP, PrP^{Sc} (Colby et al. 2009). It seems likely, therefore, that pathological prions may have a combination of the structural features studied here to allow for high-fidelity propagation, although not necessarily to the extent that provides the robust redundancy found in HET-s(218–289). Overall, our studies with HET-s(218–289) mutants provide a useful basis for understanding the relative contributions of different structural features for high-fidelity fibrillization and structural propagation, two core properties that define a stable prion strain. Prion structure and self-propagation appear to require an obligatory level of complexity not seen in short amyloid models.

CHAPTER VI

Conclusions

VI.1 Heterogeneous seeding of prions

VI.1.1 Hetergeneous seeding as a mechanism for structural adaptation

The molecular architectures of the HET-s(218–289) polymorphs studied here resemble those of recPrP amyloids of low infectivity (Legname et al. 2004) and highly infectious brain-derived PrP 27–30 (Wille et al. 2009). Fiber diffraction from recPrP amyloid (Wille et al. 2009) showed a characteristic stacked β-sheet pattern, similar to that shown by the stacked β-sheet HET-s(218–289) polymorph. recPrP has a single meridional reflection at 4.8 Å, and an equatorial inter-sheet intensity maximum at 10.5 Å, clearly showing a stacked β-sheet structure. Fiber diffraction from brain-derived PrP 27–30 showed meridional reflections at 9.6 Å, 6.4 Å, and 4.8 Å, consistent with a four β-strand repeat (Wille et al. 2009). Equatorial diffraction showed a series of diffraction maxima, indicating a roughly cylindrical structure. Fiber diffraction of PrP 27–30 showed features consistent with a four-rung β-solenoid model derived from EM reconstructions and comparative modelling (Wille et al. 2002), which is similar to the two-rung β-solenoid structure of HET-s(218–289) (Van Melckebeke et al. 2010).

Concomitant with the similarities in molecular architectures, HET-s(218–289) heterogeneous seeding resembles a model of PrP adaptation. recPrP fibrils do not contain PrP^{Sc} and have very low initial infectivity (Makarava et al. 2011), similar to the low but not incomplete infectivity observed with low pH HET-s(218–289) polymorphs (Sabaté et al. 2007). During serial passaging, recPrP undergoes adaptation to the new host conditions and acquires the biophysical properties of PrP^{Sc} (Wille et al. 2009; Makarava et al. 2011; Makarava et al. 2012b), parallel to the reproduction of homogeneous seeding kinetics following serial passage of heterogeneously seeded HET-s(218–289) fibrils. The similarities between these results suggest that strain adaptation by way of changing molecular structure is a common biophysical feature of prions. Results with HET-s(218–289) show that this phenomenon can

be reproduced under simple experimental conditions, and that the interaction of distinctly different molecular architectures does not need to be facilitated by cofactors. The ability for distinct architectures to interact may indicate that segments of the two conformations share structure. Seeding using degraded HET-s(218–289) further suggests that fragments of shared secondary structure are sufficient for heterogeneous seeding. If this is the case, then despite the significant structural changes possible through heterogeneous seeding, the conformational space that is accessible by the initial seed could still be limited.

While heterogeneous seeding and structural mutation is a useful model for certain speciation phenomena, it is not the sole mechanism of prion strain formation. Isolation of the hyper (HY) and drowsy (DY) prion strains by passage of transmissible mink encephalopathy into Syrian hamsters likely involves heterogeneous seeding together with the presence of multiple prion strains in the original animal (Bessen and Marsh 1992). Initial passages into hamsters resulted in reduced incubation times, consistent with structural adaptation, but on the third passage, the HY and DY strains began to diverge, with subsequent passages leading to lower incubation times until stabilization of each strain. The divergence of HY and DY may have resulted from effective isolation of two variants present in the original mink brain, but the reduction in incubation time, and in particular, the inability of HY to re-infect mink, indicate that structural mutation was present.

VI.1.2 Possible implications for drug-resistant prions

Heterogeneous seeding may be an underlying factor in the drug-resistance mechanisms of certain types of prions. In a recent study by Oelschlegel and Weissmann (2013), 22L prions were propagated in a number of different cell lines with and without swainsonine (swa), an inhibitor of α-mannosidase II that results in misglycosylation of PrP. They found that by serial passage of prions through cell lines in the presence of swa, they could produce swa-dependent (where presence of swa increases infectivity) prions that maintained this property even without swa present, indicating structural mutation of a fold that requires the misglycosylation to propagate efficiently. Other combinations of passaging produced swa-resistant prions that became semi-resistant after passaging without swa, indicating

that the structural mutations compensated for swa, but were otherwise not optimal, and the absence of swa allowed further mutation.

In another study (Berry et al. 2013), RML prions were passaged into mice treated with a therapeutic lead compound, IND24, which resulted in longer survival times of treated mice. Second passage of IND24-treated RML-infected brains resulted in shorter survival times than initial infections, indicating the emergence of drug resistance. However, if IND24-treated RML-infected brains were passaged without IND24 treatment, the third passage resulted in IND24-susceptible prions. The abrupt switching of IND24 resistance suggests that this mode of drug resistance may be related to selection of a resistant strain within the RML inoculum rather than structural mutation.

VI.1.3 Concluding remarks

Heterogeneous seeding and structural mutability appear to be general biophysical phenomena that allow prions to adapt to new environmental conditions. From observations of HET-s(218–289) and PrP, we conclude that heterogeneous seeding can occur despite substantial differences in molecular architecture. However, interaction between heterogeneous structures implies that there is at least some level of similarity present, which may limit the number of conformations that can be arrived at through this mechanism. The interaction of similar structural features also extends to over-simplified model systems, such as short peptide systems, as the ability to elicit biophysical interactions only implies subtle localized structural similarities. This interplay of structural complexity and size has notably been observed in Sup35p, where the full protein shows different secondary structure from that found in the truncated Sup35 NM domain, and neither of them show the secondary structure found in the short peptide GNNQQNY (Luckgei et al. 2013; Nelson et al. 2005). While heterogeneous seeding alone is not sufficient to explain all modes of prion speciation and drug resistance, it is a significant factor that can act in concert with other mechanisms, so understanding its nature is essential to understanding prion propagation.

VI.2 The necessity of structural complexity for self-propagation

VI.2.1 On the definition of a prion

The term prion is derived from the word protein and infectious and was originally coined to describe the protein-based infectious agent found in scrapie (Prusiner 1982). Following the discovery that scrapie and the other TSEs were induced by aberrantly folded forms of PrP, the term prion effectively became synonymous with the TSE-causing agent (Prusiner 1991). However, the prion hypothesis proved to be useful for explaining a number of non-Mendelian genetic elements in yeast (Wickner 1994; Chernoff et al. 1995) and fungi (Coustou et al. 1997), demonstrating that the principle of transmissible alternative protein conformations is extensible beyond diseases of PrP. A useful working definition of prion, from a biophysical and structural perspective, is a self-propagating aberrantly-folded protein aggregate that produces a biological effect. In the case of TSEs this effect is pathological; in *Saccharomyces cerevisiae*, prions manifest as non-Mendelian heritable traits; and in some fungi, prions are used for mating-type recognition.

In vivo, HET-s acts as a functional prion in *Podospora anserina*, and is used for mating-type recognition. In this case the biological effect is a cell-death event when HET-s expressing mating-types interact with the opposite mating-types expressing the non-prion forming homolog HET-S (Saupe 2011). It has been shown that HET-s can take on globular and prion folds (Greenwald et al. 2010), and that the prion fold occurs in 92 % of wild HET-s strains (Debets et al. 2012). These features demonstrate that HET-s is indeed a true prion, and the prion-forming domain HET-s(218–289) has been shown to reproduce these features *in vivo* (Balguerie et al. 2003). As would be expected from the *in vivo* results, the structure of residues 218–289 is virtually identical when taken as a fragment (Van Melckebeke et al. 2010) or within the full-length protein (Wasmer et al. 2009).

In addition to the prion fold, HET-s(218–289) can be folded into "non-infectious" amyloids under acidic conditions (Sabaté et al. 2007). In this case, non-infectious does not signify a complete lack of biological activity, but instead indicates a substantially diminished level of activity. In our hands, HET-s(218–289) fibrillized under certain acidic conditions can proteolyze into fragments (Wan et al. 2012) or remain intact (Wan et al. 2013), depending

on the specific buffer used. In both cases, the resultant amyloids take on a stacked β-sheet architecture. The stacked β-sheet architecture appears to represent a generic low-energy amyloid state that is thought to be accessible to any protein under appropriate conditions. Early fiber diffraction experiments showed that stacked β-sheets could be produced by heat denaturation (Astbury et al. 1935) or super-contraction of coiled-coils (Rudall 1946), indicating that a stacked β-sheet is simply a collapsed protein chain. In terms of intra- and inter-molecular interactions, as well as overall backbone fold, the prion form of HET-s(218–289) has structural complexity similar to other β-solenoids (Kajava and Steven 2006). It appears that the structural complexity of the β-solenoid fold is what makes it a true prion, compared with the low activity of the simple stacked β-sheet amyloid polymorphs. Results from other biologically active amyloids indicate that structural complexity is a general requisite for robust biological activity.

VI.2.2 Requirements for self-propagation

From our mutagenesis studies of HET-s(218–289), we have found that reproducible folding of the two-rung β-solenoid architecture relies on the presence of a flexible loop and solvent-exposed interactions. The flexible loop is capable of sustaining the loss of up to three residues before proper folding is lost (Ritter et al. 2005), but appears to require amino acids at certain positions, as shown by our reversed loop or scrambled loop mutants. The requirements on the loop appear to be related to allowing sufficient freedom for the two rungs to align. The alignment of the rungs, and the subsequent formation of the β-solenoid core, appear to be mediated by the solvent-exposed contacts: the salt-bridges and asparagine ladders. The loss of both of these results in the formation of stacked β-sheets. While these stacked β-sheets may have different structures than those formed at low pH, the similarities in architectures suggest that both represent low-energy states that are accessible under the fibrillization conditions. The need for solvent-exposed interactions, as well as our results showing structural deformation with dehydration, indicate that the solvent exposed surfaces, and not the hydrophobic core, are the important driving factor for formation of the β-solenoid structure. A recent ssNMR structure from the Alzheimer's disease-related

Aβ 1–40 was determined from synthetic and recombinant protein seeded with human brain-derived tissue (Lu et al. 2013). This showed a three-protofilament structure with a solvent-accessible channel down the middle, similar to previous models from completely synthetic protein (McDonald et al. 2012), though the the β-strand structure in the synthetic amyloid is much simpler than the brain derived structure. While the effects of this channel have not yet been studied in detail, that this particular structure propagated from brain-tissue versus the many other non-pore-containing structures seen with synthetic Aβ (Petkova et al. 2006; Sachse et al. 2008; Meinhardt et al. 2009; Bertini et al. 2011) suggest that the self-replicating activity of pathological Aβ may require this more complex structure.

Another factor which appears to play a significant role in self-propagation is the size of the amyloid subunits. In our experiments with HET-s(218–289), we found that degraded fragments were able to act as heterogeneous seeds, but were inherently incapable of producing a β-solenoid structure. Similar results have been seen with the yeast prion Sup35, which can form amyloids from 7 residue fragments (Nelson et al. 2005) that do not share secondary structural elements with amyloid formed from the full protein (Luckgei et al. 2013). Some parallels can also be drawn with different sized constructs derived from mammalian PrP. PrP fragments as small as 6 residues can form amyloid fibrils (Sawaya et al. 2007), but the shortest toxic amyloid found is 21 residues (Forloni et al. 1993). This 21 residue fragment, PrP 106–126 has been shown to form parallel β-sheet steric-zipper-like fibrils by ssNMR (Walsh et al. 2009), though our own fiber diffraction experiments suggest a different anti-parallel β-sheet structure. The mode of PrP 106–126 toxicity appears to be PrP dependent, but it only causes neurotoxicity and does not induce a true TSE state, indicating that it is incapable of self-propagation (Fioriti et al. 2005). A larger 55 residue fragment containing a mutation (P102L) linked to the familial prion disease GSS was found to induce GSS-like symptoms in transgenic mice containing this mutation (Kaneko et al. 2000). Wild-type PrP fragments that can reproduce disease-states have tended to correspond to the proteinase K resistant core, PrP 27–30, which approximately corresponds to residues 89–231 (Legname et al. 2004), though these prions tend to require several passages through animals to reproduce highly-infectious prions. However, these large constructs appear to have substantial

heterogeneity when fibrillized *in vitro*, leading to the ability to propagate a diverse range of stable strains (Colby et al. 2009). While methods for producing highly-infective prions *de novo* have been published (Castilla et al. 2005; Wang et al. 2010), they have been difficult to reproduce in other labs. Taken together, these results indicate that biological effects can be caused by fragments much shorter than those required to fully reproduce disease-states. In the case of PrP, larger fragments have more accessible stable amyloid folds, leading to significant heterogeneity in *in vitro* specimens. Emergence of highly-infectious prions requires selection by passaging through animals, possibly through a mechanism of heterogeneous seeding. Despite this, the ability to produce stable strains of varying infectivity shows that these larger constructs are able to form a diverse array of self-propagating structures.

Overall, our results have shown that HET-s(218–289) has been a useful model system for studying the general mechanisms of prion propagation. Our results indicate that structural complexity, in terms of amyloid architecture, intra- and inter-subunit interactions, and protein length, is required for robust self-propagation. While smaller or less complex amyloids can induce some forms of biological activity, such as heterogeneous seeding, they do not reproduce the same effects as the complex prion folds.

REFERENCES

(1755). *Journal of the House of Commons* **27**: 87.

Adams, D. H. and Caspary, E. A. (1967). "Nature of the scrapie virus". *British Medical Journal* **3**:5558, 173.

Aguzzi, A. (2009). "Cell biology: Beyond the prion principle". *Nature* **459**:7249, 924–925.

Alper, T., Haig, D., and Clarke, M. (1966). "The exceptionally small size of the scrapie agent". *Biochemical and Biophysical Research Communications* **22**:3, 278–284.

Alper, T., Cramp, W. A., Haig, D. A., and Clarke, M. C. (1967). "Does the agent of scrapie replicate without nucleic acid?" *Nature* **214**:5090, 764–766.

Alper, T., Haig, D. A., and Clarke, M. C. (1978). "The scrapie agent: evidence against its dependence for replication on intrinsic nucleic acid". *Journal of General Virology* **41**:3, 503–516.

Alpers, M. (1970). "III. Kuru in New Guinea: Its changing pattern and etiologic elucidation". *The American Journal of Tropical Medicine and Hygiene* **19**:1, 133–137.

Arnott, S. (2006). "Historical article: DNA polymorphism and the early history of the double helix". *Trends in Biochemical Sciences* **31**:6, 349–354.

Arnott, S., Scott, W. E., Rees, D. A., and McNab, C. G. A. (1974). "i-Carrageenan: Molecular structure and packing of polysaccharide double helices in oriented fibres of divalent cation salts". *Journal of Molecular Biology* **90**:2, 253–267.

Ashe, K. H. and Aguzzi, A. (2013). "Prions, prionoids and pathogenic proteins in Alzheimer disease". *Prion* **7**:1, 55–59.

Astbury, W. T., Dickinson, S., and Bailey, K. (1935). "The X-ray interpretation of denaturation and the structure of the seed globulins". *Biochemical Journal* **29**:10, 2351–2360.

Bahmanyar, S., Williams, E. S., Johnson, F. B., Young, S., and Gajdusek, D. C. (1985). "Amyloid plaques in spongiform encephalopathy of mule deer". *Journal of Comparative Pathology* **95**:1, 1–5.

Balguerie, A., Reis, S. D., Ritter, C., Chaignepain, S., Coulary-Salin, B., Forge, V., Bathany, K., Lascu, I., Schmitter, J.-M., Riek, R., and Saupe, S. J. (2003). "Domain organization

and structure-function relationship of the HET-s prion protein of Podospora anserina". *EMBO Journal* **22**:9, 2071–2081.

Barlow, R. and Rennie, J. (1970). "Transmission experiments with a scrapie-like encephalopathy of mink". *Journal of Comparative Pathology* **80**:1, 75–79.

Barnhart, M. M. and Chapman, M. R. (2006). "Curli biogenesis and function". *Annual Review of Microbiology* **60**:1, 131–147.

Baskakov, I. V. (2004). "Autocatalytic conversion of recombinant prion proteins displays a species barrier". *The Journal of Biological Chemistry* **279**:9, 7671–7677.

Baskakov, I. V., Legname, G., Baldwin, M. A., Prusiner, S. B., and Cohen, F. E. (2002). "Pathway complexity of prion protein assembly into amyloid". *The Journal of Biological Chemistry* **277**:24, 21140–21148.

Basler, K., Oesch, B., Scott, M., Westaway, D., Wälchli, M., Groth, D., McKinley, M., Prusiner, S., and Weissmann, C. (1986). "Scrapie and cellular PrP isoforms are encoded by the same chromosomal gene". *Cell* **46**:3, 417–428.

Beese, L., Stubbs, G., and Cohen, C. (1987). "Microtubule structure at 18 Å resolution". *Journal of Molecular Biology* **194**:2, 257–264.

Beijerinck, M. W. (1898). "Ueber ein Contagium vivum fluidum als Ursache der Fleckenkrankheit der Tabaksblatter". *Verhandelingen der Koninklyke akademie van Wettenschappen te Amsterdam* **65**:2, 3–21.

Beijerinck, M. W. (1942). "Concerning a contagium vivum fluidium as a cause of the spot-disease of tobacco leaves". *Phytopathological Classics*. Vol. 7. Translated by J. Johnson. Originally published in 1898. St. Paul, MN: American Phytopathological Society, 33–52.

Bendheim, P. E., Barry, R. A., DeArmond, S. J., Stites, D. P., and Prusiner, S. B. (1984). "Antibodies to a scrapie prion protein". *Nature* **310**:5976, 418–421.

Benkemoun, L., Ness, F., Sabaté, R., Ceschin, J., Breton, A., Clavé, C., and Saupe, S. J. (2011). "Two structurally similar fungal prions efficiently cross-seed in vivo but form distinct polymers when coexpressed". *Molecular Microbiology* **82**:6, 1392–1405.

Berry, D. B., Lu, D., Geva, M., Watts, J. C., Bhardwaj, S., Oehler, A., Renslo, A. R., DeArmond, S. J., Prusiner, S. B., and Giles, K. (2013). "Drug resistance confounding

prion therapeutics". *Proceedings of the National Academy of Sciences of the United States of America*, doi: 10.1073/pnas.1317164110.

Bertini, I., Gonnelli, L., Luchinat, C., Mao, J., and Nesi, A. (2011). "A new structural model of Aβ40 fibrils". *Journal of the American Chemical Society* **133**:40, 16013–16022.

Besnoit, C. (1899). "La tremblante ou nevrite peripherique enzootique du mouton". *Revue Vétérinaire* **24**: 265–277.

Besnoit, C. and Morel, C. (1898). "Note sur les lésions nerveuses de la tremblante du mouton". *Revue Vétérinaire* **23**: 397–400.

Bessen, R. A. and Marsh, R. F. (1992). "Identification of two biologically distinct strains of transmissible mink encephalopathy in hamsters". *Journal of General Virology* **73**:2, 329–334.

Bian, W., Wang, H., McCullough, I., and Stubbs, G. (2006). "WCEN: a computer program for initial processing of fiber diffraction patterns". *Journal of Applied Crystallography* **39**:5, 752–756.

Bockman, J. M., Kingsbury, D. T., McKinley, M. P., Bendheim, P. E., and Prusiner, S. B. (1985). "Creutzfeldt–Jakob disease prion proteins in human brains". *New England Journal of Medicine* **312**:2, 73–78.

Bolton, D. C., McKinley, M. P., and Prusiner, S. B. (1982). "Identification of a protein that purifies with the scrapie prion". *Science* **218**:4579, 1309–1311.

Bonar, L, Cohen, A. S., and Skinner, M. M. (1969). "Characterization of the amyloid fibril as a cross-β protein". *Proceedings of the Society for Experimental Biology and Medicine* **131**:4, 1373–1375.

Bram, A., Brändén, C. I., Craig, C., Snigireva, I., and Riekel, C. (1997). "X-ray diffraction from single fibres of spider silk". *Journal of Applied Crystallography* **30**:3, 390–392.

Burger, D and Hartsough, G. R. (1965). "Encephalopathy of mink. II. Experimental and natural transmission". *The Journal of Infectious Diseases* **115**:4, 393–399.

Cantor, C. R. and Schimmel, P. R. (1980). *Biophysical Chemistry: Part II: Technqiues for the study of biological structure and function.* San Francisco: W.H. Freeman and Company.

Castilla, J., Saá, P., Hetz, C., and Soto, C. (2005). "*In vitro* generation of infectious scrapie prions". *Cell* **121**:2, 195–206.

Chandler, R. L. (1963). "Experimental scrapie in the mouse". *Research in Veterinary Science* **4**: 276–285.

Chandler, R. (1961). "Encephelopathy in mice produced by inoculation with scrapie brain material". *The Lancet* **277**:7191, 1378–1379.

Chandrasekaran, R. and Stubbs, G. (2012). "Fibre diffraction". *International Tables for Crystallography Volume F: Crystallography of biological macromolecules*. Ed. by E. Arnold, D. M. Himmel, and M. G. Rossmann. International Tables for Crystallography F. John Wiley & Sons, Ltd, 583–592.

Changeux, J.-P., Thiery, J., Tung, Y., and Kittel, C. (1967). "On the cooperativity of biological membranes". *Proceedings of the National Academy of Sciences of the United States of America* **57**:2, 335–341.

Chernoff, Y. O., Lindquist, S. L., Ono, B., Inge-Vechtomov, S. G., and Liebman, S. W. (1995). "Role of the chaperone protein Hsp104 in propagation of the yeast prion-like factor [psi+]". *Science* **268**:5212, 880–884.

Chiti, F. and Dobson, C. M. (2006). "Protein misfolding, functional amyloid, and human disease". *Annual Review of Biochemistry* **75**:1, 333–366.

Cochran, W., Crick, F. H., and Vand, V. (1952). "The structure of synthetic polypeptides. I. The transform of atoms on a helix". *Acta Crystallographica* **5**:5, 581–586.

Cohen, A. S. (1967a). "Amyloidosis". *New England Journal of Medicine* **277**:10, 522–530.

Cohen, A. S. (1967b). "Amyloidosis". *New England Journal of Medicine* **277**:11, 574–583.

Cohen, A. S. (1967c). "Amyloidosis". *New England Journal of Medicine* **277**:12, 628–638.

Cohen, A. S. (1986). "General introduction and a brief history of amyloidosis". *Amyloidosis*. Nijhoff, Dordrecht: Springer, 3–19.

Cohen, A. S. and Calkins, E. (1959). "Electron microscopic observations on a fibrous component in amyloid of diverse origins". *Nature* **183**:4669, 1202–1203.

Cohen, S. I. A., Linse, S., Luheshi, L. M., Hellstrand, E., White, D. A., Rajah, L., Otzen, D. E., Vendruscolo, M., Dobson, C. M., and Knowles, T. P. J. (2013). "Proliferation of

amyloid-β42 aggregates occurs through a secondary nucleation mechanism". *Proceedings of the National Academy of Sciences of the United States of America* **110**:24, 9758–9763.

Colby, D. W., Giles, K., Legname, G., Wille, H., Baskakov, I. V., DeArmond, S. J., and Prusiner, S. B. (2009). "Design and construction of diverse mammalian prion strains". *Proceedings of the National Academy of Sciences of the United States of America* **106**:48, 20417–20422.

Costa, P. P., Figueira, A. S., and Bravo, F. R. (1978). "Amyloid fibril protein related to prealbumin in familial amyloidotic polyneuropathy." *Proceedings of the National Academy of Sciences of the United States of America* **75**:9, 4499–4503.

Coustou, V., Deleu, C., Saupe, S., and Begueret, J. (1997). "The protein product of the het-s heterokaryon incompatibility gene of the fungus Podospora anserina behaves as a prion analog". *Proceedings of the National Academy of Sciences of the United States of America* **94**:18, 9773–9778.

Cuillé, J. and Chelle, P.-L. (1936). "La maladie dite tremblante du mouton est-elle inoculable". *Comptes Rendus de l'Academie des Sciences* **203**: 1552–1554.

Cuillé, J. and Chelle, P.-L. (1938a). "Le tremblante du mouton est bien inoculable". *Comptes rendus hebdomadaires des séances de l'Académie des Sciences* **206**: 78–79.

Cuillé, J. and Chelle, P.-L. (1938b). "La tremblante du mouton est-elle déterminée par un virus filtrable?" *Comptes rendus hebdomadaires des séances de l'Académie des Sciences* **206**: 1687–1688.

Cuillé, J. and Chelle, P.-L. (1939). "Transmission expérimentale de la tremblante à la chèvre". *Comptes rendus hebdomadaires des séances de l'Académie des Sciences* **208**: 1058–1060.

Debets, A. J. M., Dalstra, H. J. P., Slakhorst, M., Koopmanschap, B., Hoekstra, R. F., and Saupe, S. J. (2012). "High natural prevalence of a fungal prion". *Proceedings of the National Academy of Sciences of the United States of America* **109**:26, 10432–10437.

Diener, T. O. (1971). "Potato spindle tuber "virus": IV. A replicating, low molecular weight RNA". *Virology* **45**:2, 411–428.

Diener, T. O. (1972). "Is the scrapie agent a viroid?" *Nature* **235**:59, 218–219.

Divry, P. and Florkin, M. (1927). “Sur les proprietes optiques de l’amyloide”. *Comptes rendus des séances de la Société de biologie et de ses filiales* **97**: 1808–1810.

Eanes, E. D. and Glenner, G. G. (1968). “X-ray diffraction studies on amyloid filaments”. *Journal of Histochemistry and Cytochemistry* **16**:11, 673–677.

Eckroade, R. J., Zu Rhein, G. M., Marsh, R. F., and Hanson, R. P. (1970). “Transmissible mink encephalopathy: experimental transmission to the squirrel monkey”. *Science* **169**:3950, 1088–1090.

Fast, C. and Groschup, M. H. (2013). “Classical and atypical scrapie in sheep and goats”. *Prions and Diseases*. Ed. by W.-Q. Zou and P. Gambetti. Springer New York, 15–44.

Field, E. J. (1966). “Transmission experiments with multiple sclerosis: an interim report.” *British Medical Journal* **2**:5513, 564–565.

Field, E. J., Farmer, F., Caspary, E. A., and Joyce, G. (1969). “Susceptibility of scrapie agent to ionizing radiation”. *Nature* **222**:5188, 90–91.

Fioriti, L., Quaglio, E., Massignan, T., Colombo, L., Stewart, R. S., Salmona, M., Harris, D. A., Forloni, G., and Chiesa, R. (2005). “The neurotoxicity of prion protein (PrP) peptide 106–126 is independent of the expression level of PrP and is not mediated by abnormal PrP species”. *Molecular and Cellular Neuroscience* **28**:1, 165–176.

Forloni, G., Angeretti, N., Chiesa, R., Monzani, E., Salmona, M., Bugiani, O., and Tagliavini, F. (1993). “Neurotoxicity of a prion protein fragment”. *Nature* **362**:6420, 543–546.

Franklin, R. E. and Gosling, R. G. (1953). “The structure of sodium thymonucleate fibres. I. The influence of water content”. *Acta Crystallographica* **6**:8, 673–677.

Franklin, R. E. and Klug, A. (1955). “The splitting of layer lines in X-ray fibre diagrams of helical structures: application to tobacco mosaic virus”. *Acta Crystallographica* **8**:12, 777–780.

Fraser, R. D. B., Macrae, T. P., Miller, A., and Rowlands, R. J. (1976). “Digital processing of fibre diffraction patterns”. *Journal of Applied Crystallography* **9**:2, 81–94.

Friedreich, P. D. N. and Kekulé, P. D. A. (1859). “Zur Amyloidfrage”. *Archiv für pathologische Anatomie und Physiologie und für klinische Medicin* **16**:1-2, 50–65.

Frost, B. and Diamond, M. I. (2010). "Prion-like mechanisms in neurodegenerative diseases". *Nature Reviews Neuroscience* **11**:3, 155–159.

Gaiger, S. (1924). "Scrapie". *Journal of Comparative Pathology and Therapeutics* **37**: 259–277.

Gajdusek, D. C. (1963). "Kuru". *Transactions of the Royal Society of Tropical Medicine and Hygiene* **57**: 151–169.

Gajdusek, D. C. (1977). "Unconventional viruses and the origin and disappearance of kuru". *Science* **197**:4307, 943–960.

Gajdusek, D. C. and Gibbs, C. J. (1964). "Attempts to demonstrate a transmissible agent in kuru, amyotrophic lateral sclerosis, and other sub-acute and chronic nervous system degenerations of man". *Nature* **204**:4955, 257–259.

Gajdusek, D. C. and Gibbs, C. J. (1971). "Transmission of two subacute spongiform encephalopathies of man (kuru and Creutzfeldt–Jakob disease) to new world monkeys". *Nature* **230**:5296, 588–591.

Gajdusek, D. C. and Zigas, V (1957). "Degenerative disease of the central nervous system in New Guinea; the endemic occurrence of kuru in the native population". *The New England Journal of Medicine* **257**:20, 974–978.

Gajdusek, D. C. and Zigas, V (1959). "Kuru: Clinical, pathological and epidemiological study of an acute progressive degenerative disease of the central nervous system among natives of the Eastern Highlands of New Guinea". *The American Journal of Medicine* **26**:3, 442–469.

Gajdusek, D. C., Gibbs, C. J., and Alpers, M. (1966). "Experimental transmission of a kuru-like syndrome to chimpanzees". *Nature* **209**:5025, 794–796.

Gajdusek, D. C., Gibbs, C. J., and Alpers, M. (1967). "Transmission and passage of experimental 'kuru' to chimpanzees". *Science* **155**:3759, 212–214.

Gajdusek, D. C., Gibbs, C. J., Asher, D. M., and David, E. (1968). "Transmission of experimental kuru to the spider monkey (Ateles geoffreyi)". *Science* **162**:3854, 693–694.

Geddes, A. J., Parker, K. D., Atkins, E. D., and Beighton, E (1968). ""Cross-β" conformation in proteins". *Journal of Molecular Biology* **32**:2, 343–358.

Gibbons, R. A. and Hunter, G. D. (1967). "Nature of the scrapie agent". *Nature* **215**:5105, 1041–1043.

Gibbs, C. J., Gajdusek, D. C., Asher, D. M., Alpers, M. P., Beck, E., Daniel, P. M., and Matthews, W. B. (1968). "Creutzfeldt-Jakob disease (spongiform encephalopathy): transmission to the chimpanzee". *Science* **161**:3839, 388–389.

Gibbs, C. J., Gajdusek, D. C., and Latarjet, R. (1978). "Unusual resistance to ionizing radiation of the viruses of kuru, Creutzfeldt-Jakob disease, and scrapie". *Proceedings of the National Academy of Sciences* **75**:12, 6268–6270.

Gibbs, C. J., Joy, A., Heffner, R., Franko, M., Miyazaki, M., Asher, D. M., Parisi, J. E., Brown, P. W., and Gajdusek, D. C. (1985). "Clinical and pathological features and laboratory confirmation of Creutzfeldt–Jakob disease in a recipient of pituitary-derived human growth hormone". *New England Journal of Medicine* **313**:12, 734–738.

Glabe, C. G. (2008). "Structural classification of toxic amyloid oligomers". *Journal of Biological Chemistry* **283**:44, 29639–29643.

Glasse, R. (1967). "Cannibalism in the Kuru region of New Guinea". *Transactions of the New York Academy of Sciences* **29**:6 Series II, 748–754.

Glenner, G. G. (1980a). "Amyloid deposits and amyloidosis. The beta-fibrilloses (first of two parts)". *The New England journal of medicine* **302**:23, 1283–1292.

Glenner, G. G. (1980b). "Amyloid Deposits and Amyloidosis The beta-fibrilloses (second of two parts)". *New England Journal of Medicine* **302**:23, 1283–1292.

Glenner, G. G. (1988). "Alzheimer's disease: Its proteins and genes". *Cell* **52**:3, 307–308.

Glenner, G. G., Harbaugh, J., Ohms, J. I., Harada, M., and Cuatrecasas, P. (1970). "An amyloid protein: The amino-terminal variable fragment of an immunoglobulin light chain". *Biochemical and Biophysical Research Communications* **41**:5, 1287–1289.

Glenner, G. G., Eanes, E. D., Bladen, H. A., Linke, R. P., and Termine, J. D. (1974). "β-pleated sheet fibrils. A comparison of native amyloid with synthetic protein fibrils." *Journal of Histochemistry and Cytochemistry* **22**:12, 1141–1158.

Gonzalez, A., Nave, C., and Marvin, D. A. (1995). "Pf1 filamentous bacteriophage: refinement of a molecular model by simulated annealing using 3.3 Å resolution X-ray fibre

diffraction data". *Acta Crystallographica Section D Biological Crystallography* **51**:5, 792–804.

Gordon, W. S. (1946). "Advances in veterinary research". *The Veterinary Record* **58**:47, 516–525.

Govaerts, C., Wille, H., Prusiner, S. B., and Cohen, F. E. (2004). "Evidence for assembly of prions with left-handed β-helices into trimers". *Proceedings of the National Academy of Sciences of the United States of America* **101**:22, 8342–8347.

Greenwald, J., Buhtz, C., Ritter, C., Kwiatkowski, W., Choe, S., Maddelein, M.-L., Ness, F., Cescau, S., Soragni, A., Leitz, D., Saupe, S. J., and Riek, R. (2010). "The Mechanism of Prion Inhibition by HET-S". *Molecular Cell* **38**:6, 889–899.

Gregory, J. and Holmes, K. (1965). "Methods of preparing orientated tobacco mosaic virus sols for X-ray diffraction". *Journal of Molecular Biology* **13**:3, 796–801.

Griffith, J. S. (1967). "Nature of the scrapie agent: self-replication and scrapie". *Nature* **215**:5105, 1043–1044.

Guiroy, D. C., Williams, E. S., Yanagihara, R., and Gajdusek, D. C. (1991). "Immunolocalization of scrapie amyloid (PrP27-30) in chronic wasting disease of Rocky Mountain elk and hybrids of captive mule deer and white-tailed deer". *Neuroscience Letters* **126**:2, 195–198.

Guo, J. L. and Lee, V. M.-Y. (2011). "Seeding of normal tau by pathological tau conformers drives pathogenesis of Alzheimer-like tangles". *Journal of Biological Chemistry* **286**:17, 15317–15331.

Haass, C. and Selkoe, D. J. (2007). "Soluble protein oligomers in neurodegeneration: lessons from the Alzheimer's amyloid β-peptide". *Nature Reviews Molecular Cell Biology* **8**:2, 101–112.

Hadlow, W. J. (1959). "Scrapie and kuru". *The Lancet* **274**:7097, 289–290.

Halfmann, R., Jarosz, D. F., Jones, S. K., Chang, A., Lancaster, A. K., and Lindquist, S. (2012). "Prions are a common mechanism for phenotypic inheritance in wild yeasts". *Nature* **482**:7385, 363–368.

Hardy, J. and Allsop, D. (1991). "Amyloid deposition as the central event in the aetiology of Alzheimer's disease". *Trends in Pharmacological Sciences* **12**: 383–388.

Hardy, J. A. and Higgins, G. A. (1992). "Alzheimer's disease: the amyloid cascade hypothesis". *Science* **256**:5054, 184–185.

Hartsough, G. R. and Burger, D (1965). "Encephalopathy of mink. I. Epizootiologic and clinical observations". *The Journal of Infectious Diseases* **115**:4, 387–392.

Hetz, C., Maundrell, K., and Soto, C. (2003). "Is loss of function of the prion protein the cause of prion disorders?" *Trends in Molecular Medicine* **9**:6, 237–243.

Holmes, D., Lancaster, A., Lindquist, S., and Halfmann, R. (2013). "Heritable remodeling of yeast multicellularity by an environmentally responsive prion". *Cell* **153**:1, 153–165.

Holmes, K. C. and Barrington Leigh, J. (1974). "The effect of disorientation on the intensity distribution of non-crystalline fibres. I. Theory". *Acta Crystallographica Section A Foundations of Crystallography* **30**:5, 635–638.

Holmes, K. C., Popp, D., Gebhard, W., and Kabsch, W. (1990). "Atomic model of the actin filament". *Nature* **347**:6288, 44–49.

Hsiao, K, Baker, H. F., Crow, T. J., Poulter, M, Owen, F, Terwilliger, J. D., Westaway, D, Ott, J, and Prusiner, S. B. (1989). "Linkage of a prion protein missense variant to Gerstmann-Sträussler syndrome". *Nature* **338**:6213, 342–345.

Hunter, G. D. (1972). "Scrapie: A prototype slow infection". *Journal of Infectious Diseases* **125**:4, 427–440.

Hunter, G. D. and Millson, G. C. (1964). "Studies on the heat stability and chromatographic behaviour of the scrapie agent". *Journal of General Microbiology* **37**: 251–258.

Hunter, G. D. and Millson, G. C. (1967). "Attempts to release the scrapie agent from tissue debris". *Journal of Comparative Pathology* **77**:3, 301–307.

Hunter, G. D., Millson, G. C., and Meek, G. (1964). "The intracellular location of the agent of mouse scrapie". *Journal of General Microbiology* **34**:2, 319–325.

Hunter, G. D., Kimberlin, R. H., and Gibbons, R. A. (1968). "Scrapie: A modified membrane hypothesis". *Journal of Theoretical Biology* **20**:3, 355–357.

Hunter, G., Gibbons, R., Kimberlin, R., and Millson, G. (1969). "Further studies of the infectivity and stability of extracts and homogenates derived from scrapie affected mouse brains". *Journal of Comparative Pathology* **79**:1, 101–108.

Inouye, H, Fraser, P. E., and Kirschner, D. A. (1993). "Structure of β-crystallite assemblies formed by Alzheimer β-amyloid protein analogues: analysis by x-ray diffraction". *Biophysical Journal* **64**:2, 502–519.

Jahn, T. R., Makin, O. S., Morris, K. L., Marshall, K. E., Tian, P., Sikorski, P., and Serpell, L. C. (2010). "The common architecture of cross-β amyloid". *Journal of Molecular Biology* **395**:4, 717–727.

James, T. L., Liu, H., Ulyanov, N. B., Farr-Jones, S., Zhang, H., Donne, D. G., Kaneko, K., Groth, D., Mehlhorn, I., Prusiner, S. B., and Cohen, F. E. (1997). "Solution structure of a 142-residue recombinant prion protein corresponding to the infectious fragment of the scrapie isoform". *Proceedings of the National Academy of Sciences of the United States of America* **94**:19, 10086–10091.

Kabani, M. and Melki, R. (2011). "Yeast prions assembly and propagation: Contributions of the prion and non-prion moieties and the nature of assemblies". *Prion* **5**:4, 277–284.

Kajava, A. V. and Steven, A. C. (2006). "β-rolls, β-helices, and other β-solenoid proteins". *Fibrous Proteins: Amyloids, Prions and Beta Proteins*. Vol. 73. Academic Press, 55–96.

Kaneko, K., Ball, H. L., Wille, H., Zhang, H., Groth, D., Torchia, M., Tremblay, P., Safar, J., Prusiner, S. B., DeArmond, S. J., Baldwin, M. A., and Cohen, F. E. (2000). "A synthetic peptide initiates Gerstmann-Sträussler-Scheinker (GSS) disease in transgenic mice". *Journal of Molecular Biology* **295**:4, 997–1007.

Kendall, A. and Stubbs, G. (2006). "Oriented sols for fiber diffraction from limited quantities or hazardous materials". *Journal of Applied Crystallography* **39**:1, 39–41.

King, C.-Y. and Diaz-Avalos, R. (2004). "Protein-only transmission of three yeast prion strains". *Nature* **428**:6980, 319–323.

Kishimoto, A, Hasegawa, K, Suzuki, H, Taguchi, H, Namba, K, and Yoshida, M (2004). "β-Helix is a likely core structure of yeast prion Sup35 amyloid fibers". *Biochemical and Biophysical Research Communications* **315**:3, 739–745.

Klatzo, I., Gajdusek, D. C., and Zigas, V (1959). "Pathology of kuru". *Laboratory Investigation* **8**:4, 799–847.

Klug, A., Crick, F. H. C., and Wyckoff, H. W. (1958). "Diffraction by helical structures". *Acta Crystallographica* **11**:3, 199–213.

Lambert, R. J., Mytilinaios, I., Maitland, L., and Brown, A. M. (2012). "Monte Carlo simulation of parameter confidence intervals for non-linear regression analysis of biological data using Microsoft Excel". *Computer Methods and Programs in Biomedicine* **107**:2, 155–163.

Lange, A., Gattin, Z., Van Melckebeke, H., Wasmer, C., Soragni, A., Gunsteren, W. F. van, and Meier, B. H. (2009). "A combined solid-state NMR and MD characterization of the stability and dynamics of the HET-s(218–289) prion in its amyloid conformation". *ChemBioChem* **10**:10, 1657–1665.

Latarjet, R., Muel, B., Haig, D. A., Clarke, M. C., and Alper, T. (1970). "Inactivation of the scrapie agent by near monochromatic ultraviolet light". *Nature* **227**:5265, 1341–1343.

Legname, G., Baskakov, I. V., Nguyen, H.-O. B., Riesner, D., Cohen, F. E., DeArmond, S. J., and Prusiner, S. B. (2004). "Synthetic mammalian prions". *Science* **305**:5684, 673–676.

Leopoldt, J. G. (1750). *Nützliche und auf die Erfahrung gegrüdete Einleitung zu der Land-Wirthschafft*. Vol. 5. Sorau, 348.

Levin, M, Pras, M, and Franklin, E. C. (1973). "Immunologic studies of the major non-immunoglobulin protein of amyloid. I. Identification and partial characterization of a related serum component". *The Journal of Experimental Medicine* **138**:2, 373–380.

Lipson, H. and Taylor, C. A. (1958). *Fourier transforms and X-ray diffraction*. Glasgow: G. Bell and Sons.

Lu, J.-X., Qiang, W., Yau, W.-M., Schwieters, C., Meredith, S., and Tycko, R. (2013). "Molecular structure of β-Amyloid fibrils in alzheimer's disease brain tissue". *Cell* **154**:6, 1257–1268.

Luca, S., Yau, W.-M., Leapman, R., and Tycko, R. (2007). "Peptide conformation and supramolecular organization in amylin fibrils: constraints from solid-state NMR". *Biochemistry* **46**:47, 13505–13522.

Luckgei, N., Schütz, A. K., Bousset, L., Habenstein, B., Sourigues, Y., Gardiennet, C., Meier, B. H., Melki, R., and Böckmann, A. (2013). "The conformation of the prion domain of Sup35 p in isolation and in the full-length protein". *Angewandte Chemie International Edition* **52**:48, 12741–12744.

Luk, K. C., Kehm, V., Carroll, J., Zhang, B., O'Brien, P., Trojanowski, J. Q., and Lee, V. M.-Y. (2012). "Pathological α-synuclein transmission initiates Parkinson-like neurodegeneration in nontransgenic mice". *Science* **338**:6109, 949–953.

Lundmark, K., Westermark, G. T., Nyström, S., Murphy, C. L., Solomon, A., and Westermark, P. (2002). "Transmissibility of systemic amyloidosis by a prion-like mechanism". *Proceedings of the National Academy of Sciences of the United States of America* **99**:10, 6979–6984.

Maddelein, M. L., Dos Reis, S, Duvezin-Caubet, S, Coulary-Salin, B, and Saupe, S. J. (2002). "Amyloid aggregates of the HET-s prion protein are infectious". *Proceedings of the National Academy of Sciences of the United States of America* **99**:11, 7402–7407.

Maji, S. K., Perrin, M. H., Sawaya, M. R., Jessberger, S., Vadodaria, K., Rissman, R. A., Singru, P. S., Nilsson, K. P. R., Simon, R., Schubert, D., Eisenberg, D., Rivier, J., Sawchenko, P., Vale, W., and Riek, R. (2009). "Functional amyloids as natural storage of peptide hormones in pituitary secretory granules". *Science* **325**:5938, 328–332.

Makarava, N., Kovacs, G. G., Savtchenko, R., Alexeeva, I., Budka, H., Rohwer, R. G., and Baskakov, I. V. (2011). "Genesis of mammalian prions: from non-infectious amyloid fibrils to a transmissible prion disease". *PLoS Pathogens* **7**:12, e1002419.

Makarava, N., Kovacs, G. G., Savtchenko, R., Alexeeva, I., Ostapchenko, V. G., Budka, H., Rohwer, R. G., and Baskakov, I. V. (2012a). "A new mechanism for transmissible prion diseases". *The Journal of Neuroscience* **32**:21, 7345–7355.

Makarava, N., Kovacs, G. G., Savtchenko, R., Alexeeva, I., Budka, H., Rohwer, R. G., and Baskakov, I. V. (2012b). "Stabilization of a prion strain of synthetic origin requires multiple serial passages". *Journal of Biological Chemistry* **287**: 30205–30214.

Makowski, L. (1978). "Processing of X-ray diffraction data from partially oriented specimens". *Journal of Applied Crystallography* **11**:4, 273–283.

Marsh, R. E., Corey, R. B., and Pauling, L. (1955). "An investigation of the structure of silk fibroin". *Biochimica et Biophysica Acta* **16**: 1–34.

Marvin, D. A., Wiseman, R. L., and Wachtel, E. J. (1974). "Filamentous bacterial viruses: XI. Molecular architecture of the class II (Pf1, Xf) virion". *Journal of Molecular Biology* **82**:2, 121–138.

Marvin, D. A., Hale, R. D., Nave, C., and Citterich, M. H. (1994). "Molecular models and structural comparisons of native and mutant class I filamentous bacteriophages: Ff (fd, f1, M13), If1 and IKe". *Journal of Molecular Biology* **235**:1, 260–286.

Mathews, J. D., Glasse, R., and Lindenbaum, S. (1968). "Kuru and cannibalism". *The Lancet* **292**:7565, 449–452.

Maurstad, G., Prass, M., Serpell, L. C., and Sikorski, P. (2009). "Dehydration stability of amyloid fibrils studied by AFM". *European Biophysics Journal* **38**:8, 1135–1140.

McAlister, V. (2005). "Sacred disease of our times: failure of the infectious disease model of spongiform encephalopathy". *Clinical and Investigative Medicine. Médecine Clinique Et Experimentale* **28**:3, 101–104.

McDonald, M., Kendall, A., Tanaka, M., Weissman, J. S., and Stubbs, G. (2008). "Enclosed chambers for humidity control and sample containment in fiber diffraction". *Journal of Applied Crystallography* **41**:1, 206–209.

McDonald, M., Kendall, A., Bian, W., McCullough, I., Lio, E., Havens, W. M., Ghabrial, S. A., and Stubbs, G. (2010). "Architecture of the potyviruses". *Virology* **405**:2, 309–313.

McDonald, M., Box, H., Bian, W., Kendall, A., Tycko, R., and Stubbs, G. (2012). "Fiber diffraction data indicate a hollow core for the Alzheimer's Aβ 3-fold symmetric fibril". *Journal of Molecular Biology* **423**:3, 454–461.

McGlinchey, R. P., Shewmaker, F., McPhie, P., Monterroso, B., Thurber, K., and Wickner, R. B. (2009). "The repeat domain of the melanosome fibril protein Pmel17 forms the amyloid core promoting melanin synthesis". *Proceedings of the National Academy of Sciences of the United States of America* **106**:33, 13731–13736.

McKinley, M. P., Masiarz, F. R., and Prusiner, S. B. (1981). "Reversible chemical modification of the scrapie agent". *Science* **214**:4526, 1259–1261.

McKinley, M. P., Bolton, D. C., and Prusiner, S. B. (1983). "A protease-resistant protein is a structural component of the scrapie prion". *Cell* **35**:1, 57–62.

Medori, R., Tritschler, H.-J., LeBlanc, A., Villare, F., Manetto, V., Chen, H. Y., Xue, R., Leal, S., Montagna, P., Cortelli, P., Tinuper, P., Avoni, P., Mochi, M., Baruzzi, A., Hauw, J. J., Ott, J., Lugaresi, E., Autilio-Gambetti, L., and Gambetti, P. (1992). "Fatal familial insomnia, a prion disease with a mutation at codon 178 of the prion protein gene". *New England Journal of Medicine* **326**:7, 444–449.

Meinhardt, J., Sachse, C., Hortschansky, P., Grigorieff, N., and Fändrich, M. (2009). "Aβ(1-40) fibril polymorphism implies diverse interaction patterns in amyloid fibrils". *Journal of Molecular Biology* **386**:3, 869–877.

M'Fadyean, J. (1918). "Scrapie". *Journal of Comparative Pathology and Therapeutics* **31**: 102–131.

M'Gowan, J. P. (1914). *Investigation into the disease of sheep called "scrapie"*. Edinburgh: William Blackwood and Sons.

Miller, Y., Ma, B., and Nussinov, R. (2011). "The Unique Alzheimer's β-amyloid triangular fibril has a cavity along the fibril axis under physiological conditions". *Journal of the American Chemical Society* **133**:8, 2742–2748.

Mizuno, N., Baxa, U., and Steven, A. C. (2011). "Structural dependence of HET-s amyloid fibril infectivity assessed by cryoelectron microscopy". *Proceedings of the National Academy of Sciences of the United States of America* **108**:8, 3252 –3257.

Morris, K. and Serpell, L. (2010). "From natural to designer self-assembling biopolymers, the structural characterisation of fibrous proteins & peptides using fibre diffraction". *Chemical Society Reviews* **39**: 3445–3453.

Morris, K., Rodger, A., Hicks, M., Debulpaep, M., Schymkowitz, J., Rousseau, F., and Serpell, L. (2013). "Exploring the sequence–structure relationship for amyloid peptides". *Biochemical Journal* **450**:2, 275–283.

Mould, D. L., Smith, W., and Dawson, A. M. (1964a). "The elution of scrapie brain tissue through calcium phosphate columns". *Biochemical Journal* **91**: 13P.

Mould, D. L., Dawson, A. M., and Smith, W (1964b). "The infectivities of brain-cell fractions from mice infected with Suffolk sheep scrapie agent". *Biochemical Journal* **91**: 13P–14P.

Mould, D. L., Dawson, A. M., and Smith, W (1965). "Scrapie in mice. The stability of the agent to various suspending media, pH and solvent extraction". *Research in Veterinary Science* **6**: 151–154.

Münch, C., O'Brien, J., and Bertolotti, A. (2011). "Prion-like propagation of mutant superoxide dismutase-1 misfolding in neuronal cells". *Proceedings of the National Academy of Sciences of the United States of America* **108**:9, 3548–3553.

Namba, K., Pattanayek, R., and Stubbs, G. (1989). "Visualization of protein-nucleic acid interactions in a virus : Refined structure of intact tobacco mosaic virus at 2.9 Å resolution by X-ray fiber diffraction". *Journal of Molecular Biology* **208**:2, 307–325.

Nelson, R., Sawaya, M. R., Balbirnie, M., Madsen, A. O., Riekel, C., Grothe, R., and Eisenberg, D. (2005). "Structure of the cross-β spine of amyloid-like fibrils". *Nature* **435**:7043, 773–778.

Nicoll, A. J., Panico, S., Freir, D. B., Wright, D., Terry, C., Risse, E., Herron, C. E., O'Malley, T., Wadsworth, J. D. F., Farrow, M. A., Walsh, D. M., Saibil, H. R., and Collinge, J. (2013). "Amyloid-β nanotubes are associated with prion protein-dependent synaptotoxicity". *Nature Communications* **4**:

Nielsen, L., Khurana, R., Coats, A., Frokjaer, S., Brange, J., Vyas, S., Uversky, V. N., and Fink, A. L. (2001). "Effect of environmental factors on the kinetics of insulin fibril formation: elucidation of the molecular mechanism". *Biochemistry* **40**:20, 6036–6046.

Nilsson, M. R. (2004). "Techniques to study amyloid fibril formation in vitro". *Methods* **34**:1, 151–160.

Nishiyama, Y., Langan, P., and Chanzy, H. (2002). "Crystal structure and hydrogen-bonding system in cellulose Iβ from synchrotron X-ray and neutron fiber diffraction". *Journal of the American Chemical Society* **124**:31, 9074–9082.

Oda, T., Makino, K., Yamashita, I., Namba, K., and Maéda, Y. (1998). "Effect of the length and effective diameter of F-actin on the filament orientation in liquid crystalline sols measured by X-ray fiber diffraction". *Biophysical Journal* **75**:6, 2672–2681.

Oda, T., Iwasa, M., Aihara, T., Maéda, Y., and Narita, A. (2009). "The nature of the globular- to fibrous-actin transition". *Nature* **457**:7228, 441–445.

Oelschlegel, A. M. and Weissmann, C. (2013). "Acquisition of drug resistance and dependence by prions". *PLoS Pathogens* **9**:2, e1003158.

Oesch, B., Westaway, D., Wälchli, M., McKinley, M. P., Kent, S. B. H., Aebersold, R., Barry, R. A., Tempst, P., Teplow, D. B., Hood, L. E., Prusiner, S. B., and Weissmann, C. (1985). "A cellular gene encodes scrapie PrP 27-30 protein". *Cell* **40**:4, 735–746.

Orgel, J. P. R. O., Irving, T. C., Miller, A., and Wess, T. J. (2006). "Microfibrillar structure of type I collagen in situ". *Proceedings of the National Academy of Sciences of the United States* **103**:24, 9001 –9005.

Pan, K. M., Baldwin, M., Nguyen, J., Gasset, M., Serban, A., Groth, D., Mehlhorn, I., Huang, Z., Fletterick, R. J., and Cohen, F. E. (1993). "Conversion of alpha-helices into beta-sheets features in the formation of the scrapie prion proteins". *Proceedings of the National Academy of Sciences of the United States of America* **90**:23, 10962–10966.

Paravastu, A. K., Leapman, R. D., Yau, W.-M., and Tycko, R. (2008). "Molecular structural basis for polymorphism in Alzheimer's β-amyloid fibrils". *Proceedings of the National Academy of Sciences of the United States of America* **105**:47, 18349 –18354.

Parker, K. D. and Rudall, K. M. (1957). "The silk of the egg-stalk of the green lace-wing fly: structure of the silk of chrysopa egg-stalks". *Nature* **179**:4566, 905–906.

Pattison, I. H. (1965). "Resistance of the scrapie agent to formalin". *Journal of Comparative Pathology* **75**:2, 159–164.

Pattison, I. H. and Jones, K. M. (1967). "The possible nature of the transmissible agent of scrapie". *The Veterinary Record* **80**:1, 2–9.

Perutz, M. F., Finch, J. T., Berriman, J, and Lesk, A (2002). "Amyloid fibers are water-filled nanotubes". *Proceedings of the National Academy of Sciences of the United States of America* **99**:8, 5591–5595.

Petkova, A. T., Leapman, R. D., Guo, Z., Yau, W.-M., Mattson, M. P., and Tycko, R. (2005). "Self-propagating, molecular-level polymorphism in alzheimer's β-amyloid fibrils". *Science* **307**:5707, 262–265.

Petkova, A. T., Yau, W.-M., and Tycko, R. (2006). "Experimental constraints on quaternary structure in alzheimer's β-amyloid fibrils". *Biochemistry* **45**:2, 498–512.

Prusiner, S. B. (1982). "Novel proteinaceous infectious particles cause scrapie". *Science* **216**:4542, 136–144.

Prusiner, S. B. (1991). "Molecular biology of prion diseases". *Science* **252**:5012, 1515–1522.

Prusiner, S. B. (2012). "A unifying role for prions in neurodegenerative diseases". *Science* **336**:6088, 1511–1513.

Prusiner, S. B., Hadlow, W. J., Eklund, C. M., and Race, R. E. (1977). "Sedimentation properties of the scrapie agent". *Proceedings of the National Academy of Sciences of the United States of America* **74**:10, 4656–4660.

Prusiner, S. B., Hadlow, W. J., Garfin, D. E., Cochran, S. P., Baringer, J. R., Race, R. E., and Eklund, C. M. (1978a). "Partial purification and evidence for multiple molecular forms of the scrapie agent". *Biochemistry* **17**:23, 4993–4999.

Prusiner, S. B., Hadlow, W. J., Eklund, C. M., Race, R. E., and Cochran, S. P. (1978b). "Sedimentation characteristics of the scrapie agent from murine spleen and brain". *Biochemistry* **17**:23, 4987–4992.

Prusiner, S. B., Groth, D. F., Cochran, S. P., Masiarz, F. R., McKinley, M. P., and Martinez, H. M. (1980). "Molecular properties, partial purification, and assay by incubation period measurements of the hamster scrapie agent". *Biochemistry* **19**:21, 4883–4891.

Prusiner, S. B., McKinley, M. P., Groth, D. F., Bowman, K. A., Mock, N. I., Cochran, S. P., and Masiarz, F. R. (1981a). "Scrapie agent contains a hydrophobic protein". *Proceedings of the National Academy of Sciences of the United States of America* **78**:11, 6675–6679.

Prusiner, S. B., Groth, D. F., McKinley, M. P., Cochran, S. P., Bowman, K. A., and Kasper, K. C. (1981b). "Thiocyanate and hydroxyl ions inactivate the scrapie agent". *Proceedings of the National Academy of Sciences of the United States of America* **78**:7, 4606–4610.

Prusiner, S. B., Bolton, D. C., Groth, D. F., Bowman, K. A., Cochran, S. P., and McKinley, M. P. (1982). "Further purification and characterization of scrapie prions". *Biochemistry* **21**:26, 6942–6950.

Prusiner, S. B., McKinley, M. P., Bowman, K. A., Bolton, D. C., Bendheim, P. E., Groth, D. F., and Glenner, G. G. (1983). "Scrapie prions aggregate to form amyloid-like birefringent rods". *Cell* **35**:2, Part 1, 349–358.

Prusiner, S. B., Groth, D. F., Bolton, D. C., Kent, S. B., and Hood, L. E. (1984). "Purification and structural studies of a major scrapie prion protein". *Cell* **38**:1, 127–134.

Prusiner, S. B., Füzi, M, Scott, M, Serban, D., Serban, H., Taraboulos, A., Gabriel, J.-M., Wells, G. A. H., Wilesmith, J. W., Bradley, R., DeArmond, S. J., and Kristensson, K. (1993). "Immunologic and molecular biologic studies of prion proteins in bovine spongiform encephalopathy". *Journal of Infectious Diseases* **167**:3, 602–613.

Rajkumar, G., Al-Khayat, H. A., Eakins, F., He, A., Knupp, C., and Squire, J. (2005). "FibreFix—A new integrated CCP13 software package". *Fibre Diffraction Review* **13**: 11–18.

Reconditi, M. (2006). "Recent improvements in small angle x-ray diffraction for the study of muscle physiology". *Reports on Progress in Physics* **69**:10, 2709–2759.

Ridley, R. M., Baker, H. F., Windle, C. P., and Cummings, R. M. (2006). "Very long term studies of the seeding of β-amyloidosis in primates". *Journal of Neural Transmission* **113**:9, 1243–1251.

Ritter, C., Maddelein, M.-L., Siemer, A. B., Luhrs, T., Ernst, M., Meier, B. H., Saupe, S. J., and Riek, R. (2005). "Correlation of structural elements and infectivity of the HET-s prion". *Nature* **435**:7043, 844–848.

Roberts, G. W., Lofthouse, R, Brown, R, Crow, T. J., Barry, R. A., and Prusiner, S. B. (1986). "Prion-protein immunoreactivity in human transmissible dementias". *The New England Journal of Medicine* **315**:19, 1231–1233.

Rochin, L., Hurbain, I., Serneels, L., Fort, C., Watt, B., Leblanc, P., Marks, M. S., Strooper, B. D., Raposo, G., and Niel, G. v. (2013). "BACE2 processes PMEL to form the melanosome amyloid matrix in pigment cells". *Proceedings of the National Academy of Sciences* **110**:26, 10658–10663.

Ross, E. D., Baxa, U., and Wickner, R. B. (2004). "Scrambled prion domains form prions and amyloid". *Molecular and Cellular Biology* **24**:16, 7206–7213.

Ross, E. D., Edskes, H. K., Terry, M. J., and Wickner, R. B. (2005). "Primary sequence independence for prion formation". *Proceedings of the National Academy of Sciences of the United States of America* **102**:36, 12825–12830.

Rudall, K. M. (1946). "The structure of epidermal protein". *The Society of Dyers and Colourists: Symposium on Fibrous Proteins*. Leeds, England: Chorley and Pickersgill, 15–23.

Sabaté, R., Baxa, U., Benkemoun, L., Groot, N. S. de, Coulary-Salin, B., Maddelein, M.-l., Malato, L., Ventura, S., Steven, A. C., and Saupe, S. J. (2007). "Prion and non-prion amyloids of the HET-s prion forming domain". *Journal of Molecular Biology* **370**:4, 768–783.

Sachse, C., Fändrich, M., and Grigorieff, N. (2008). "Paired β-sheet structure of an Aβ(1-40) amyloid fibril revealed by electron microscopy". *Proceedings of the National Academy of Sciences of the United States of America* **105**:21, 7462–7466.

Saupe, S. J. (2011). "The [Het-s] prion of *Podospora anserina* and its role in heterokaryon incompatibility". *Seminars in Cell & Developmental Biology* **22**:5, 460–468.

Sawaya, M. R., Sambashivan, S., Nelson, R., Ivanova, M. I., Sievers, S. A., Apostol, M. I., Thompson, M. J., Balbirnie, M., Wiltzius, J. J. W., McFarlane, H. T., Madsen, A. O., Riekel, C., and Eisenberg, D. (2007). "Atomic structures of amyloid cross-β spines reveal varied steric zippers". *Nature* **447**:7143, 453–457.

Schneider, K., Fangerau, H., Michaelsen, B., and Raab, W. H.-M. (2008). "The early history of the transmissible spongiform encephalopathies exemplified by scrapie". *Brain Research Bulletin* **77**:6, 343–355.

Sen, A., Baxa, U., Simon, M. N., Wall, J. S., Sabate, R., Saupe, S. J., and Steven, A. C. (2007). "Mass analysis by scanning transmission electron microscopy and electron diffraction validate predictions of stacked β-solenoid model of HET-s prion fibrils". *Journal of Biological Chemistry* **282**:8, 5545–5550.

Seuring, C., Greenwald, J., Wasmer, C., Wepf, R., Saupe, S. J., Meier, B. H., and Riek, R. (2012). "The mechanism of toxicity in HET-S/HET-s prion incompatibility". *PLoS Biology* **10**:12, e1001451.

Shewmaker, F., Ross, E. D., Tycko, R., and Wickner, R. B. (2008). "Amyloids of shuffled prion domains that form prions have a parallel in-register β-sheet structure". *Biochemistry* **47**:13, 4000–4007.

Shotton, M. W., Pope, L. H., Forsyth, V. T., Denny, R. C., Archer, J., Langan, P., Ye, H., and Boote, C. (1998). "New developments in instrumentation for X-ray and neutron fibre diffraction Experiments". *Journal of Applied Crystallography* **31**:5, 758–766.

Siedler, H and Malamud, N (1963). "Creutzfeldt-Jakob's disease. clinicopathologic report of 15 cases and review of the literature (with special reference to a related disorder designated as subacute spongiform encephalopathy)". *Journal of Neuropathology and Experimental Neurology* **22**: 381–402.

Sigurdsson, B. (1954). "Rida, a chronic encephalitis of sheep". *British Veterinary Journal* **110**: 341–354.

Spillantini, M. G., Schmidt, M. L., Lee, V. M.-Y., Trojanowski, J. Q., Jakes, R., and Goedert, M. (1997). "α-synuclein in lewy bodies". *Nature* **388**:6645, 839–840.

Squires, A. M., Devlin, G. L., Gras, S. L., Tickler, A. K., MacPhee, C. E., and Dobson, C. M. (2006). "X-ray scattering study of the effect of hydration on the cross-β structure of amyloid fibrils". *Journal of the American Chemical Society* **128**:36, 11738–11739.

Stahl, N., Baldwin, M. A., Teplow, D. B., Hood, L., Gibson, B. W., Burlingame, A. L., and Prusiner, S. B. (1993). "Structural studies of the scrapie prion protein using mass spectrometry and amino acid sequencing". *Biochemistry* **32**:8, 1991–2002.

Stockman, S. (1913). "Scrapie: an obscure disease of sheep". *Journal of Comparative Pathology and Therapeutics* **26**: 317–327.

Stubbs, G. (1989). "The probability distributions of X-ray intensities in fiber diffraction: largest likely values for fiber diffraction R factors". *Acta Crystallographica Section A Foundations of Crystallography* **45**:3, 254–258.

Stubbs, G. J. (1974). "The effect of disorientation on the intensity distribution of non-crystalline fibres. II. Applications". *Acta Crystallographica Section A Foundations of Crystallography* **30**:5, 639–645.

Studier, F. W. (2005). "Protein production by auto-induction in high density shaking cultures". *Protein Expression and Purification* **41**:1, 207–234.

Stöhr, J., Watts, J. C., Mensinger, Z. L., Oehler, A., Grillo, S. K., DeArmond, S. J., Prusiner, S. B., and Giles, K. (2012). "Purified and synthetic alzheimer's amyloid Beta (Aβ) prions". *Proceedings of the National Academy of Sciences of the United States of America* **109**:27, 11025–11030.

Sugiyama, T., Miyashiro, D., Takao, D., Iwamoto, H., Sugimoto, Y., Wakabayashi, K., and Kamimura, S. (2009). "Quick shear-flow alignment of biological filaments for X-ray fiber diffraction facilitated by methylcellulose". *Biophysical Journal* **97**:12, 3132–3138.

Sunde, M, Serpell, L. C., Bartlam, M, Fraser, P. E., Pepys, M. B., and Blake, C. C. (1997). "Common core structure of amyloid fibrils by synchrotron X-ray diffraction". *Journal of Molecular Biology* **273**:3, 729–739.

Toyama, B. H., Kelly, M. J. S., Gross, J. D., and Weissman, J. S. (2007). "The structural basis of yeast prion strain variants". *Nature* **449**:7159, 233–237.

Tsuruta, H and Irving, T. (2008). "Experimental approaches for solution X-ray scattering and fiber diffraction". *Current Opinion in Structural Biology* **18**:5, 601–608.

Van Melckebeke, H, Wasmer, H, Lange, A, AB, E., Loquet, A, Böckmann, A, and Meier, B. H. (2010). "Atomic-resolution three-dimensional structure of HET-s(218–289) amyloid fibrils by solid-state NMR spectroscopy". *Journal of the American Chemical Society* **132**:39, 13765–13775.

Van Melckebeke, H., Schanda, P., Gath, J., Wasmer, C., Verel, R., Lange, A., Meier, B. H., and Böckmann, A. (2011). "Probing water accessibility in HET-s(218–289) amyloid fibrils by solid-state NMR". *Journal of Molecular Biology* **405**:3, 765–772.

Virchow, R. (1854). "Zur Cellulose – Frage". *Archiv für pathologische Anatomie und Physiologie und für klinische Medicin* **6**:3, 416–426.

Volpicelli-Daley, L., Luk, K., Patel, T., Tanik, S., Riddle, D., Stieber, A., Meaney, D., Trojanowski, J., and Lee, V.-Y. (2011). "Exogenous α-synuclein fibrils induce lewy body pathology leading to synaptic dysfunction and neuron death". *Neuron* **72**:1, 57–71.

Walsh, P., Simonetti, K., and Sharpe, S. (2009). "Core structure of amyloid fibrils formed by residues 106–126 of the human prion protein". *Structure* **17**:3, 417–426.

Wan, W., Wille, H., Stohr, J., Baxa, U., Prusiner, S. B., and Stubbs, G. (2012). "Degradation of fungal prion HET-s(218–289) induces formation of a generic amyloid fold". *Biophysical Journal* **102**:10, 2339–2344.

Wan, W., Bian, W., McDonald, M., Kijac, A., Wemmer, D. E., and Stubbs, G. (2013). "Heterogeneous seeding of a prion structure by a generic amyloid form of the fungal prion-forming domain HET-s(218–289)". *Journal of Biological Chemistry* **288**:41, 29604–29612.

Wang, F., Wang, X., Yuan, C.-G., and Ma, J. (2010). "Generating a prion with bacterially expressed recombinant prion protein". *Science* **327**:5969, 1132–1135.

Wang, W and Malcolm, B. A. (1999). "Two-stage PCR protocol allowing introduction of multiple mutations, deletions and insertions using QuikChange Site-Directed Mutagenesis". *BioTechniques* **26**:4, 680–682.

Wasmer, C., Lange, A., Van Melckebeke, H., Siemer, A. B., Riek, R., and Meier, B. H. (2008a). "Amyloid fibrils of the HET-s(218-289) prion form a β-Solenoid with a triangular hydrophobic core". *Science* **319**:5869, 1523–1526.

Wasmer, C., Soragni, A., Sabaté, R., Lange, A., Riek, R., and Meier, B. (2008b). "Infectious and noninfectious amyloids of the HET-s(218–289) prion have different NMR spectra". *Angewandte Chemie International Edition* **47**:31, 5839–5841.

Wasmer, C., Schütz, A., Loquet, A., Buhtz, C., Greenwald, J., Riek, R., Böckmann, A., and Meier, B. H. (2009). "The molecular organization of the fungal prion HET-s in its amyloid Form". *Journal of Molecular Biology* **394**:1, 119–127.

Wasmer, C., Zimmer, A., Sabaté, R., Soragni, A., Saupe, S. J., Ritter, C., and Meier, B. H. (2010). "Structural similarity between the prion domain of HET-s and a homologue can explain amyloid cross-seeding in spite of limited sequence identity". *Journal of Molecular Biology* **402**:2, 311–325.

Wells, G. A., Scott, A. C., Johnson, C. T., Gunning, R. F., Hancock, R. D., Jeffrey, M., Dawson, M., and Bradley, R. (1987). "A novel progressive spongiform encephalopathy in cattle". *The Veterinary Record* **121**:18, 419–420.

Westermark, P., Wernstedt, C., Wilander, E., and Sletten, K. (1986). "A novel peptide in the calcitonin gene related peptide family as an amyloid fibril protein in the endocrine pancreas". *Biochemical and Biophysical Research Communications* **140**:3, 827–831.

Wickner, R. B. (1994). "[URE3] as an altered URE2 protein: evidence for a prion analog in textitSaccharomyces cerevisiae". *Science* **264**:5158, 566–569.

Wickner, R. B., Taylor, K. L., Edskes, H. K., Maddelein, M. L., Moriyama, H, and Roberts, B. T. (1999). "Prions in Saccharomyces and Podospora spp.: protein-based inheritance". *Microbiology and Molecular Biology Reviews* **63**:4, 844–861.

Wille, H., Michelitsch, M. D., Guénebaut, V., Supattapone, S., Serban, A., Cohen, F. E., Agard, D. A., and Prusiner, S. B. (2002). "Structural studies of the scrapie prion protein by electron crystallography". *Proceedings of the National Academy of Sciences of the United States of America* **99**:6, 3563–3568.

Wille, H., Bian, W., McDonald, M., Kendall, A., Colby, D. W., Bloch, L., Ollesch, J., Borovinskiy, A. L., Cohen, F. E., Prusiner, S. B., and Stubbs, G. (2009). "Natural and synthetic prion structure from X-ray fiber diffraction". *Proceedings of the National Academy of Sciences of the United States of America* **106**:40, 16990–16995.

Wischik, C. M., Novak, M, Thøgersen, H. C., Edwards, P. C., Runswick, M. J., Jakes, R, Walker, J. E., Milstein, C, Roth, M, and Klug, A (1988). "Isolation of a fragment of tau derived from the core of the paired helical filament of Alzheimer disease." *Proceedings of the National Academy of Sciences of the United States of America* **85**:12, 4506–4510.

Yamashita, I., Vonderviszt, F., Noguchi, T., and Namba, K. (1991). "Preparing well-oriented sols of straight bacterial flagellar filaments for X-ray fiber diffraction". *Journal of Molecular Biology* **217**:2, 293–302.

Yamashita, I., Suzuki, H., and Namba, K. (1998). "Multiple-step method for making exceptionally well-oriented liquid-crystalline sols of macromolecular assemblies". *Journal of Molecular Biology* **278**:3, 609–615.

Zlotnik, I. and Barlow, R. M. (1967). "The transmission of a specific encephalopathy of mink to the goat". *Veterinary Record* **81**:2, 55–56.